OPTIMIZATION OF A PACKAGED AIR CONDITIONING UNIT PERFORMANCE USING AN EXPERIMENTALLY VALIDATED CFD MODEL

ADEL MOHAMMED HUSSAIN AL-NASSER

MECHANICAL ENGINEERING

25 JUNE 2003

KING FAHD UNIVERSITY OF PETROLEUM & MINERALS

DHAHRAN 31261, SAUDI ARABIA

DEANSHIP OF GRADUATE STUDIES

This Thesis, written by Adel Mohammed Hussain Al-Nasser under the direction of his thesis advisor and approved by his committee, has been presented to and accepted by the Dean of Graduate Studies, in partial fulfillment of the requirements for the degree of MASTER OF SCIENCE IN MECHANICAL ENGINEERING.

Thesis committee

Dr. Rached Ben-Mansour
(Advisor)

Dr. Syed A.M. Said
(Co-Advisor)

Dr. Mohammed A. Habib
(Member)

Dr. Faleh A. Al-Sulaiman
Department Chairman

Dr. Esmail Mokheimer
(Member)

Mr. Hashim A. Al-Saedi
(Member)

Dr. Osama A. Jannadi
Dean of Graduate Studies

Date: _____

Dedicated to

My Loving Parents
& Growing Family

ACKNOWLEDGEMENT

I am extremely grateful to Almighty Allah who granted me the capability and luck to reach this achievement.

Acknowledgement is due to King Fahd University of petroleum and Minerals for supporting this research. I would like to express my deep appreciation to my thesis advisor, Dr. Rached Ben-Mansour, for his continuous support and guidance throughout this work. His instructions were key towards completing this accomplishment. Thanks are due to the members of my thesis committee, Dr. S.A.M. Said, Dr. M.A. Habib and Dr. E. Mokheimer for their constructive criticisms towards the success of this work.

My sincere gratitude is offered to the distinguished member of my thesis committee, Mr. Hashim A. Bounyan Al-Saedi, the Director of Research and Development Department in Zamil Air Conditioners. His leadership in the idea formulation, and guidance in the execution of both the computational and experimental work, all made this work a successful one.

The work was mainly sponsored by Zamil Air Conditioners in Saudi Arabia in terms of supplying the experimental equipment, providing testing facilities and enduring the computational cost. In this chance, I would like to convey my thanks to all Zamil representatives who encouraged and adopted sponsoring this work. Such as Mr. Abdulla M. Al-Zamil, the Senior Vice President, who provided the full support and enthusiasms towards building Saudis technical skills. I also appreciate Mr. Abdul Mohsin Al-Ghamdi, Mr. Khalil Issa, Mr. Virgilio Guevarra and all R & D staffs for their cooperation and assistance.

Special appreciation is due to my team leader, Mr. Ahmad Doughan for his major support and guidance in all processes constructed in the work.

Finally, I am glad to express my deep thanks to my family represented by My Father, My Mother, My Wife and My Uncle for their patience and pray to Almighty Allah to reach this accomplishment.

TABLE OF CONTENTS

LIST OF TABLES

LIST OF FIGURES

NOMENCLATURE

A	surface area, ft^2
B	body force
C_D	drag coefficient
C_p	specific heat
D_h	Hydraulic diameter
ε	dissipation rate of turbulent kinetic energy
f	friction factor
γ	volume porosity
j	colburn factor
JF	combined dimensionless parameter
k	turbulent kinetic energy
k_{ij}	area porosity
K_L	loss coefficient for pressure
$\dot{m}$	mass flow rate, kg/sec
μ	viscosity
ω	angular velocity, rad/sec
P	static pressure
$\overline{P_i}$	average static pressure at fan inlet

$\overline{P}_o$	average static pressure at fan outlet
Pr	Prandtle number
p	perimeter
Q	air volume flow rate, ft^3/min
q	heat transfer rate, W
q"	heat flux
r	radius, in
R	distributed resistance
R'	difference between maximum and minimum SN ratio for each design factor
Re	Reynolds number
RMS	root mean square of fluctuating velocity component
ρ	fluid density, kg/m^3
S	source term
SN	ratio defined by dynamic parameters
T	temperature, deg. F
T_b	bulk temperature, deg. F
T_{exit}	exit air temperature
T_{HX}	heat exchanger surface temperature
TI	turbulence intensity, %
U	mean velocity, ft/min
U_i	time averaged mean velocity
u	mean velocity component in x-direction, ft/min
u(t)	instantaneous flow velocity component in the x-direction, ft/min

u’ fluctuating component of velocity in the x-direction

$\bar{u}$ weighted average velocity integrated on the surface area, ft/min

$u_i u_j$ Reynolds stress tensor

v mean velocity component in y-direction, ft/min

$\overline{V}$ average velocity, ft/min

w mean velocity component in z-direction, ft/min

x,y,z coordinate in axial, lateral and vertical direction

THESIS ABSTRACT

NAME: **ADEL MOHAMMED HUSSAIN AL-NASSER**

TITLE: **Optimization of a Packaged Air Conditioning Unit Performance Using an Experimentally Validated CFD Model**

MAJOR FIELD: **Mechanical Engineering**

DATE OF DEGREE: **June 2003**

In the design of packaged air conditioning equipment, it is found that packaging and installation requirements can often lead to maldistribution of airflow pattern at the approach to, and the discharge from the heat exchanger and other components, which can result in low heat exchanger performance. CFD modeling of airflow and heat transfer in a specified packaged unit is formulated to predict airflow pattern in the unit medium near the evaporator and centrifugal fan. Re-circulation and stagnant areas in the flow field are investigated in the predicted model. Experimental validation of the CFD model is conducted by performing measurements of actual flow characteristics (velocity, pressure and temperature) at different regions in the flow field. A simple parametric study is introduced by identifying the different geometric design parameters affecting airflow distribution in the unit. They are related to the change of components positions in the unit, which produced different thermal and flow performance in comparison with the original configuration.

ملخص بحث

درجة الماجستير في العلوم الهندسيه

الإسم : عادل محمد حسين الناصر

عنوان الرسالة : رفع أداء وحدات تكييف الهواء بإستخدام طرق الإحصاء التحليلية ومقارنتها بالقياسات المختبرية

التخصص : الهندسة الميكانيكية

تاريخ التخرج : يونيو 2003م

عـند تصـنيع وحـدات تكييف الهواء المركزية , يلاحظ وجود عقبات تصميمية تعيق من حركة الهواء عند مـروره عبر المبدل الحراري (المبخر), مما يؤدي إلى انخفاض الطاقة التبريدية لنظام التكييف. لدراسة هذه الظاهـرة, اسـتخدمت تكنولوجيا طرق الإحصاء التحليلية لميكانيكا الموائع في بناء نموذج حاسوبي لمحاكات حـركة الهـواء داخـل نظـام التكييف واستكشاف توزيعه بالقرب من المبدل الحراري ومراوح دفع الهواء المركـزية. لإثبات دقة هذا النموذج الحاسوبي, تم تركيب و اختبار وحدة تبريد مماثلة للنموذج وذلك للمقارنة بيـن النـتائج الاختـبارية والرقمية من حيث السرعة والضغط ودرجة الحرارة, مما كشف مدى فعالية هذا الـنموذج الحاسـوبي. واقترحـت عدة نماذج محسنة التصميم, تم دراسة أداء كل منها بالمقارنة مع النموذج الاصلي, للوصول إلى أفضل تصميم من حيث الأداء.

CHAPTER 1

INTRODUCTION

1.1 BACKGROUND

1.1.1 AIR CONDITIONING SYSTEMS

Different air conditioning systems were developed through the decades to satisfy various requirements of environmental comfort and industrial applications. These systems had their beginning in the early twentieth century of implementing mechanical refrigeration, since the first air conditioning design with its operational equipment was launched in the 1930s. Wide applications of air conditioning equipment such as, industry, houses, hospitals, schools, theaters, business as others made the interaction of this technology more active. The manufacturers introduced many alternative designs with various capacities and sizes.

In the design of air conditioning systems and equipment, different considerations were taken. One of which was the energy consumption. It was known that air conditioning equipment consumed about 60 % of total residential power consumption especially in the long summer season of Saudi Arabia (as announced by SCECO, Saudi Electricity Company) [21].

The demand for designing more energy efficient systems is desired by manufacturers to be able to compete by supplying higher capacity and lower power consumption units. On the other

hand, compact unit sizes and footprints are also desired to offer accessibility of installation in the field. For large air conditioning systems, supply and return air duct are to be installed on the same side of the unit to reduce space requirements in the installation location.

The basic air conditioning unit incorporates the following components in its casing:

- Evaporator coil
- Condenser coil
- Compressor
- Expansion valve
- Fan
- Filter

Other components are added based on the size and application requirements such as, humidifier, air distribution system, thermostat, dampers and control systems. These components are assembled in one casing and connected through a refrigerant circuit for supplying air to the environment. Many functions are performed by air conditioning systems by means of cooling, heating, ventilating, humidifying, and de-humidifying air supplied to the conditioned space.

Air conditioning equipment is classified as unitary or central. The unitary equipment caters limited capacity residential applications such as single or multiple rooms in one building. Window type room air conditioners inserted in the room wall are classified as a unitary type. Larger unit sizes are installed adjacent to the space to be conditioned, some of them are located on the rooftop or outside the building as per the footprint space availability.

The unitary equipment falls in two basic configurations, one of which is the split system that consists of outdoor and indoor sections. In cooling applications, the indoor section incorporates the evaporator coil and the fan blower that supplies air to the room in one chassis. It represents the

low-pressure section of the system. The outdoor section that incorporates compressor, condenser and condenser fan in another chassis is denoted as the high-pressure section. Low and high-pressure sections refer to the state of refrigerant as it passes in the refrigeration circuit. Pressure increase is performed by the compressor in the superheating process while expansion takes place at the evaporator inlet. Both the outdoor and indoor sections are joined by a tube that delivers refrigerant between low and high-pressure sections.

1.1.2 PACKAGED UNIT

The other series of unitary equipment is the packaged type, which connects both the outdoor and indoor sections in one chassis. All components are housed in a single assembly that makes it compact and more accessible for both installation and operation.

Packaged air conditioning units exist in a wide capacity range to serve low and medium applications. The flexibility of the design makes them more preferable than other units. Many optional accessories like control and air distribution systems could be connected to the unit to offer better performance.

The fan existing in medium packaged unit is basically of centrifugal type. It sucks air coming from the conditioned space. Then it throws it to the supply duct after passing through the evaporator coil, where heat transfer takes place. The evaporator coil consists of fin-tube heat exchanger. It involves refrigerant tube circuits distributed in a number of passes. The evaporator operates in two streams, refrigerant and air stream. In cooling process, refrigerant enters the evaporator as a mixture of liquid and gas. Then, it evaporates due to heat transfer between the two streams. As a result, hot air passing through the evaporator is cooled to a certain temperature. Air-cooled temperature varies based on entering conditions and refrigerant temperature. This variation could

be predicted using psychometric chart that correlates the air design condition and cooling coil capacity.

1.1.3 AIRFLOW DISTRIBUTION IN PACKAGED UNIT

In the design of packaged air conditioning equipment, it is found that packaging and installation requirements can often lead to maldistribution of airflow pattern at the approach to, and the discharge from the heat exchanger and other components. Flow maldistribution through the tube banks of evaporator coil is of particular interest for investigation, since it can result in low heat exchanger performance. In order to minimize this phenomenon, it is important to establish under what conditions does flow maldistribution occur, and determine possible steps that can be incorporated in the design of air conditioning unit to resolve this problem.

The fan blower is usually fitted downstream of the evaporator, allowing enough air quantity to pass across evaporator surface and then delivered by the fan to the conditioned space. Uniform air distribution across the evaporator surface area is desired to assure equivalent heat transfer rate within each refrigerant circuit, and maintaining leaving refrigerant temperature (two-phase) in similar level.

The suppliers of air conditioning equipment compete in offering compact systems by minimizing footprint size of the unit on the account of airflow distribution. Reduction of airflow path in the unit medium results in non-uniform air distribution over the heat exchanger that leads to a lower unit performance.

There are limited flow configurations inside the packaged unit, especially the higher capacity units that involve larger component sizes like the wide evaporator and fan housing. In some

configurations, flow behaves in one direction as the inlet, evaporator surface and the outlet are fitted in the same line. This is considered as the best configuration to reduce flow maldistribution but it is not usually attainable design. Other configurations provide a turning flow path between the inlet and outlet, based on the indirect position of the evaporator and fan to the inlet and outlet directions. This arrangement forces the flow to turn with an angle between these components, which causes flow disturbance and non-uniformity.

Flow inside the packaged unit is a turbulent one because of the high velocity air entering the system, which activates flow fluctuation and complexity in some regions of the flow field. On the other hand, the position of some components may lead to flow obstruction, and this participates in reversed flow and re-circulation.

In the next section, a review of earlier study of flow in a packaged unit is introduced, with utilization of CFD technology in predicting flow characteristics in the unit flow field. These earlier studies specify the conditions of flow maldistribution in the unit, their causes, and the proposed alternative designs to minimize their effect.

1.2 LITERATURE REVIEW

1.2.1 PREVIOUS CFD MODELING

Packaged air conditioning unit includes many components that are installed in its casing, such as the fan, the evaporator coil, the filter, the fan motor and the humidifier. The layout of the unit affects the flow pattern inside the casing, which may lead to adverse effects in the performance of the unit due to individual deviation in the performance of each component. Non-ideal airflow

pattern arises due to arrangement of the heat exchanger with respect to the fan. This can result in reduction of heat transfer rate across the evaporator coil.

Computational Fluid Dynamics (CFD) and heat transfer have matured to the stage where state of the art commercial codes can address real engineering problem. These include three dimensional, turbulent flow field and mass transfer. Finite volume method permits numerical solution of such a problem. CFD approach for modeling airflow field in the packaged air conditioning unit was attempted by (Z. G. Xu et al., 1996) [1]. He considered the following issues:

- The model was three-dimensional.
- Turbulent flow was assumed; regions of flow field contain separation and re-circulation.
- Numerous numbers of fins and tubes in the evaporator.
- Rotating elements in the fan.
- Humidity of air that extends the mode to two-phase regime.

Experimental testing of the unit was only possible for a limited number of configurations, but the numerous variables (affecting the flow field) involved in the test made the experiment difficult to perform.

In this study by Xu et al., (1996), CFD approach was used to determine the main characteristics of the flow in the packaged air conditioning unit. The method solved numerically a set of partial differential equations governing the flow and predicted the turbulent re-circulating flow in the unit. Finite volume method was used to solve the Reynolds averaged Navier-Stokes equation. A standard 2-equations k-ε turbulence model was used in solving this problem. Special techniques were applied for modeling the heat exchanger and the centrifugal fan.

In his work, Xu selected a packaged air conditioning unit that contained many components *(see Figure 1.1)* affecting the flow pattern, including:

- Inlet
- Evaporator coil
- Centrifugal fan
- Outlet
- Filter
- Casing
- Fan motor stand

The evaporator unit used a three-row fin-tube heat exchanger. This geometry was represented by a 2-D computational analysis by introducing a porous medium model. The reason for not selecting a 3-D model and describing the geometry of each tube properly was the huge number of computational cells, which were required for the model.

Another packaged unit configuration was selected for CFD modeling in a separate work by Xu et al., [4]. The unit layout *(see Figure 1.2)* provided similar components to the above-mentioned one but with different arrangement of components aimed to improve flow pattern.

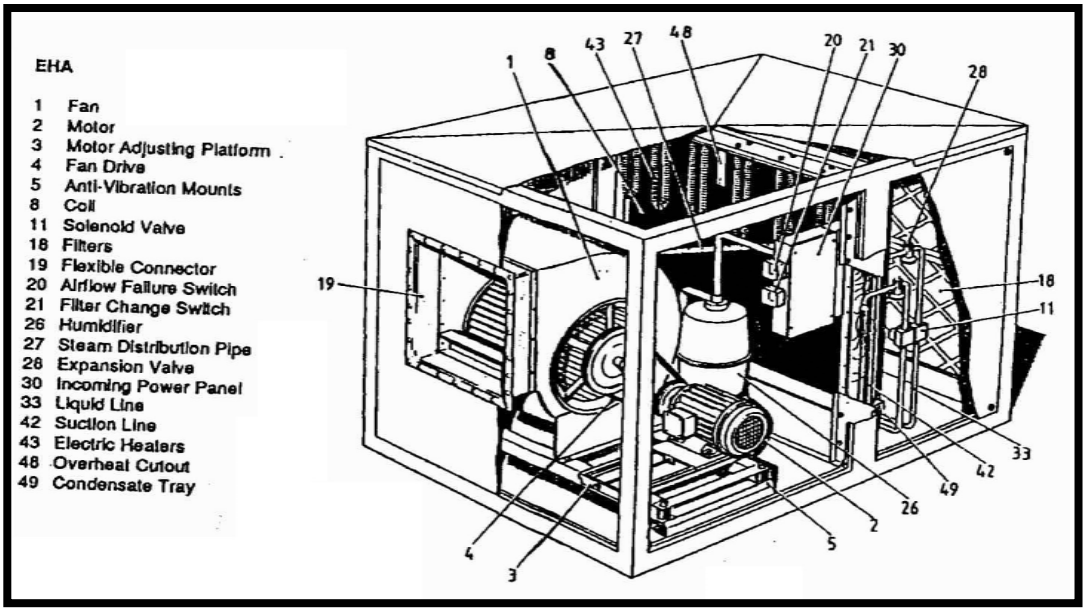

Figure 1.1. Sample packaged unit.

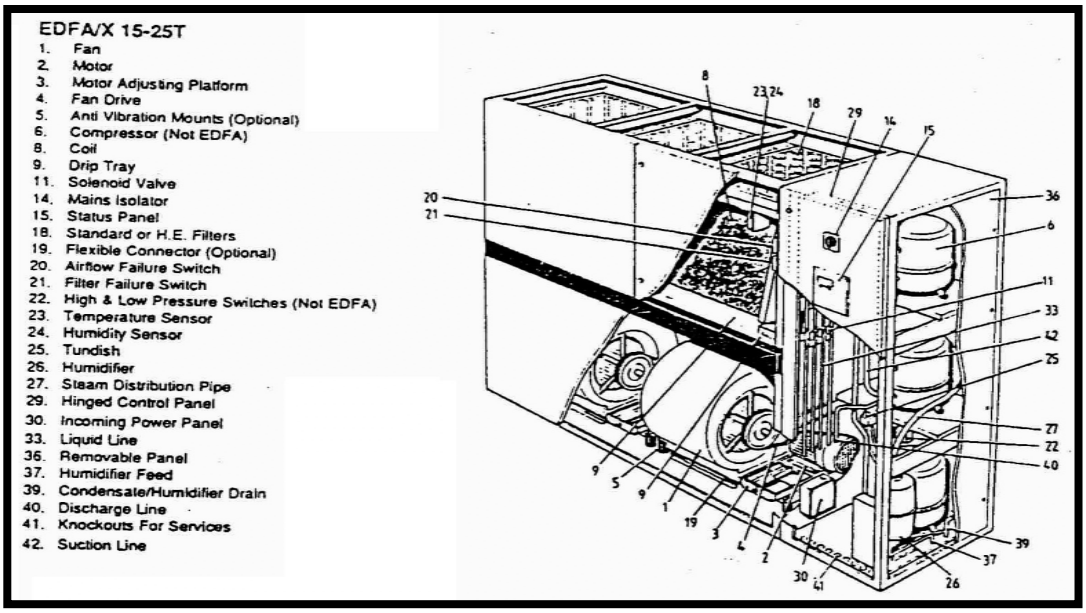

Figure 1.2. Packaged unit with different configuration.

1.2.1.1 Mathematical Model

In setting an appropriate mathematical model of the physical domain of the packaged unit. Xu et al ., [1] introduced following considerations:

a. Physical domain was three-dimensional.
b. Reynolds-averaged Navier-Stokes equations were used as governing equations.

Also, following assumptions were taken:

a. Steady flow.
b. Incompressible flow (low Mach number; less than 0.2).
c. Isothermal flow (no heat transfer was considered).
d. Humidity and Buoyancy effects on air were neglected.

Boundary conditions in three-dimensional domain were required to solve the elliptic form of the partial differential equation. Uniform velocity boundary was assumed at the inlet face of the unit, while pressure boundary was taken at the outlet face. The unit wall was treated by wall function method, which draws a profile of non-dimensional velocity component parallel to the wall.

Centrifugal fan was represented by a source term in the momentum equations for regions bounded by impeller inner and outer diameters. The body force is Coriolis and the centripetal forces in vector notations:

$$B = 2(\omega \times U) + \omega \times (\omega \times r) \tag{1.1}$$

where, ω is angular velocity of the rotation about a fixed axis, and r is the radius.

Heat exchanger was treated as distributed flow resistance unit by introducing porous media model, which applies averaged conservation on the Navier-Stokes and continuity equations in a small control volume as follows:

$$\frac{\partial k_{jk} U_k}{\partial x_j} = 0 \tag{1.2}$$

$$\rho \frac{\partial}{\partial x_j}\left[k_{jk} U_k U_i\right] = -\gamma \frac{\partial P}{\partial x_i} + \frac{\partial}{\partial x_j}\left[(\mu + \mu_i) k_{jk} \frac{\partial U_i}{\partial x_k}\right] - \gamma R_{ij} U_j \tag{1.3}$$

where, γ : volume porosity

k_{ij} : area porosity

R_{ij} : distributed resistance

The distributed resistance that accounts for flow blockage and turbulent diffusion was expressed in terms of drag coefficient, which is a function of fin-tube geometry, fluid properties and local mass flow rate. This coefficient was performed by applying Hewitt (1990) correlation's for staggered tube configuration as follows [1]:

$$C_D = 0.62 + 0.5 \times 10^{-6}\,\mathrm{Re} - 6.3 \times 10^{-12}\,\mathrm{Re}^2 + 10.7 \times 10^{-18}\,\mathrm{Re}^3 - 5.2 \times 10^{-24}\,\mathrm{Re}^4 \tag{1.4}$$

where, Re is Reynolds Number.

In other work by Gothman (1993) [3], turbulent flow through the tube bank of evaporator coil was modeled in the same manner (porous medium model) as a uniform distributed flow resistances. It was formulated by two concepts as follows:

1. Porosity factor, which was defined as a fraction of the control volume available to the fluid flow.
2. Darcy coefficient, that accounted for additional pressure loss across the coil.

The benefit of using porous media model was to have coarser computational grid by avoiding the details of fin and tube. Its disadvantage was the uncertainty and potential error. To avoid errors, the specified Darcy coefficient should be obtained from the experimental values of pressure drop across the coil.

Due to lack of computing power encountered in industrial and engineering applications, solving this 3-D turbulent flow problem (especially in packaged unit case) was not practical. Instead, 2-D representation of turbulent flow through individual tubes in the coil was used. It was observed that the flow through the coil was nearly two-dimensional. Therefore, the central symmetrical plane is selected to simply produce a pressure drop data at different conditions.

A body fitted curvilinear grid system was selected by Xu et al., [1] since it conformed to a curved surface of geometry. In developing a complete grid system, a method called "masking" was introduced. In this method, a complex geometry was broken down into a number of components or blocks. A separate grid was generated for each component by either method (algebraic or elliptic). Then, they were patched together to form a complete grid. In this system, the unit was first broken down into an evaporator coil, condensate tray and outer casing.

1.2.1.2 Numerical Solution

In separate work by Xu et al., [3], numerical solution was performed on the flow inside the same packaged unit by applying finite volume methodology. The governing flow equations were discretized using a non-staggered grid in the physical domain.

The convergence behavior of the three schemes (hybrid, upwind and quick schemes) was presented in terms of mass residual. The results of mean and vertical velocity profile downstream the coil, were presented for numerical and experimental analysis. From which, the peak of this profile was noticed upper the condensate tray. This suggests an underestimation of re-circulation zone beneath the condensate tray. It is well known that the standard k-ε often leads to under-prediction of re-circulation zone [3].

It was observed that quick scheme has produced results better than other (upwind and hybrid) compared to experimental profile. The predicted flow field inside the unit was presented in velocity vector plot. It was based on quick scheme approach. The region of negative velocity exhibited re-circulation region, which was resulted from inertial forces of the fluid over the sharp edges and turbulent effect.

1.2.1.3 Experimental Investigation

In the experimental investigation of Xu et al., [1], triple hot wire anemometry was used in measuring the velocity distribution in the unit. It reported mean velocity downstream of the evaporator coil. The fluid was assumed to enter the system with uniform axial velocity profile of 2.6 m/s (511 ft/min), and discharged to the atmosphere at the exit with a barometric pressure of 1.013 bar. The flow was considered to be turbulent based on Reynolds number calculated which reached 5.84 x 10^4.

The experimental results of Xu et al., [1] comparatively agreed with the computational ones. Some discrepancies of the results occurred due to following reasons:

- Drip eliminator was simplified for computing purposes by limiting the number of grids employed.
- Coil was treated as a uniform resistance unit for numerical modeling.
- Re-circulation in the near wall region of the unit.
- Accuracy of 3-hot wires probe measurements, it was unable to discriminate between positive and negative velocities.

1.2.2 EVAPORATOR PERFORMANCE

1.2.2.1 Airflow Maldistribution

Non-uniform airflow in packaged air conditioning unit was resulted from design and various components assembly in the flow stream. Evaporator performance was affected by airflow maldistribution, by means of reducing the tendency of heat transfer across the heat exchanger.

In latter tests performed to evaluate this phenomena by Aganda et al., [2], a single circuit of 33 tubes evaporator was mounted in a wind tunnel test section. A maldistribution was created artificially by mounting perforated plate upstream to the evaporator covering 50% of its area. The experiments were conducted at mean velocities of 3-4 m/s and 30^{o}C air inlet temperature. However, this work did not cover the physical airflow distribution in packaged unit (complex and 3-D).

Aganda et al., [2] observed that airflow maldistribution leads to refrigerant maldistribution due to uneven loading of evaporator circuits. This means that resulted poor performance in one circuit would affect the other circuits having good airflow distribution.

A program of cross flow heat exchanger called ACOL5 was used for studying this phenomenon. The effect of airflow maldistribution on the performance of a multi-circuits evaporator was evaluated. Evaporator coil of packaged air conditioning unit was selected (manufactured by Airedale International Air Conditioning). Actual velocity was taken upstream and normal to the evaporator. Each evaporator circuit was evaluated separately as a function of air mean velocity and flow distribution on to it. Also, the effect of airflow maldistribution on refrigerant condition was discussed. The effect of multi-pass circuits on evaporator performance was considered.

The packaged unit studied by Aganda et al., [2] is presented in Figure 1.3. It shows the main components including inlet, filter, evaporator, humidifier, electrical heaters, control box and a centrifugal fan. The evaporator dimensions were 600x610-mm height/width of copper tubes mechanically bonded to aluminum fins. It had 7 refrigerant circuits, 4-18 and 3-16 pass each of 5 rows tubes, and of 3/8 in. I.D. tube. The refrigerant (controlled by thermostatic expansion valve) fed to the circuits through distributor. Condensate tray was located beneath the evaporator, which obstructs the flow upstream and downstream of the evaporator *(see Fig 1.3)*.

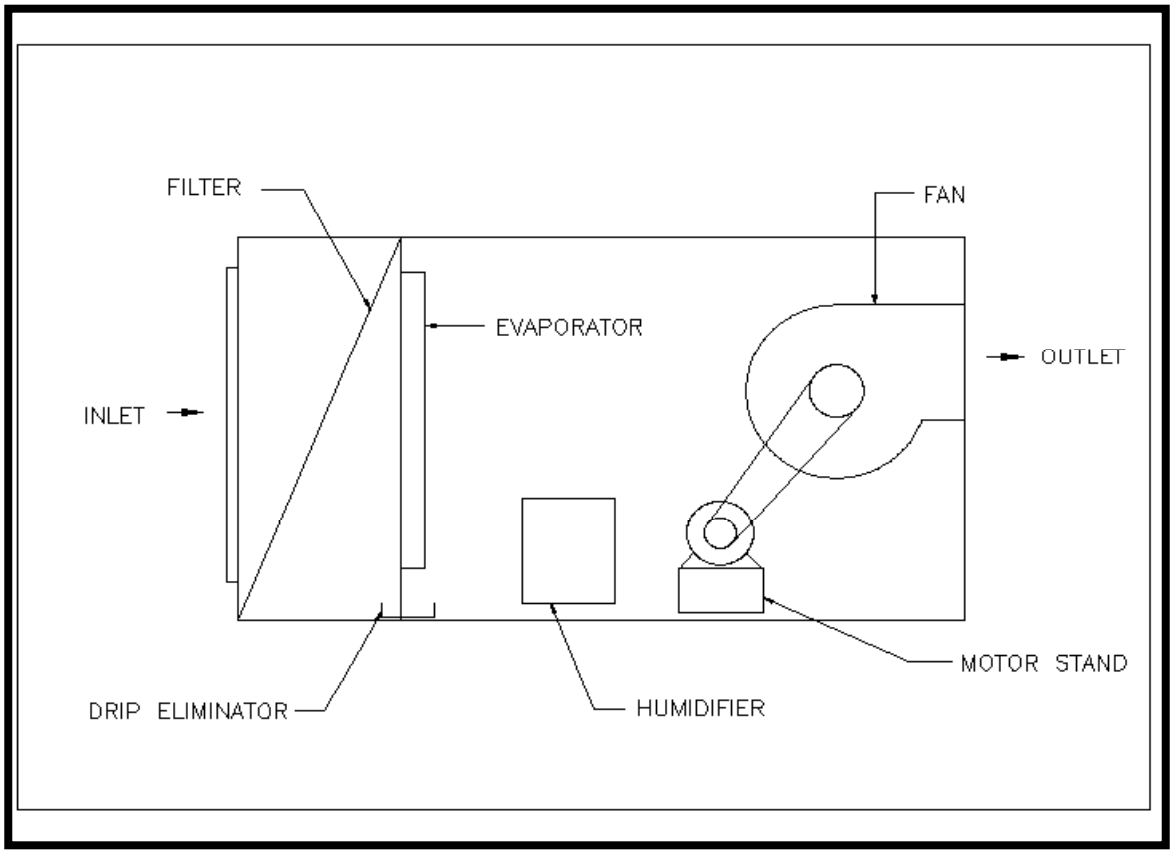

Figure 1.3. Front view of packaged air conditioning unit.

The evaporator performance was observed using ACOL5 code, with parameters such as entering/leaving temperatures and mass flow rates of each streams fluid. The tested evaporator was of 3-15 and 4-20 pass circuits. The investigation was as follows:

1. The performance at uniform air distribution was evaluated (for both 15 and 20 pass separately).
2. The non-uniform airflow distribution was investigated as provided at 50 mm upstream of the evaporator (velocity contour). Here, normalized mean velocity of 2.55 m/s was calculated from this distribution.
3. The performance of the evaporator was considered at the normalized mean velocity.

The effect of airflow maldistribution on one refrigerant circuit was having less outlet refrigerant temperature (partially in 2-phase flow or not superheated). It affected the expansion valve operation. This means, the valve will reduce the refrigerant mass flow rate fed in the whole evaporator circuits to satisfy supper heat condition for the system operation. The result was reducing heat transfer in all circuits due to less refrigerant mass flow rate in tube circuits. This investigation cannot be verified experimentally, because it could not handle each circuit separately, also it cannot treat passes of different tubes [11].

In the same study by Aganda et al., [2], normalized air velocity (normalized mean air velocity) was presented for each circuit across the evaporator width (50mm from the evaporator). These normalized air velocity distributions were used to predict the performance of each circuit (Table 1.1).

Table 1.1: Normalized air velocity at each refrigerant circuit.

	Normalized Air Velocity Across Evaporator							
	Evaporator Width, mm							
Circuit No.	0	100	200	300	400	500	600	Mean Velocity, m/s
1	0.93	0.94	1.07	1.10	1.05	1.00	0.63	2.41
2	0.80	0.86	0.93	1.01	1.06	1.20	0.70	2.64
3	0.85	1.05	1.08	1.07	0.98	1.10	0.60	2.48
4	0.80	0.90	1.03	1.10	0.98	0.90	1.00	2.54
5	0.80	0.92	1.06	1.10	1.01	0.92	0.62	2.73
6	0.70	0.90	1.10	1.20	1.13	1.02	0.80	2.47

To determine the effect of velocity distribution only, the mean velocity was considered (which is in this case 2.5 m/s). A small variation in this value based on measurements in each circuit was considered as seen in Table 1.1. The performance of each circuit having the same mean velocity of 2.5 m/s but with the airflow distribution is shown in Table 1.2:

Table 1.2: Experimental mean air velocity = 2.55 m/s.

Circuit No.	Refrigerant Outlet Temperature, ^{o}C
1	17.9
2	18.1
3	18.1
4	17.9
5	17.9
6	18.0

1.2.2.2 Full Size Evaporator Performance

The performance of six circuits using the actual mean velocities is presented in Table 1.3. If constant mean velocity was considered, then the outlet refrigerant temperature became 18.5°C.

Table 1.3: Performance at actual mean air velocity.

Circuit No.	Mean Air Velocity, m/s	Refrigerant Outlet Temperature, °C
1	2.41	17.1
2	2.64	19.1
3	2.48	18.8
4	2.54	18.3
5	2.73	19.8
6	2.47	17.9

Thermostatic expansion valve was used to control mass flow rate by sensing refrigerant temperature at the outlet. In case of one circuit, it presented the lowest mean air velocity leading outlet refrigerant temperature in two-phase. This led expansion valve to throttle the flow to insure weather refrigerant was supper heated from the lowest performing circuit. This farther reduced flow through all circuits and finally lowered heat transfer in the evaporator. Increasing number of passes per circuit modified temperature of refrigerant at the outlet. It compensated some effects of airflow maldistribution.

1.2.3 DESIGN PARAMETERS AND OPTIMIZATIONS

1.2.3.1 Heat Transfer and Pressure Drop

The effect of the various kinds of design parameters of the heat exchanger is considered in evaluating its performance. They are recognized by means of heat transfer and pressure drop char-

acteristics. The basic design parameters for slit-fins were systematically visualized by Jeom-Yun Yul et al., [6]. Taguchi method was implemented to perform parametric study on each design parameter. It aimed to evaluate their effect individually and interactively with others, on the performance of the heat exchanger. Also, it seeks to identify the main factors for optimum design. Introducing heat transfer coefficient as follows:

$$h = \frac{Q}{A\Delta T_{am}} \tag{1.5}$$

where ΔT_{am} is arithmetic mean temperature difference.

Colburn factor (j) & friction factor (f):

$$j = \frac{hp_r^{\frac{2}{3}}}{\rho C_p \overline{V}} \tag{1.6}$$

$$f = \frac{D_h}{L}\frac{2\Delta p}{\rho \overline{V}^2} \tag{1.7}$$

where, Δp is pressure drop and V is average velocity.

An increase in heat transfer yields an increase in pressure drop due to building of frictional losses in air conditioning systems. Their effects are difficult to be evaluated simultaneously by their respective parameters (j and f). Then, a relevant non-dimensional parameter is needed to define both heat transfer and flow friction effect simultaneously. One criterion introduced Goodness factor, which was proposed to compare thermal and dynamic performance of heat exchanger. It was obtained by ratios between tested and reference (provided) heat exchanger performance as worked out by Jeom-Yul Yun et al., [6]. Those ratios were formulated by introducing h (heat transfer coefficient) and P/A (friction power dissipated per unit surface area) as a functions of j and f respectively:

$$h = \left(\frac{\rho c_p}{\mathrm{Pr}^{2/3}}\right)j\overline{V} = \left(\frac{\mu c_p}{\mathrm{Pr}^{2/3}}\right)j\left(\frac{\mathrm{Re}}{D_h}\right) \tag{1.8}$$

$$\frac{p}{A} = \left(\frac{\rho}{2}\right)f\overline{V}^3 = \left(\frac{\mu^3}{2\rho^2}\right)f\left(\frac{\mathrm{Re}}{D_h}\right)^3 \tag{1.9}$$

Where, Re = ρ V D_h / μ , is Reynolds Number, and ρ , V, D_h and μ are density, average velocity, hydraulic diameter and dynamic viscosity of air respectively.

Dividing above two equations by the corresponding parameters of the reference heat exchanger, which finally cancels constant properties as follows:

$$\frac{h}{h_R} = \frac{j\left(\mathrm{Re}/D_h\right)}{j_R\left(\mathrm{Re}/D_h\right)_R} \tag{1.10}$$

$$\frac{P/A}{\left(P/A\right)_R} = \frac{f\left(\mathrm{Re}/D_h\right)^3}{f_R\left(\mathrm{Re}/D_h\right)^3{}_R} \tag{1.11}$$

Combining the two equations:

$$\frac{h/h_R}{\left\{\left(P/A\right)/\left(\left(P/A\right)_R\right)\right\}^{1/3}} = \frac{j/j_R}{\left(f/f_R\right)^{1/3}} \tag{1.12}$$

Then,

$$JF = \frac{j/j_R}{\left(f/f_R\right)^{1/3}} \tag{1.13}$$

This JF is a combined dimensionless number. It is directly proportional to the performance characteristics of the heat exchanger (higher JF number means batter characteristics). It can effectively evaluate thermal and dynamic performance of the heat exchanger.

1.2.3.2 Factors and Levels

The control factors (variable design parameters) applied to optimize the fin-and-tube heat exchanger were 7 factors. They are related to heat transfer surface area and turbulence in the air-side. Each factor was provided in a number of levels as in Table 1.4 *(see Figure 1.4 for description of the factors)* [6].

T able 1.4 : Control factors with their respective levels.

Code	Factor (unit)	Level 1	Level 2	Level 3
A	Fin pitch, P_f (mm)	1.49	1.34	1.2
B	Slit Height (mm)	1/3 P_f	½ P_f	2/3 P_f
C	Number of slits	6	8	6
D	Slit length (mm)	10	8	10
E	Number of slit divisions	1	2	1
F	Raised angle of slit	45	35	25
G	Angle of slit pattern (inlet angle/outlet angle	0/0 30/30	0/30 0/0	30/0 30/30

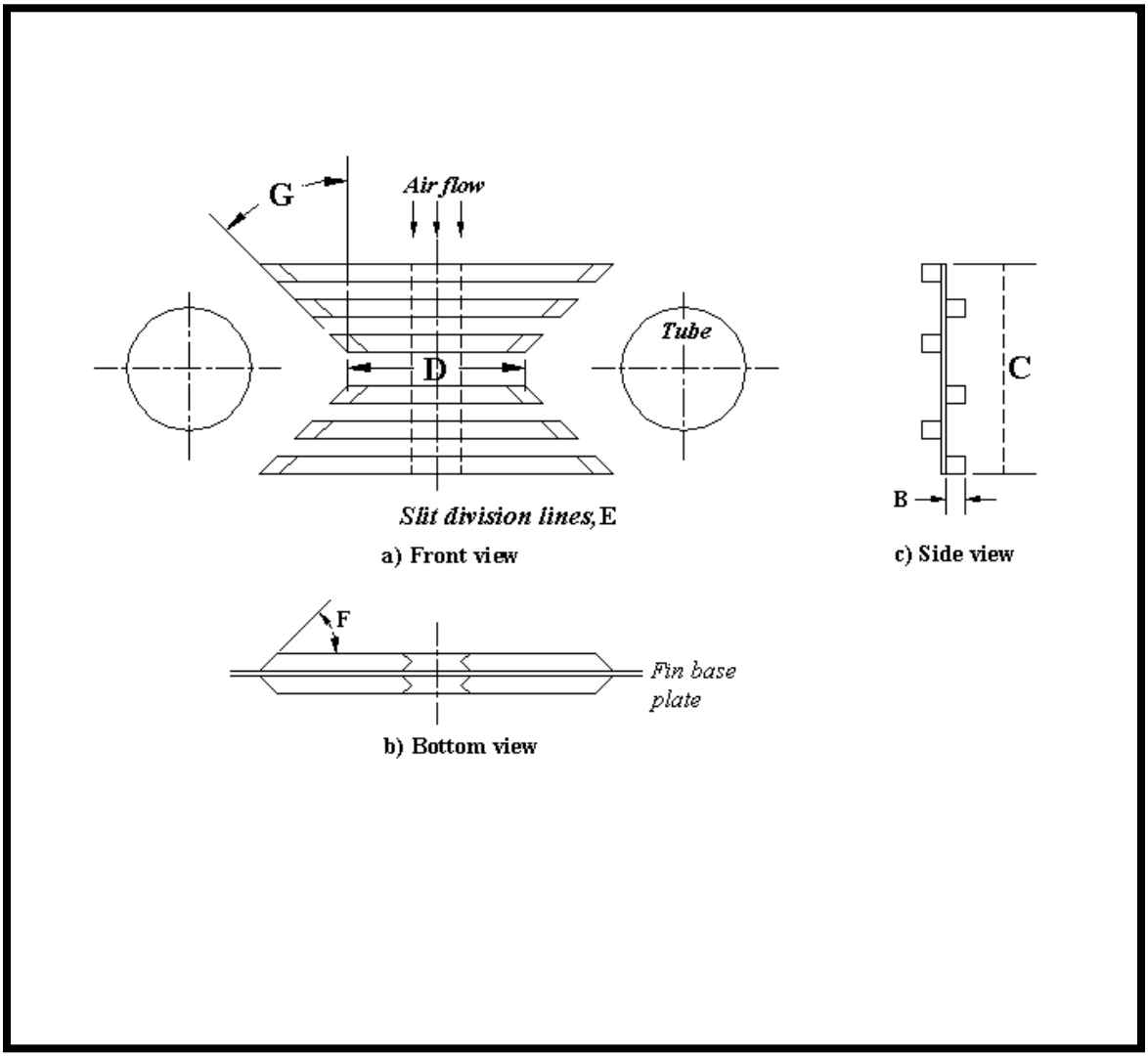

Figure 1.4. Description of the control factors in fin design.

The air velocity was taken as a signal factor in which it defines dynamic performance of the heat exchanger. Noise factors are not considered here; also fixed factors are not affecting parametric study such as fin thickness, step pitch and others.

Experimental matrix has used orthogonal array of 18 samples of combined geometric factors. These samples were used to manufacture various shapes of the fin by coordinating the level. Eighteen samples were made by combination of levels on the orthogonal array; every combination shall conduct one test.

In order to evaluate each control factor performance, we can transform the data into SN ratio. The SN ratio evaluated in this study is defined by dynamic characteristics:

$$SN = \eta = 10 \log [1/r \ (S_m - V_e)/V_e] \tag{1.14}$$

$$r = \sum V_i^2 \ , S_m = [\sum (V_I JF_I)]^2 / r \tag{1.15}$$

$$V_e = S_e / (n-1) \ , S_e = S_T - S_m \ , S_T = \sum JF_i^2 \tag{1.16}$$

Note: V_I (air velocity) is taken at 11 reference points.

1.2.3.3 Factorial Effect and Contribution Ratio

Table 1.5 below shows SN ratios calculated from 18 tests based on combinations of the different factor levels.

Table 1.5: SN ratio for evaluating performance at different factor levels

Number of Test	Control factor							SN Ratio
	G	A	B	C	D	E	F	
TS1	1	1	1	1	1	1	1	17.13799
TS2	1	2	2	2	2	2	2	17.27338
TS3	1	3	3	3	3	3	3	18.34859
TS4	2	1	1	2	2	3	3	16.72726
TS5	2	2	2	3	3	1	1	17.98196
TS6	2	3	3	1	3	1	2	18.63592
TS7	3	1	2	1	2	2	3	17.21723
TS8	3	2	3	2	1	3	1	17.55372
TS9	3	3	1	3	1	3	2	17.30539
TS10	4	1	3	3	2	2	3	17.23327
TS11	4	2	1	1	3	2	2	18.39126
TS12	4	3	2	2	3	1	3	18.63518
TS13	5	1	2	3	1	1	1	16.78063
TS14	5	2	3	1	2	3	3	17.20862
TS15	5	3	1	2	2	2	2	17.92852
TS16	6	1	3	2	3	1	1	17.94397
TS17	6	2	1	3	2	3	2	17.99606
TS18	6	3	2	1	1	2	3	18.35967

The factorial effect and contribution ratio of each factor from those ratios are presented below *(Table 1.6).* The SN ratios of levels on each factor are calculated from the arithmetic average of SN ratios corresponding to each level in previous table. The contribution ratio means the effect of each factor on JF factor (the performance characteristics of the heat exchanger). This is calculated using (R) which indicates the difference between maximum and minimum SN ratio on each factor. As a result, a percentage of contribution is obtained for each factor over total R.

Some of the factors have major effect on the performance of the heat exchanger (see Table 1.6), such as fin pitch (39.28%), angle of slit (28.04%) and slit length (20.16%). Others may have comparatively slight effect like number of slit and their divisions (see Figure 1.5). The optimum condition is obtained by combination of levels showing the largest SN ratio in each factor as presented in table 1.6.

In order to confirm above methods in defining optimum design, a confirmation test is required for validation. To perform re-productivity of the obtained test results, one method is to compare directly the heat transfer coefficient and pressure drop of the optimum condition to the reference fin performance. The other method is to compare JF factor between them.

Table 1.6 : Factorial effect and contribution ratio of each factor.

		Control Factor						
	Level	G	A	B	C	D	E	F
SN ratio (average)	1	17.4463	17.1734	17.5811	17.7164	17.8793	17.6979	17.6992
	2	17.7817	17.7342	17.708	17.677	17.3513	17.7141	17.7218
	3	17.3588	18.2022	17.8207	..	..	..	17.6888
	4	18.0932	..	..	..	..	..	..
R (SN_{max} -SN_{min})	2.619	0.73446	1.02882	0.2396	0.03937	0.52798	0.01621	0.03294
Contribution ratio (%)	100%	28.04	39.28	9.15	1.5	20.16	0.62	1.25

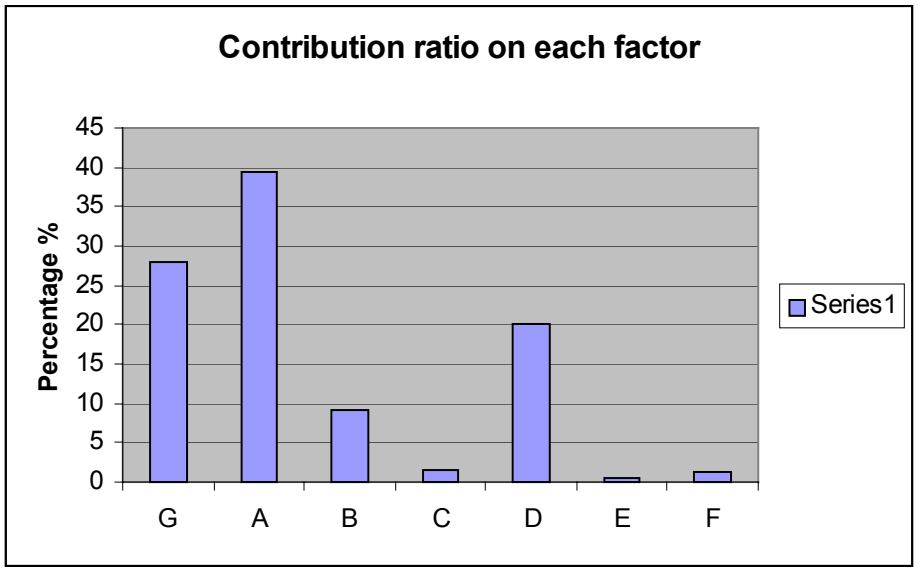

Figure 1.5. Contribution ratio on each factor.

1.3 PROBLEM FORMULATION

1.3.1 INTRODUCTION

In the present work, modeling of airflow and heat transfer in a commercial packaged air conditioning unit is formulated. A CFD (Computational Fluid Dynamic) model is used to simulate the flow in the unit airside. The basic three-dimensional geometry of the unit includes the main components like evaporator, fan, motor, pulley, shaft and others. These components have an effect on the flow pattern across the unit as some of them obstruct flow or cause its non-uniformity.

It is known that flow inside the unit is turbulent which requires a special treatment. A k-ε turbulent model is chosen as a good compromise for representing the flow in such three-dimensional CFD model. The evaporator is treated as a porous media to implement both heat transfer and pressure drop across the heat exchanger. A fan model is used for the centrifugal fan, which delivers air and represents the main component in controlling flow distribution inside the unit.

The present work also involves experimental measurements of the flow characteristics inside the unit. The packaged unit of 25 tons nominal cooling capacity is installed in a psychometric testing room available in Zamil Air Conditioners. The unit is set with a standard operating conditions, such as airflow rate, entering air temperature and relative humidity. Similar operating conditions are applied in the proposed CFD model. An air velocity probe is used for approximate measurement of three components of velocity field. It incorporates data logging system that measures fluctuation of velocity within a specified time scale. Also, the same probe could measure static pressure and air-temperature as it incorporates pressure taps and temperature sensor.

In the last part of the present work, a simplified parametric study is introduced to evaluate the performance of the packaged unit. Different design parameters affecting flow distribution inside the packaged unit are identified. They are related to the position of some components in the construction of the unit. Rearrangement of components positions such as the inlet and outlet faces, fan orientation and/or the evaporator position may create a major change in the flow path of the unit. These changes may produce different airflow distribution across the unit medium. The effect of each design parameter on the thermal and flow performance of the unit is studied.

1.3.2 OBJECTIVES

The main objectives of the CFD model are as follows:

- Modeling of airflow and heat transfer in a packaged air conditioning unit.
- Predicting of the velocity distribution at different locations in the unit.
- Identifying of re-circulation regions generated by the flow geometry.
- Validation of numerical predictions against experimental results.

The experimental validation of the CFD model includes:

- Velocity and pressure measurements at different locations in the experimental unit.
- Comparing the predicted flow characteristics obtained from the CFD model against the experimental measurements.

The parametric study and optimization of the unit will involve a simple CFD parametric study, by varying few design parameters and evaluate their effect on the thermal and flow performance of the unit

1.3.3 PRESENT SYSTEM DESCRIPTION

In the present work, one standard packaged air conditioning unit manufactured by Zamil Air Conditioners as shown in Figures 1.6 and 1.7, is selected for investigation of airflow pattern. This unit is a U-type horizontal flow configuration. The unit is fitted with a wide variety of components classified as both major and minor items. The major components are the evaporator coil, fan housing, fan motor, inlet and the outlet. While the minor components are electric control box, motor support plate, motor pulley and fan pulley. These components are included in a rectangular chassis having overall dimensions of 76.8 in. x 86.6 in. x 53 in. (1.95m x 2.2m x 1.35m). In addition, there is a filter frame immediately behind the evaporator coil and a coil frame.

The evaporator coil is a finned tube heat exchanger with 4 rows of 3/8 in (9.5mm) inner tube diameter arranged in staggered formation. There is a drain pan rigged in the bottom panel under the evaporator coil. The fan is of centrifugal type with double symmetrical side inlets. Air is drawn through the evaporator coil and exchanges heat with the cooling medium flowing through it. The fan discharges conditioned air to the atmosphere through the unit outlet. The standard packaged unit offers 25 tons of nominal cooling capacity. Its standard/nominal airflow rate is 9000 cubic feet per minute (4.25 m^3/s). The average flow velocity at the inlet is 1,846 ft/min (9.32 m/s).

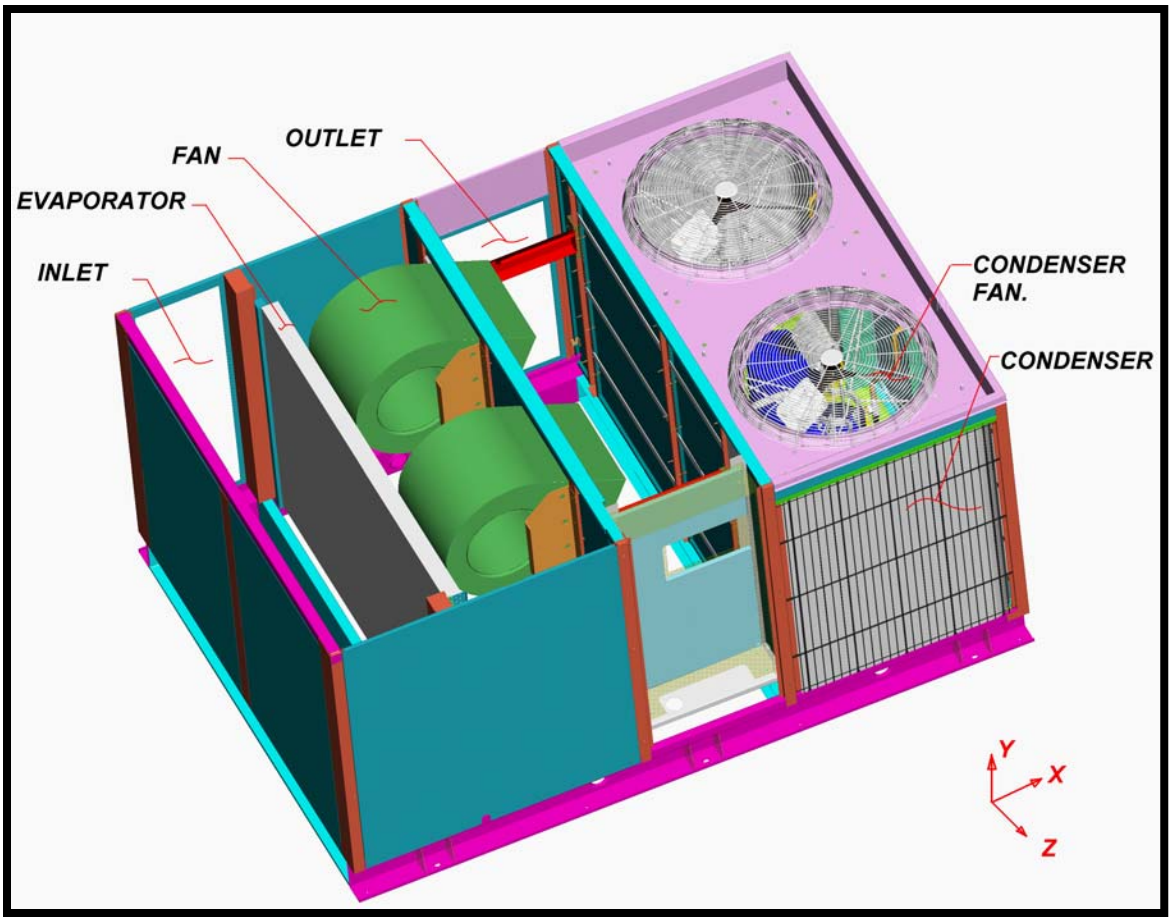

Figure 1.6. Three-dimensional view of the packaged air conditioning unit (PU300).

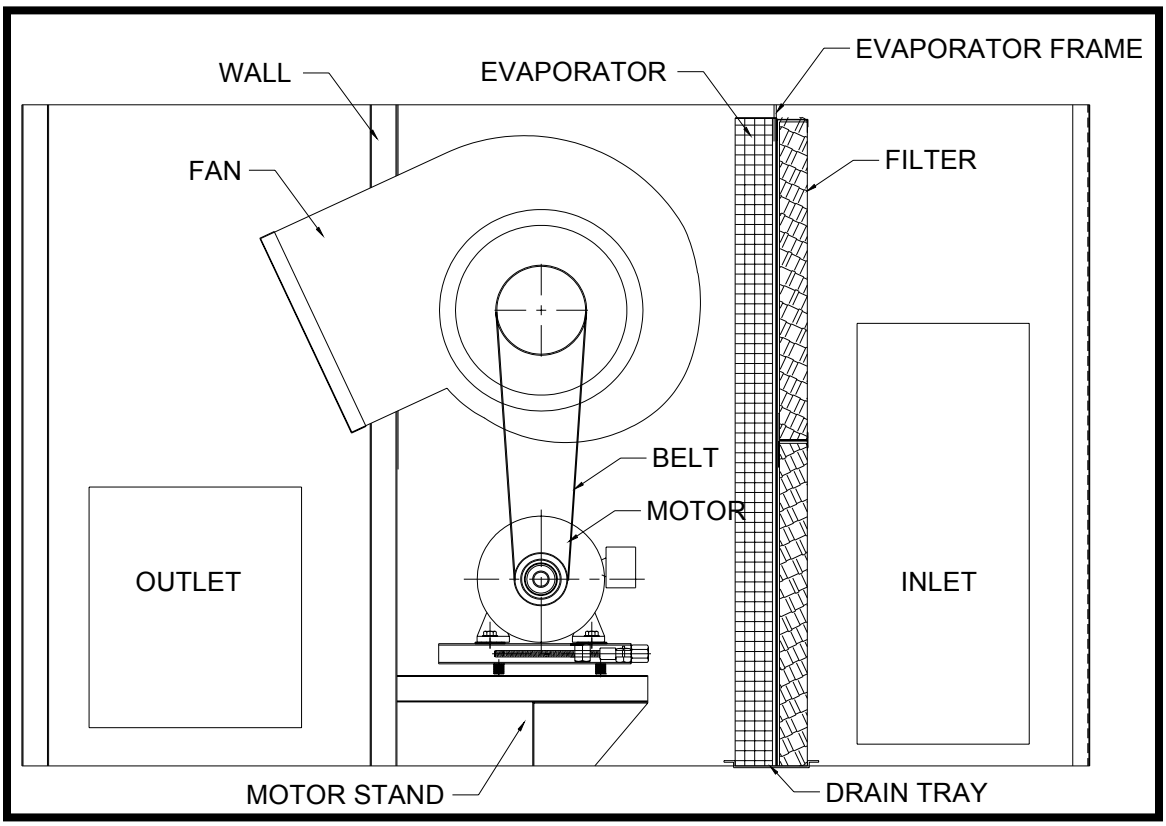

Figure 1.7. Front view of the packaged air conditioning unit (PU300).

CHAPTER 2

EXPERIMENTAL SET-UP OF PACKAGED UNIT

2.1 BASIC SET-UP

Testing is performed on a full-scale experimental model in a psychrometric test room. This test facility is available in Zamil Air Conditioners. The Psychometric test facility consists of an indoor and an outdoor room *(see Figure 2.1)*. The inner room represents the conditioned space and the outdoor room represents the ambient space. Both the indoor and outdoor rooms are set on the standard design conditions. For example, the design room air-temperature in the indoor section is set on 80/67°F Dry/Wet Bulb temperatures (26.6/19.4°C). In order to maintain this temperature, a re-conditioning supply air is continuously fed to the room. The outdoor section in the psychometric room is kept on the standard ambient temperature of Saudi Arabia (115°F or 46°C), with a re-conditioning system supplied to maintain this temperature.

Since in the present work, a packaged unit is considered for testing, and then each half of the unit (evaporator and condenser) is fit in its corresponding section (indoor and outdoor rooms). In the indoor side (cooling section), the supply air from outlet of the unit is connected to a duct which allows air to pass over nozzles for airflow rate and temperature measurements, and latter to

re-conditioning equipment. Both rooms need to remain stable for an hour to maintain air and refrigerant temperatures as per the standard conditions. The psychometric room is practical for cooling and/or heating capacity calculations. In addition, the facility is used for testing the performance characteristics of air conditioning equipment, such as dry/wet bulb temperatures, relative humidity airflow rate and others on both supply and return ducts to the unit.

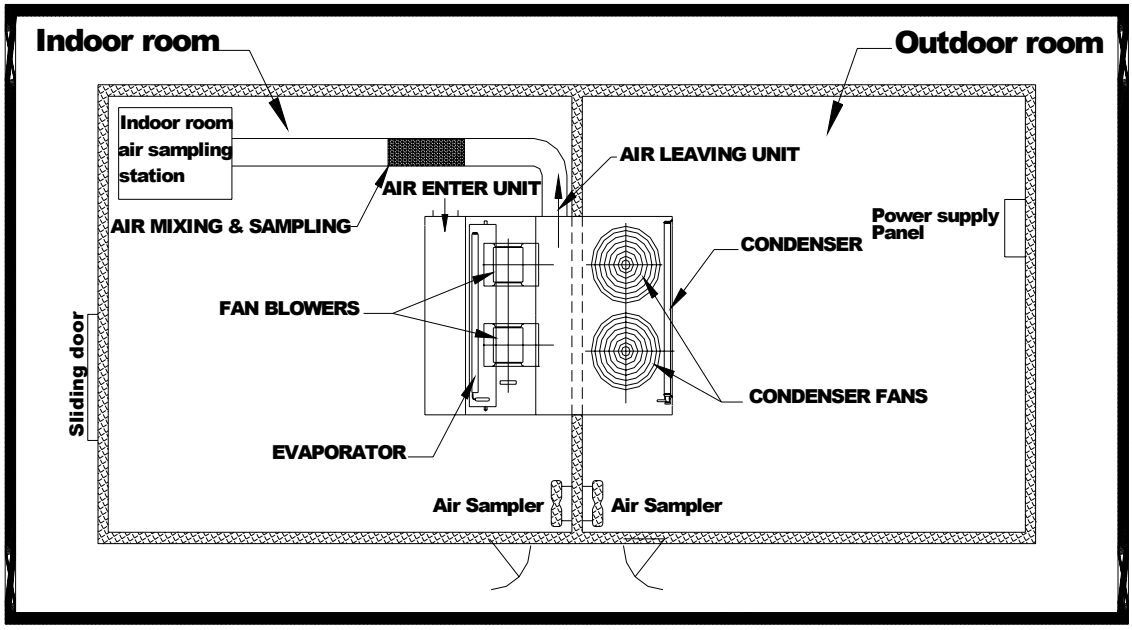

Figure 2.1. Psychometric test room.

The capacity and airflow runs are initiated as per ASHRAE standard 37. This standard uses the air-enthalpy method arrangement, which depends on reconditioning equipment in measuring airflow discharge**.** A data acquisition system records all the psychometric data from which the capacity is calculated as per the standard.

2.2 APPARATUS

The main apparatus used for the experimental test includes a velocity probe with multiple sensors (Figure 2.2). This probe has a velocity range from 0-50 m/s with an accuracy of ±3 % of total range [20]. It has a capability of measuring differential pressure and volumetric flow rate. Also, it has data logging ability of 1,394 samples per test [20].

Figure 2.2. Velocity probe system.

The velocity probe system operates with two sensors: an air velocity sensor and a temperature compensation sensor. The velocity sensor is heated to an elevated temperature (relative to the surrounding air) by means of control electronics. The temperature compensation sensor senses the ambient, or surrounding air temperature and forces the velocity sensor to stay at a constant "overheat" above the ambient. The sensors form two opposite legs of a Wheatstone bridge (Figure 2.3). The bridge circuit forces the voltage at points A and B to be equal by means of an operational amplifier. Air flowing past the velocity sensor tends to cool the sensor, thus driving down its resistance. The operational amplifier responds by immediately delivering more power to the top of the bridge to maintain voltage equilibrium at points A and B. As more air flows past the sensor, more power is required to maintain a balanced bridge. Thus, the power going into the top of the bridge is related to the velocity of the air flowing past the sensor. This is the basic principal of operation for constant temperature thermal anemometers [20].

This probe is used to measure the air velocity components (X, Y and Z) by directing the sensor window normal to the flow in the same axis, see Figure 2.4 that shows schematic of the velocity sensor.

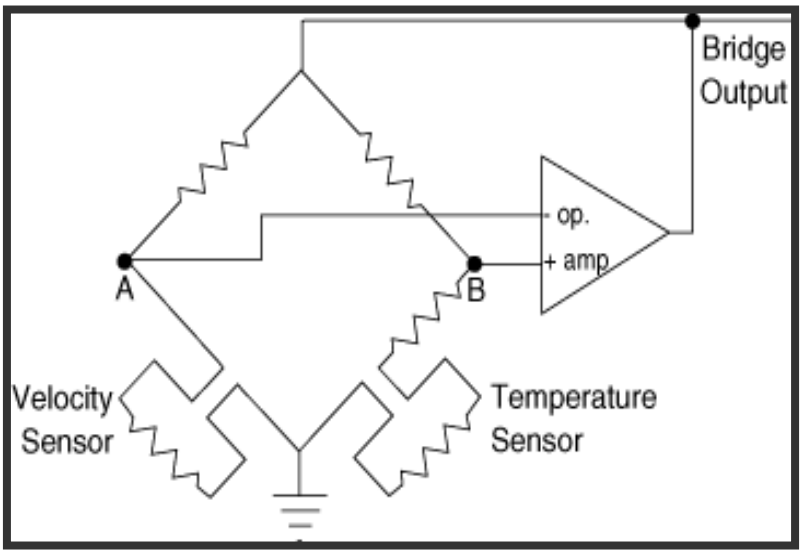

Figure 2.3. Wheatstone Bridge diagram.

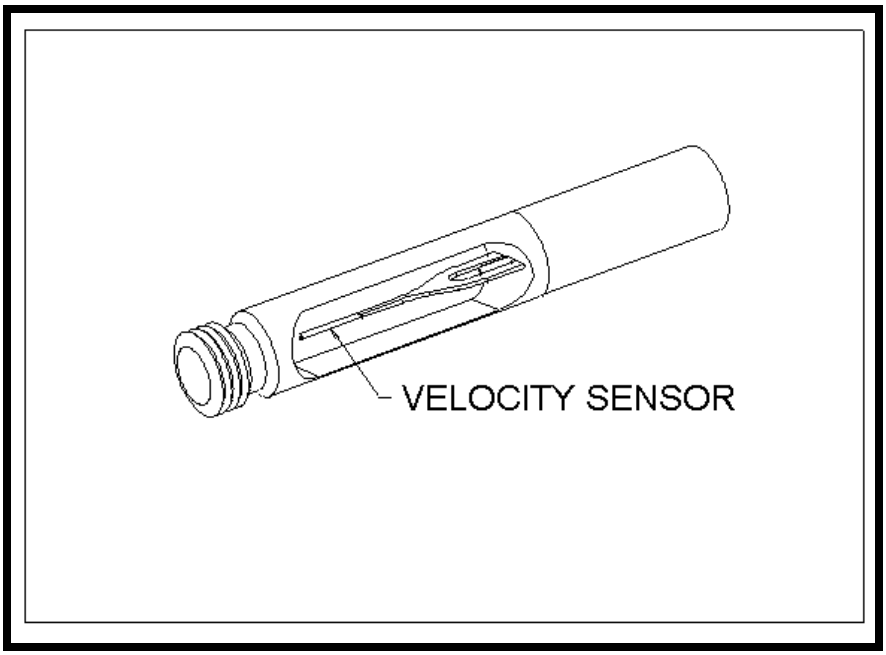

Figure 2.4. Schematic of the velocity sensor.

The minimum measuring time constant offered by this probe is 1 second, but logging takes place after 2-seconds as minimum by averaging the last two measurement values. In the present work, fluctuation of velocity is experienced almost in all regions of the flow, which couldn't be measured with a single data log. To overcome this, multiple measurements are logged within a specified time interval. In some regions of the flow, 90 data log (equivalent to 3-minutes of time interval) are taken for measuring a velocity fluctuation at one specified location. Other regions that have low fluctuations are treated with a lower number of data logs.

2.3 MEASUREMENT SET-UP

Slots are cut on specific sections on each panel of the packaged unit where the measurements will take place. These slots openings are covered again with transparent plastic sheets and glued to prevent any air leakage *(see Figure 2.5 below)*.

The probe measuring end is positioned in the flow field and the opposite end is clamped to the steel panel, using a support bracket on the top panel *(see Figures 2.6 and 2.7)*. For measurements on different sections, similar slots are built on the top and side panels. Small holes are drilled for inserting the probe in the flow field. The velocity probe can be extended to longer distances in the flow field for taking the measurements at far regions. It incorporates a flexible scaled antenna for both extending and/or shrinking its length.

Fig. 2.5 : Slots on the top panel of the unit.

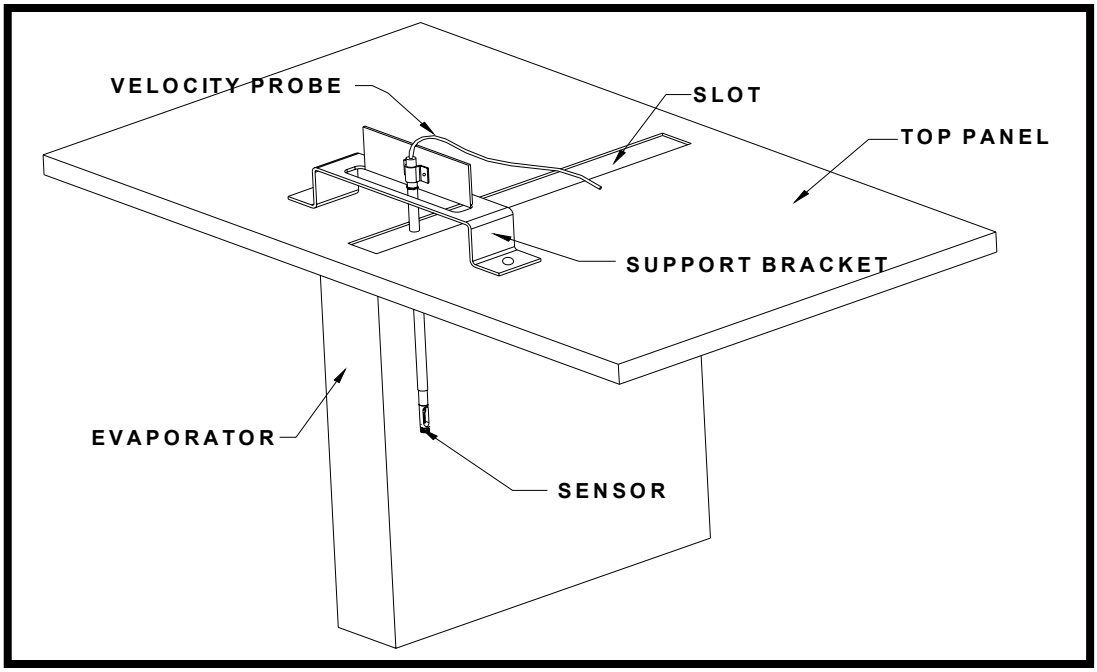

Figure 2.6. Support bracket for fixing the probe inside the slot.

Figure 2.7. Probe mounting form on the top panel of the unit.

2.4 TEST PLANES

The flow inside the unit (PU300) is measured experimentally using the velocity probe described earlier at different planes in the flow field. To facilitate these measurements, several planes in the flow field are identified for the proposed measurements. A group of points that are equally distributed across the surface of each plane are defined, in order to obtain a reasonably accurate view of the actual flow in the chosen plane. The proposed planes are identified in Figure 2.8 that is indicated on the detailed drawing of the PU300 unit (front and top views).

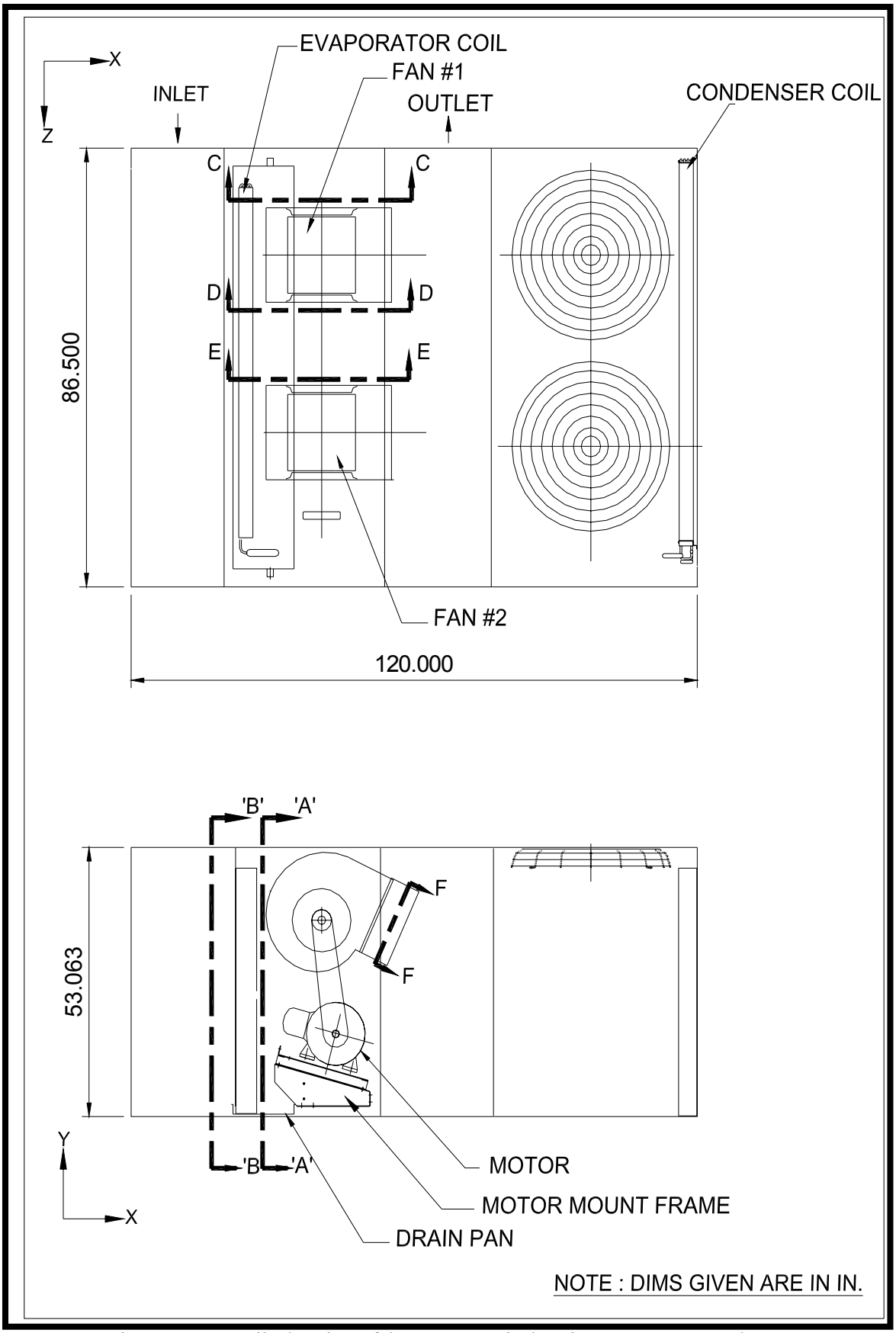

Figure 2.8. Details drawing of the PU300 unit showing measurement planes.

The identified planes in Figure 2.8 are described in Table 2.1. Each plane is provided with a corresponding figure showing its layout, dimensions and locations of the specified measurement points.

Table 2.1: Experimental planes identification.

Plane (Section)	Plane Name	Figure #
A-A	Vertical plane at 1.4 in. downstream evaporator	Figure 2.9
B-B	Vertical plane at 2.4 in. upstream evaporator	Figure 2.9
C-C	Vertical plane at fan inlet # 1 (left face)	Figure 2.10
D-D	Vertical plane at fan inlet # 1 (right face)	Figure 2.10
E-E	Vertical plane at fan inlet # 2 (left face)	Figure 2.10
F-F	Plane normal to fan outlet (both #1 and 2)	Figure 2.11
Inlet and outlet	Plane covers inlet and outlet faces	Figure 2.12

Plane A–A in Figure 2.9 is selected to measure velocity distribution of air leaving evaporator of fin-tube geometry. Plane B-B has similar layout to plane A–A while it is located prior to evaporator coil. It is selected to measure non-uniformity of the flow distribution across the evaporator, which may lead to poor heat transfer across refrigerant tube circuits. The identified planes at various fan inlets in Figure 2.10 are aimed to validate the computational model and check if the fan model built in the code complies with the real fan performance by means of velocity distribution at each fan inlet. Finally, both inlet and outlet planes in Figure 2.12 represent the boundary of the system. These planes are selected to measure the flow rate and velocity distribution at the system boundaries. Each plane is meshed with a group of points equally distanced, and each point is numbered in a sequence based on its location from the respective frame axis.

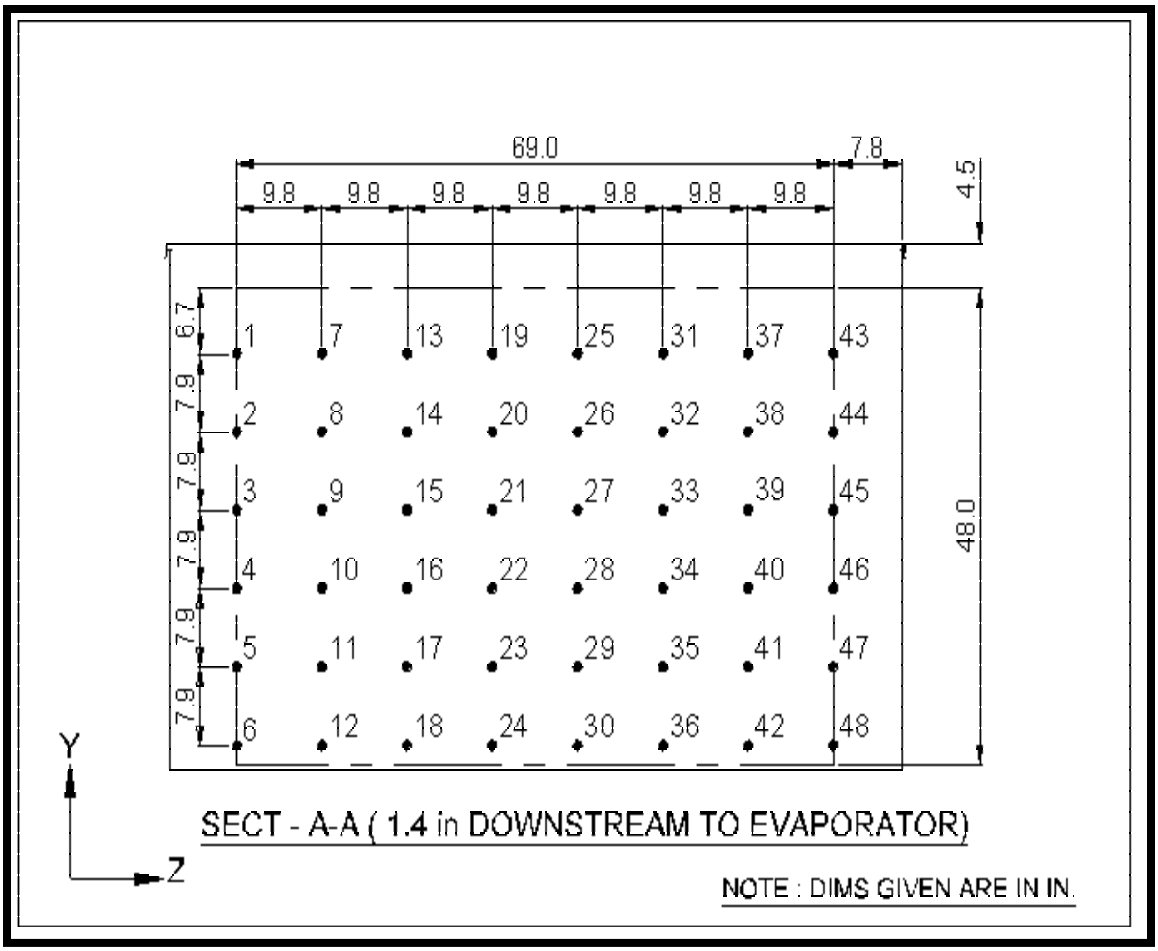

Fig. 2.9. Plane A-A an at 1.4 in. downstream of the evaporator (similar reference for plane B-B).

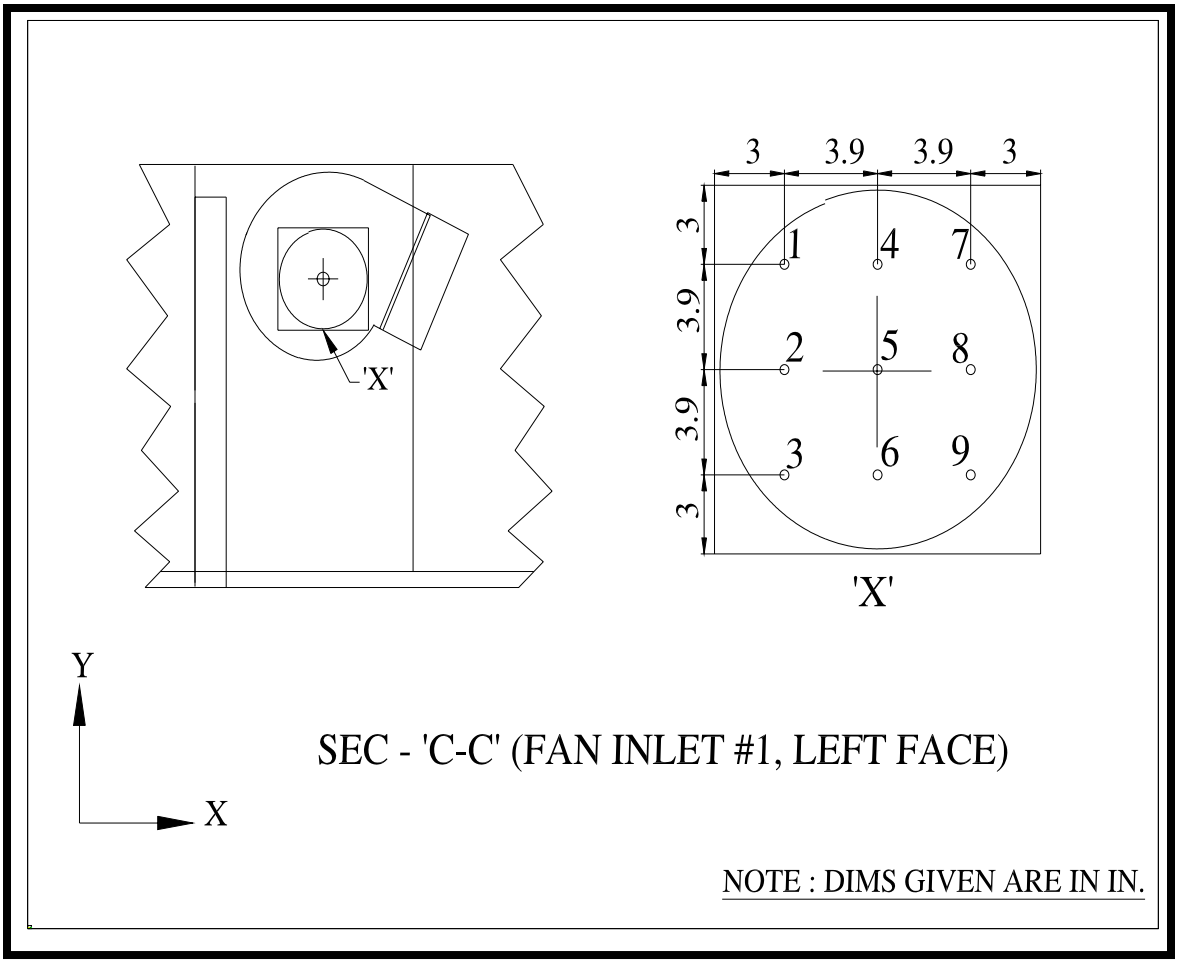

Figure 2.10. Plane C-C at fan inlet # 1 (left face), similar reference for planes D-D and E-E.

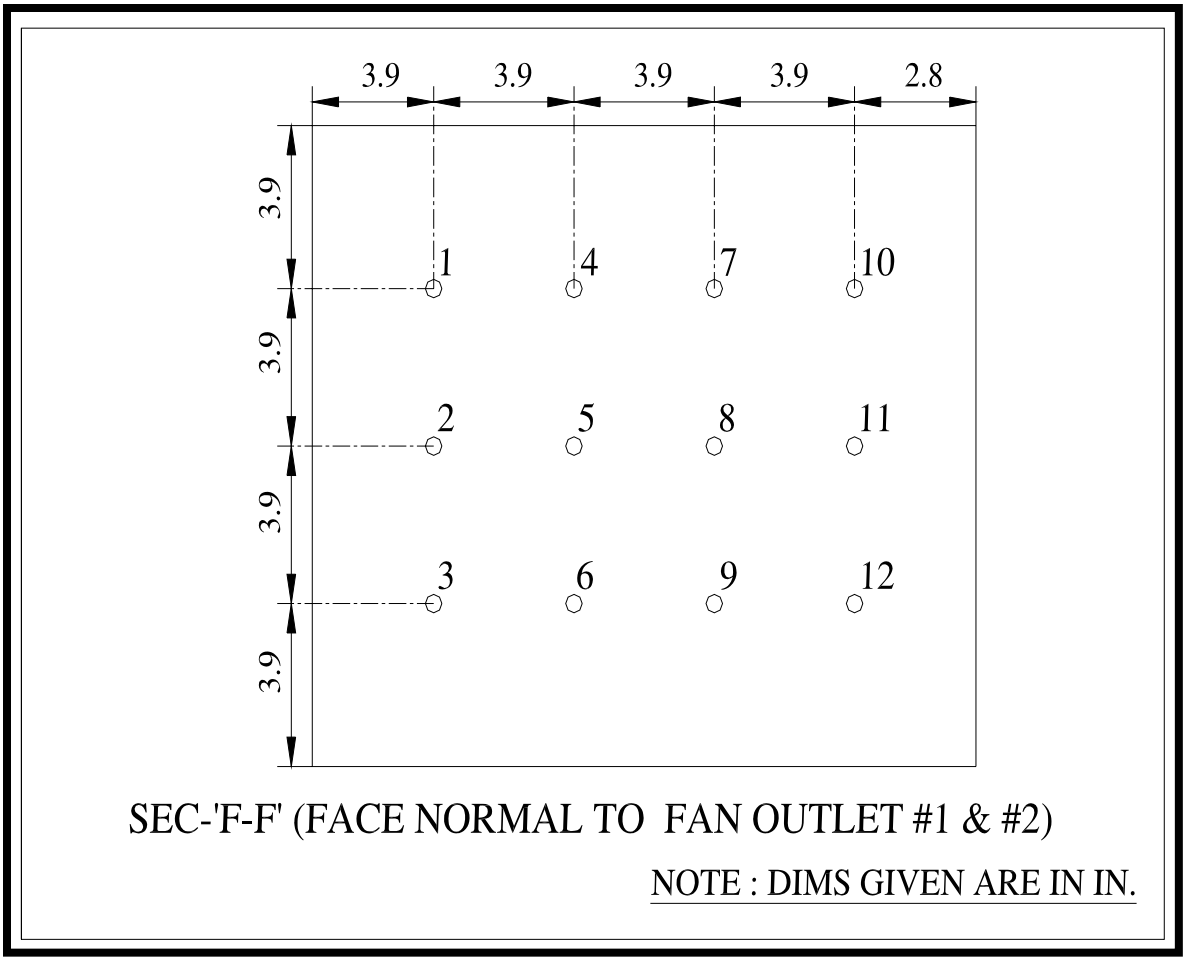

Figure 2.11. Plane F-F normal to fan outlet face.

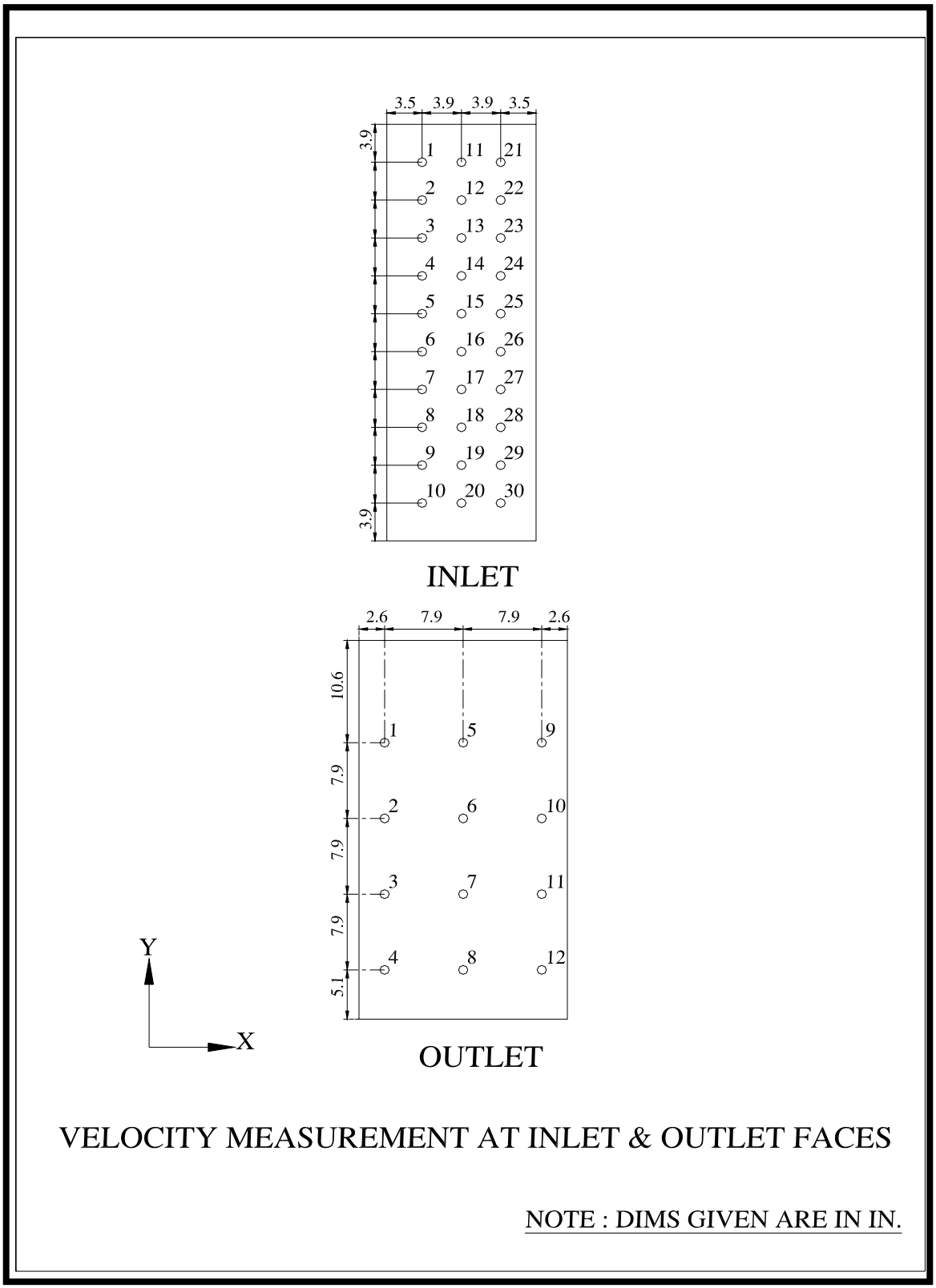

Figure 2.12. Planes show inlet and outlet faces.

CHAPTER 3

EXPERIMENTAL RESULTS

3.1 CONSIDERATIONS

The experimental measurements are taken at the specified planes defined earlier and include the three components of velocity, pressure and the temperature of air. Each plane incorporates a group of measurement points equally distanced on its cross sectional area. The fluctuations of velocity components at some points are estimated. The magnitude of velocity component is considered by taking its absolute value, which is presented in terms of air speed. The root mean square (RMS) is calculated to give an approximate measure of the turbulence intensity.

3.2 ERROR ANALYSIS

The velocity probe used in the measurements of flow characteristics operates within a limited range and logging accuracy. Table 3.1 shows the measurement range and the corresponding accuracy, as per the specifications of the velocity probe.

Table 3.1. Velocity probe operating range.

	Measurement Range	*Accuracy, %*	*Maximum Error*
Velocity, ft/min	0 – 100	----	± 3 ft/min
Velocity, ft/min	100 – 6000 ft/min	± 3%	± (3 – 180) ft/min
Static Pressure, in w.g.	-2 to +1 in w.g.	1%	± 0.02 in w.g.
Temperature, ^{o}F	55 – 62 ^{o}F	----	± 0.5 ^{o}F

Possible measurement errors are also encountered because of the probe mounting on the unit. Mounting the sensor in a high velocity flow field such as near the fan makes it vibrating. This vibration is expected because of the length of the probe end that reaches 1 meter (39.4" in.). This results in errors in the data for velocity and pressure, especially in the far regions that require extending the probe to its maximum length.

Measurement of velocity components needs directing the sensor window normal to the respective axis. A small change in the angle may lead to a false reading of the required velocity component. This is due to the highly non-uniform flow behavior in the unit. In addition, the finite width of the probe window (5 mm) causes redirection and blockage of the flow, hence altering the flow field and reducing the accuracy of the measurement. Another possible error in the experimental measurement refers to an incorrect positioning of the probe sensor in its specified location. For the sake of validating the computational model, it is required to compare the measured and predicted flow characteristics at the same point in the flow field. Small deviation in the orientation of these points may lead to an incorrect validation.

Another disadvantage of the velocity probe is that it measures only the magnitude of the flow speed passing through its sensor window. It does not recognize the direction of the flow. This

makes it hard to know the direction in regions of flow re-circulation where the flow direction is not recognized.

3.3 INLET

The Inlet face is open to the atmosphere. Figures 3.1 and 3.2 show the contours of u and w-air speeds measured at inlet plane respectively. The contours map shows w-air speed component as the dominating one at this plane, where its range is between 2,300 – 2,800 ft/min. The measured u-air speed ranges between 200-500 ft/min. The actual volume flow rate entering the unit inlet is calculated based on the integration of the measured w-air speed component over the surface area of the inlet as follows:

$$Q = \iint w(x, y).dx.dy = 12{,}931\, ft^3/\min \tag{3.1}$$

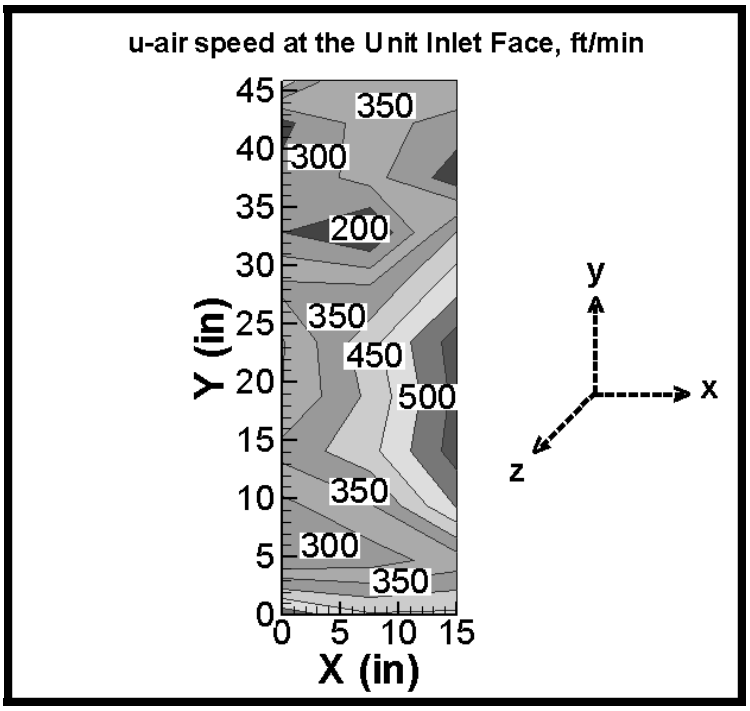

Figure 3.1. u-air speed measured at unit inlet face

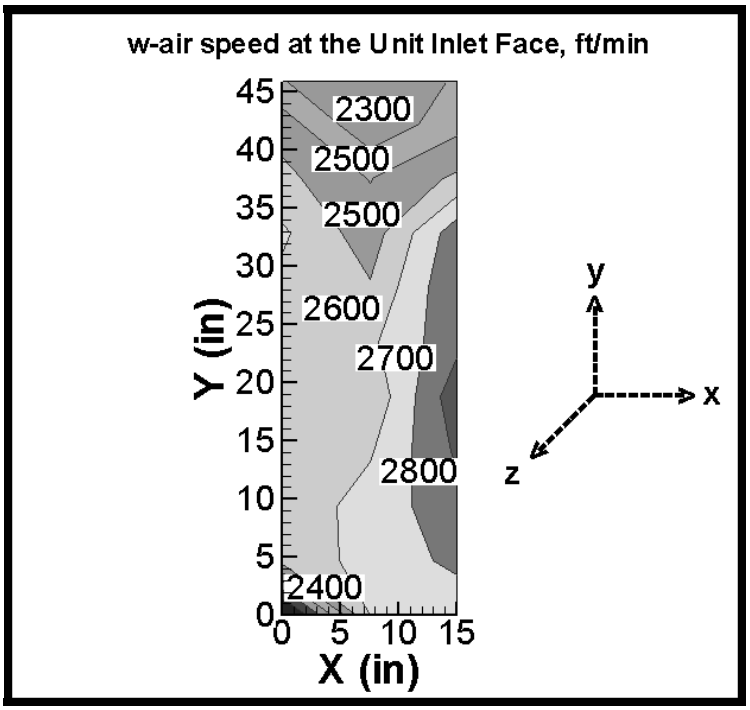

Figure 3.2. w-air speed measured at unit inlet face

3.4 EVAPORATOR

3.4.1 PLANE B–B UPSTREAM OF THE EVAPORATOR

Plane B–B is located at 2.4 in. upstream of the evaporator (see Figures 2.8 and 2.9 for reference). The u-air speed component in the direction normal to evaporator surface is in the 200-900 ft/min range as indicated in Figure 3.3. Flow upstream of the evaporator is of complex nature. Air enters the unit and immediately turns 90° towards the evaporator. Very small distance in the x-direction would not be enough to permit air to straighten in the direction of the evaporator. This is obvious from Figure 3.5 that shows a high w-air speed component of air approaching plane B–B.

The PU300 air conditioning unit is classified to three sections, inlet section, fan section and outlet section. The inlet section is the one situated between the unit inlet and the evaporator. This section is free of flow obstructs which may interrupt the flow inside. The high velocity air entering this section tends to distribute among the wide evaporator area. But, this free space causes part of the flow to diverge from its path and hits the facing wall opposite to the inlet instead of flowing towards the evaporator, which results into flow re-circulation in the inlet section. This is observed experimentally by placing ribbons at the inlet face.

Figure 3.4 shows estimated values (in percent, %) of turbulence intensity. These values vary between 0.5-4 %, which indicates a variable fluctuations of velocity in different regions of plane B–B.

A filter which was normally placed in the unit was removed from its frame upstream of the evaporator in order to facilitate the measurement of plane B–B. The air filter was attached adjacent and upstream of the evaporator. It is concluded that plane B–B is a good location to study flow

behavior upstream of the evaporator, which shows the flow complexity and re-circulation resulting from the design construction nature of the unit.

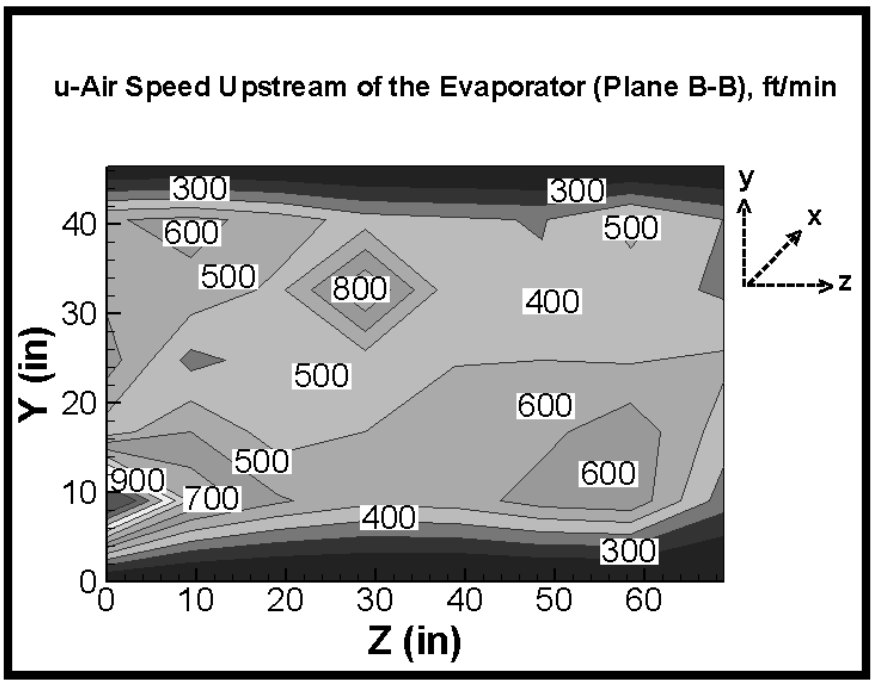

Figure 3.3. u-air speed measured upstream of the evaporator (plane B–B)

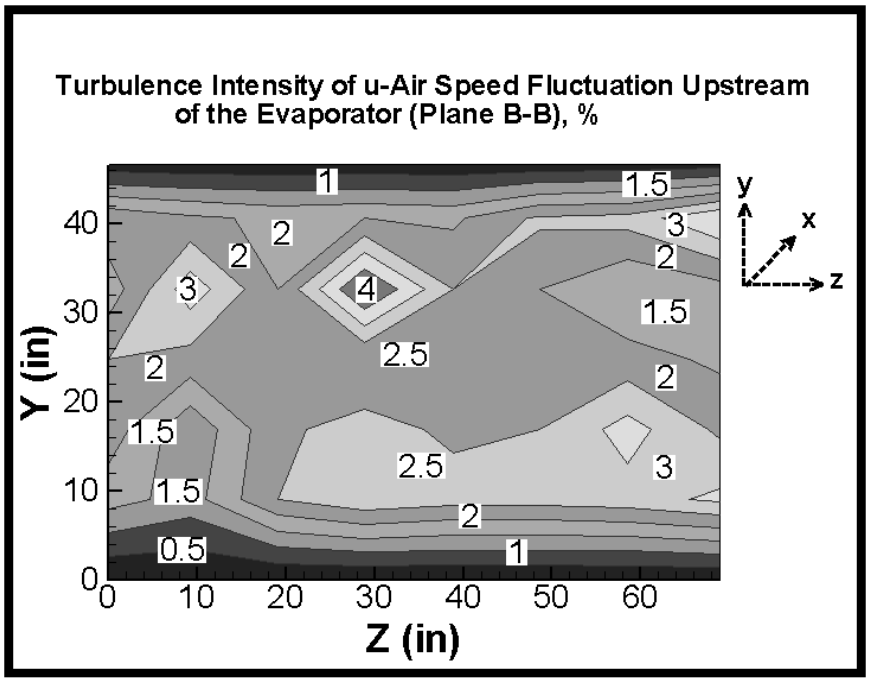

Figure 3.4. Estimated turbulence intensity upstream of the evaporator (plane B–B).

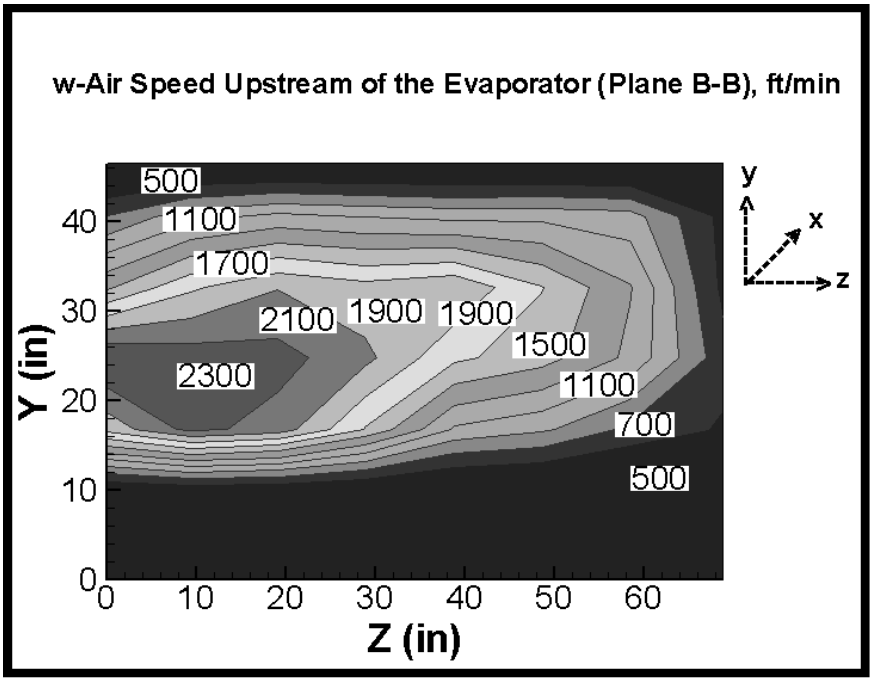

Figure 3.5. w-air speed measured upstream of the evaporator (plane B–B).

3.4.2 PLANE A–A DOWNSTREAM OF THE EVAPORATOR

Plane A–A is positioned at a distance 1.4 in. downstream of the evaporator. Figures 3.6 to 3.9 show the measured air speed components (u, v and w) with the estimated values of turbulence intensity of the u-air speed component. The u-air speed distribution on plane A–A (Figure 3.6) shows that the airflow has a complex behavior as well. Increasing u-air speed values appear in the central region of this plane because of the free area between the two fan housings.

In Figure 3.8, the contour levels of v-air speed component in y-direction fall in the range of 100–200 ft/min in most parts of the plane. This is considerably lower than the u-air speed component. However, there is a small region, which has high v-air speed near the rotating pulley.

In Figure 3.9, higher w-air speed values are noticed in the middle region of plane A–A. This region is located between the two fans.

The actual volume flow rate leaving the evaporator is calculated based on the integration of u-air speed component over the cross sectional area of the evaporator:

$$Q = \int_{A_{evap.}} u \cdot dA \tag{3.2}$$

$$Q \cong \sum U_i \Delta A_i \tag{3.3}$$

The obtained value is 11,960 ft^3/min, which is less than the actual flow rate at the inlet that is equal to 12,931 ft^3/min. In addition to experimental error and the course measurement mesh, the difference may be due to the re-circulation zones upstream and downstream of the evaporator. From Figure 3.6, it is seen that the majority of u-air speed values falls in the range of 400–600 ft/min. This range is well centered close to an estimated average u-air speed of 507 ft/min.

Finally, contours of static pressure measured on plane A–A are presented in Figure 3.10. Regions of high velocity experiences higher pressure drop than other regions of low velocity.

3.4.2.1 Cooling Effect at Plane A–A

In the PU300 experimental unit, the evaporator is a 4-row finned tube heat exchanger. The refrigerant (R-22) flows in the tube circuits. Two-phase heat transfer takes place between airflow passing across the evaporator and the refrigerant flowing inside the tubes. The unit operates in the cooling mode based on the operating conditions applied on the unit. Entering air temperature is 80° F (26.6°C) and refrigerant evaporating temperature is 49°F (9.44°C). Air non-uniformity upstream of the evaporator causes uneven loading of evaporator circuits. This results into poor performance of refrigerant circuits due to uneven flow over them.

Figure 3.11 shows the air temperature distribution at plane A–A downstream of the evaporator. Lower temperature appears in the central region of the plane and higher temperature exists near the plane edges. It is known that evaporator cooling capability increases as air velocity increases. This is due to the increase of airside convective heat transfer coefficient. High and even velocity distribution across evaporator is desired for the same purpose. Note that higher air velocity across evaporator leads to higher air temperature leaving it, as the effect of velocity on the heat transfer is smaller.

The bulk average air temperature (T_b) on plane A-A that takes into account the effect of velocity distribution downstream of the evaporator (u-air speed) can be found as:

$$T_b = \frac{1}{\dot{m}} \int_A \rho \cdot u \cdot T \cdot dA = \frac{1}{\rho \cdot Q} \int_A \rho \cdot u \cdot T \cdot dA = 59.64^{\circ} F \tag{3.4}$$

This value of bulk temperature is equivalent to 15.36°C. Q is the estimated air volume flow rate crossing the evaporator and ρ is the air density. Since the flow is incompressible, then ρ is constant value and is extracted from the integral to cancel with the denominator value. On the other hand, calculating the average air temperature on the same plane without incorporating velocity distribution in the integral gives:

$$\overline{T} = \frac{1}{A}\int_{A} T \cdot dA = 59.39°F \tag{3.5}$$

It is observed that both values of bulk and average temperatures are almost similar, indicating an almost uniform air speed distribution.

Calculating the sensible cooling capacity (q) across the evaporator based on the experimental values as follows:

$$\begin{aligned} q &= \dot{m} \cdot C_p \cdot (T_{in} - T_{out}) \\ q &= \rho \cdot Q \cdot C_p \cdot (T_{in} - T_{out}) \\ q &= 1.16 \times 5.65 \times 1007 \times (26.7 - 15.36) = 74{,}842 \ W \end{aligned} \tag{3.6}$$

Where this value of q is equivalent to 21.3 Tons or 255,438 Btu/hr. The PU300 unit is basically designed to offer 25 tons cooling capacity. The above calculated capacity accounts only for sensible load rather than latent one.

3.4.2.2 Flow Turbulence at Plane A–A

Plane A–A exists in the low-pressure region near the fan section. The fan motor and the rotating shaft cause high fluctuation region in the flow field. This fluctuation is found by means of RMS (root mean square) of each velocity components and denoted as turbulence intensity. This

approach resolves the instantaneous flow velocity u(t) into a time averaged component u and a fluctuating component u'. It can be expressed thus:

$$u(t) = u + u'(t) \tag{3.7}$$

The mean velocity u is determined by:

$$u = \frac{1}{\Delta t} \int_{t_o}^{t_o+\Delta t} u(t) \cdot dt \tag{3.8}$$

The RMS value of the fluctuating component can be estimated as

$$RMS_u = \sqrt{\overline{u'^2}} = \left[\frac{1}{\Delta t} \int_{t_o}^{t_o+\Delta t} [u'(t)]^2 \cdot dt \right]^{1/2} \tag{3.9}$$

Thus the estimated turbulence intensity (TI) based on the u-component is determined in percentage (%) as:

$$TI_u(\%) = \frac{RMS_u}{u} \times 100 \tag{310}$$

Figure 3.12 shows plane A–A indicating measurement points. It also indicates locations of components such as fans, shaft, motor and pulleys on the same plane. Four points are selected for presentation of fluctuating u-air speed as in Figure 3.13. The first point is selected behind the first fan *(point # 8, see Figures 3.12 and 3.13).* High fluctuation is noticed at this point where u-air speed fluctuates between 300–600 ft/min. Point # 20 is located in the region between the two fans. Less fluctuation is measured at this point. Point # 22 is located in the lower plane A–A surface. The last point (point # 38) is behind the rotating shaft and pulley. These points are selected at different locations in plan A–A.

Each single measurement of air speed is logged in a time interval equivalent to two-seconds. The complete measurement of a single point takes place within 180-seconds. It outcomes to 90 readings of recorded velocity. In present results, mean air speed value is considered in the

presentation of air speed distribution in all planes. The estimated turbulence intensity based on the actual measurements does not essentially provide accurate information about turbulence. It only offers an insight into the flow field and regions of flow non-uniformity.

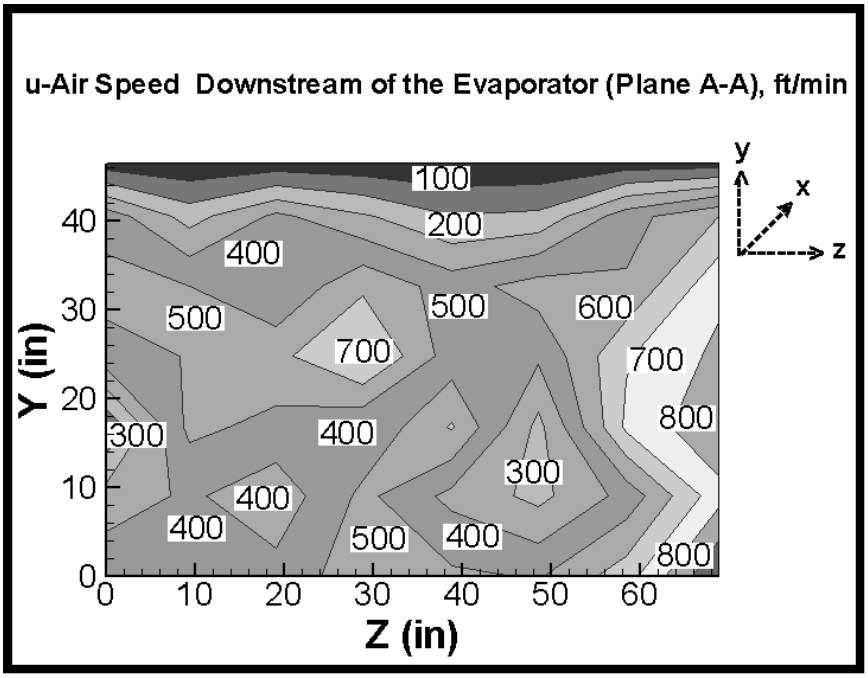

Figure 3.6. u-air speed measured downstream of the evaporator (plane A–A)

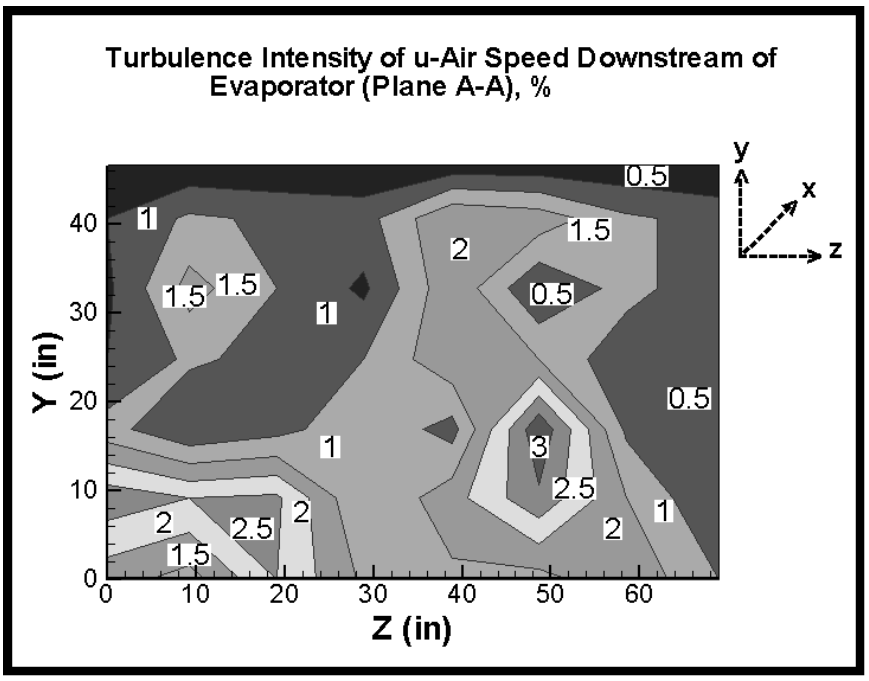

Figure 3.7. Estimated turbulence intensity of u-air speed downstream of the evaporator (plane A–A).

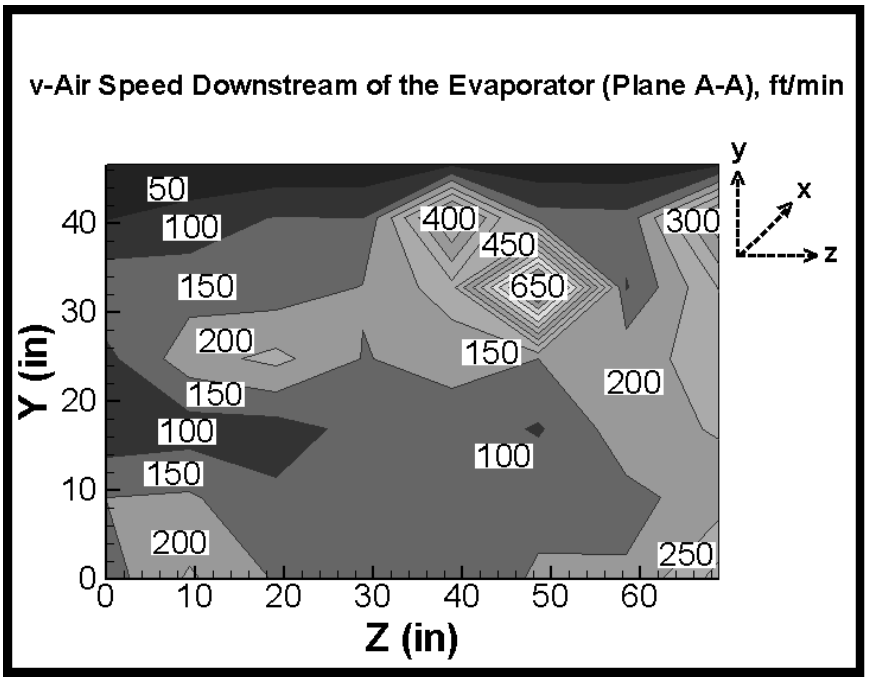

Figure 3.8. v-air speed measured downstream of the evaporator (plane A-A).

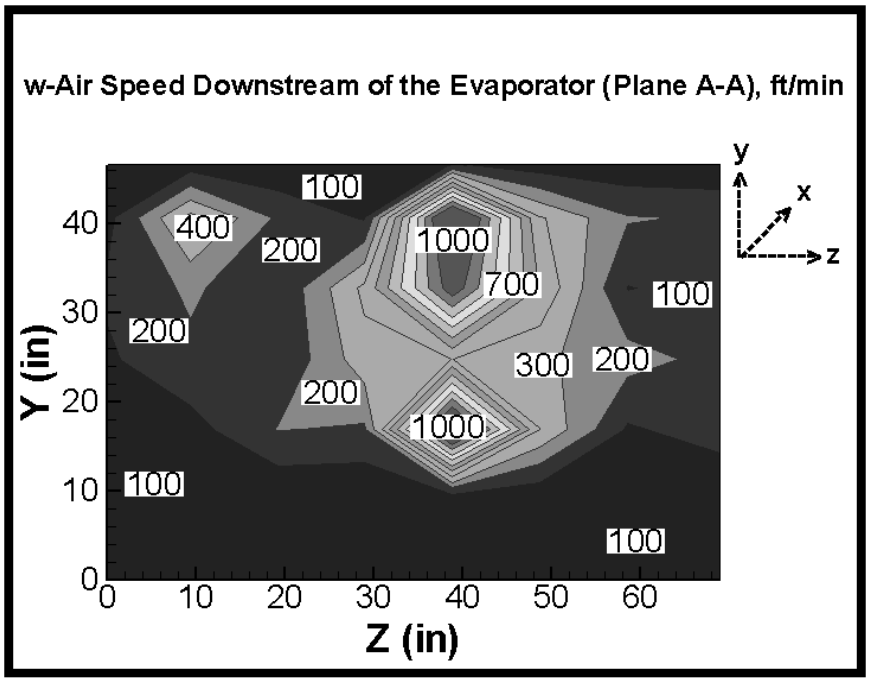

Figure 3.9. w-air speed measured downstream of the evaporator (plane A-A)

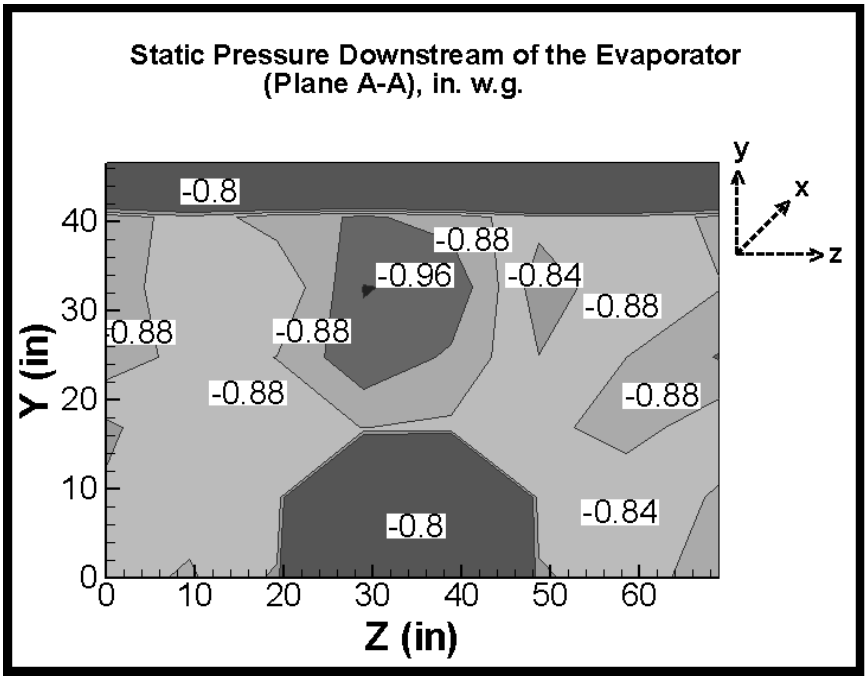

Figure 3.10. Static pressure measured downstream of the evaporator (plane A-A).

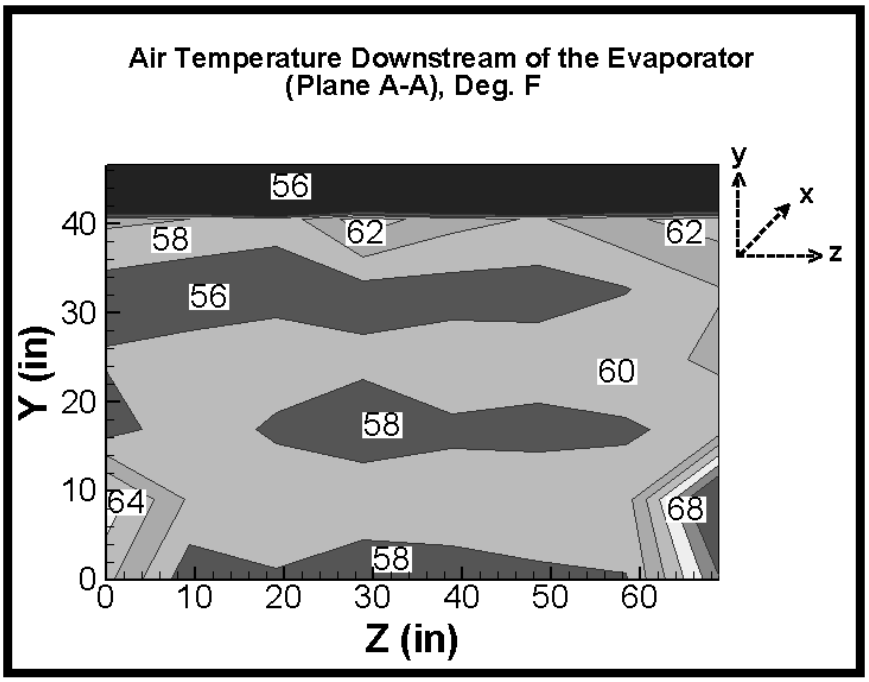

Figure 3.11. Air temperature measured downstream of the evaporator (plane A-A).

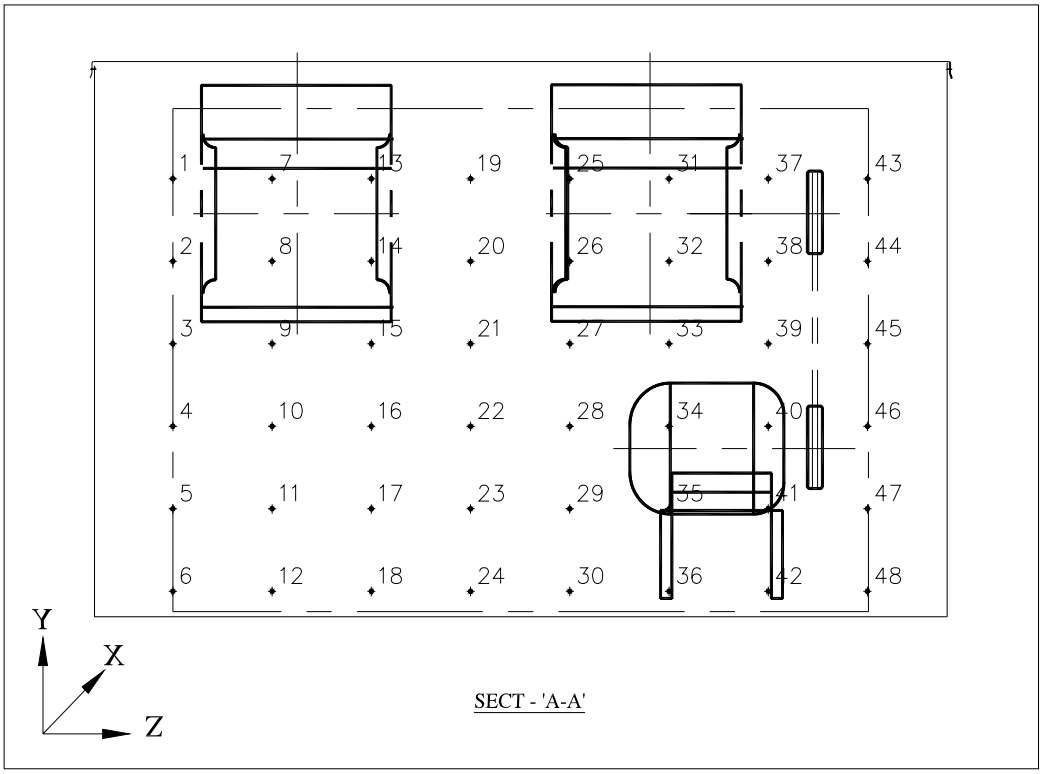

Figure 3.12. Plane A–A, with measurement points numbering and components behind the plane.

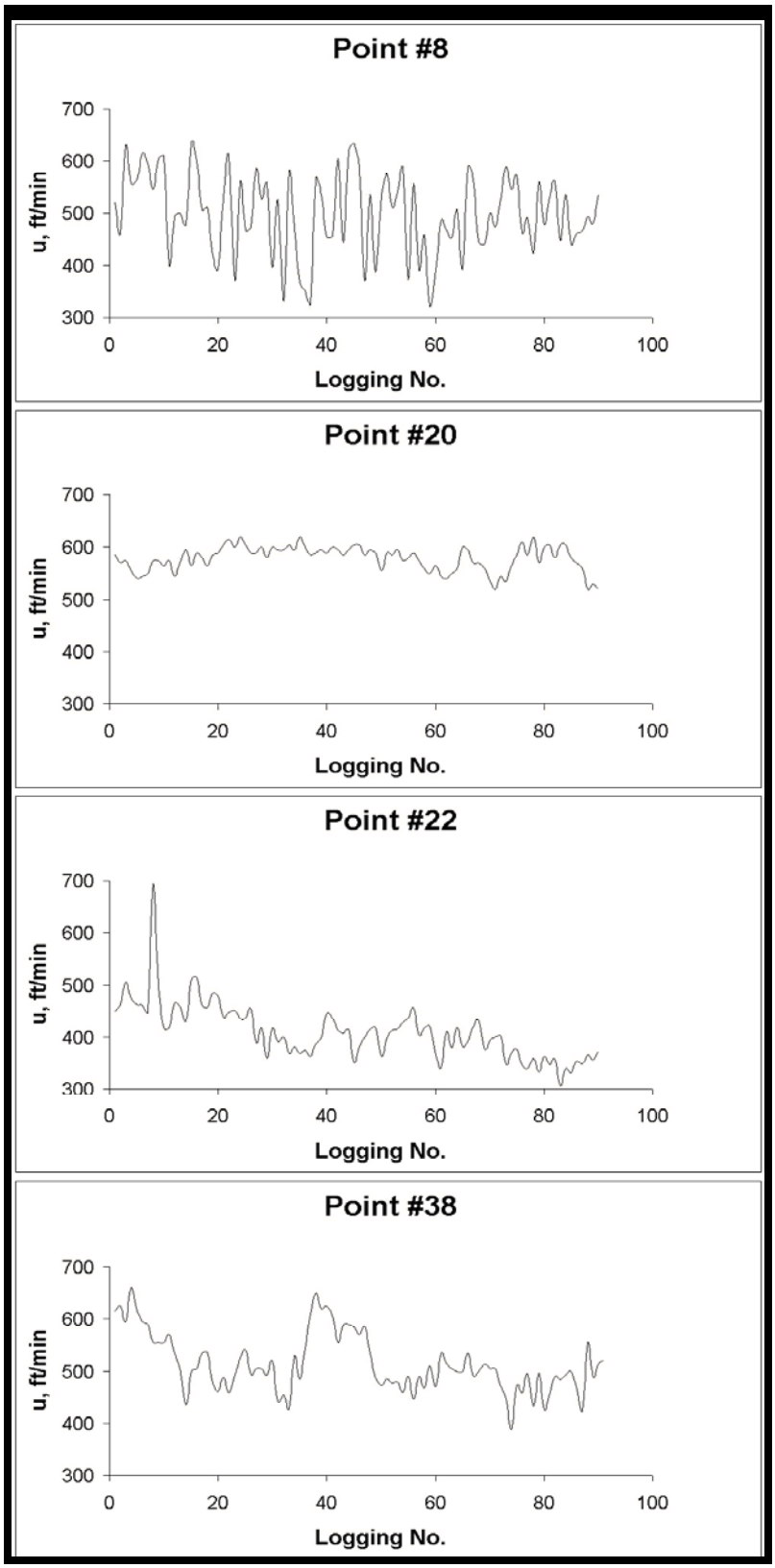

Figure 3.13. Fluctuation of u-air speed at measurement points on plane A-A.

3.5 FAN

3.5.1 FAN INLET (PLANES C–C, D–D AND E–E)

The shaft is connected to the fan motor through the pulley. It drives impellers of the two centrifugal fans of PU300 unit. Rotating components such as impellers, shaft, fan pulley and motor pulley contribute in disturbing the flow and add more swirls to it.

Figures 3.14 and 3.16 exhibit contours of u and w-air speed components respectively on plane C–C at fan # 1 inlet face. The measurements are taken on plane at a distance of 1 in. from the fan inlet face. Peak u-air speed is noticed in the regions near the corners of the fan inlet plane as in Figure 3.14. It reaches about 4500 ft/min at lower right corner. Air flows to the fan inlet from all directions towards the low-pressure region. All components of air speed are measured at this plane. The w-air speed component normal to the fan inlet displays the highest values as shown in Figure 3.16. The maximum w-air speed exceeds 3500 ft/min at the center of the plane.

Negative pressure is observed at plane C–C (see Figure 3.17). It reaches around (–1.5) in. of water gauge (-375 Pa). Similar static pressure level is measured at other fan inlets as in Figures 3.20 and 3.23. They show static pressure contour at plane D–D and plane E–E respectively. This similarity indicates almost equivalent performance of each fan inlet.

The shaft driving the two fans is mounted on two bearings. These bearings are fixed to a support sheet on the fan-housing surface. The support sheets create partial blockage of the fan inlet area. This leads to a difficulty in measurement of some locations. In addition, the rotating shaft is located at the center of the fan inlet. This position cannot be measured by the velocity probe. Plane D–D at the other inlet face of fan # 1 shows limited number of measurement points due to the above-mentioned difficulties.

Figures 3.18 and 3.19 display contour maps of u and w-air speed at plane D–D respectively. The unmeasured locations are excluded from the contour map by blanking them. It is observed that u-air speed component in the x-direction parallel to the fan inlet reaches 1500 ft/min in some locations. This shows the complexity of the flow occurring at the fan inlet. It is found that w-air speed dominates the flow as it exceeds 3000–4000 ft/min range.

In plane E–E at fan # 2 inlet face, Figures 3.21 and 3.22 show u and w-air speed components at this plane. Similar contour levels could be observed here in comparison to the other fan inlets. This determines that the flow characteristics measured on all planes of the fan inlets are in the same range of velocity and static pressure. It may also be deduced that fan positions are correctly situated in the unit as it results the similar flow characteristics.

3.5.1.1 Flow Turbulence at Fan Inlet

With reference to measurement points taken on plane C–C (see Figure 2.10). Both u and w-air speed fluctuation on three measurement points (point # 2, 4 and 5) are presented in Figures 3.24 and 3.25 respectively. Both air speed components exhibit high fluctuation at these points. At point # 4, u-air speed fluctuates in the range of 2000-3500 ft/min.

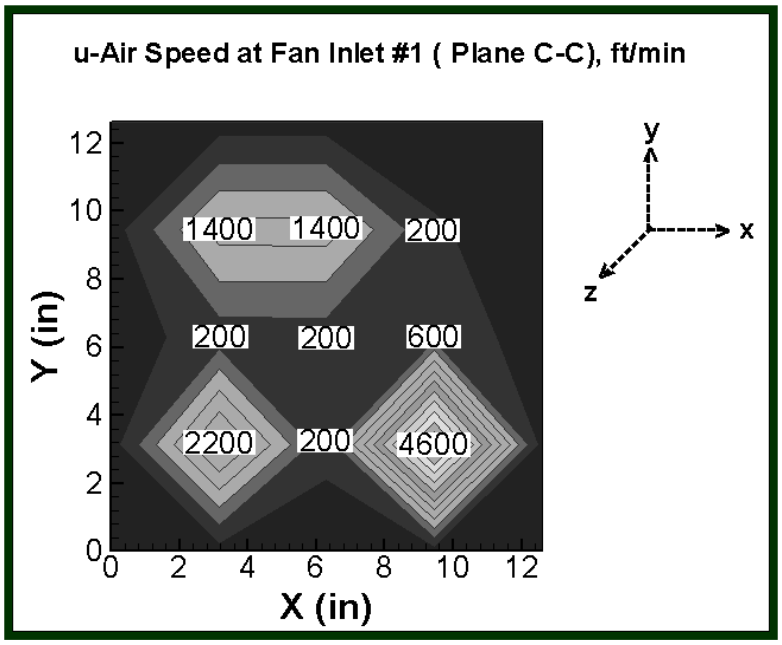

Figure 3.14. u-air speed measured at fan inlet #1 (plane C–C)

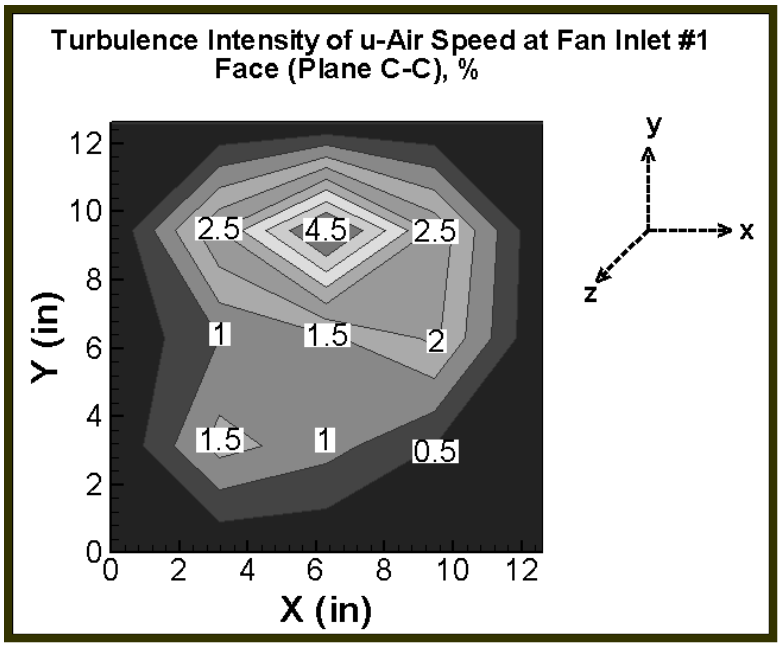

Figure 3.15. Estimated turbulence intensity of u-air speed at fan inlet #1 (plane C–C).

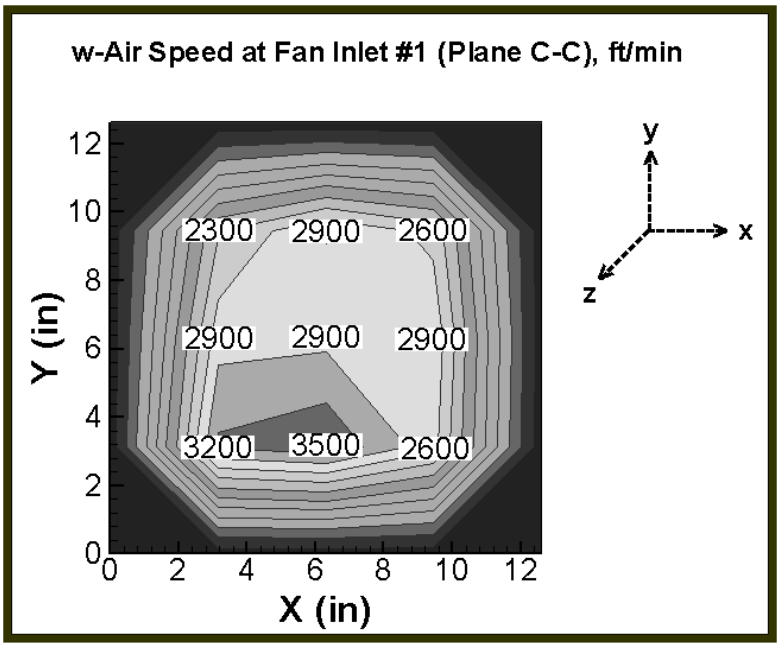

Figure 3.16. w-air speed measured at fan inlet #1 (plane C–C).

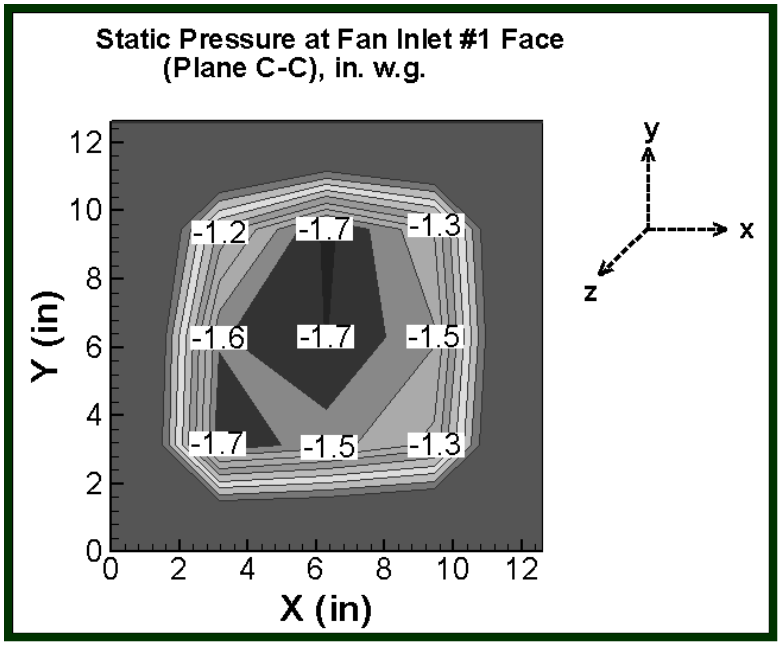

Figure 3.17. Static pressure measured at fan inlet # 1 (plane C–C).

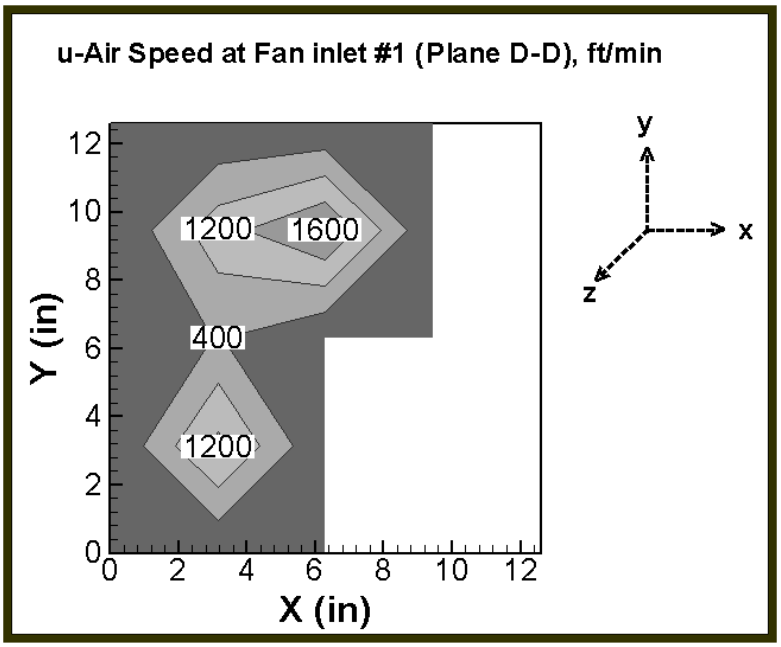

Figure 3.18. u-air speed measured at fan inlet #1 (plane D–D).

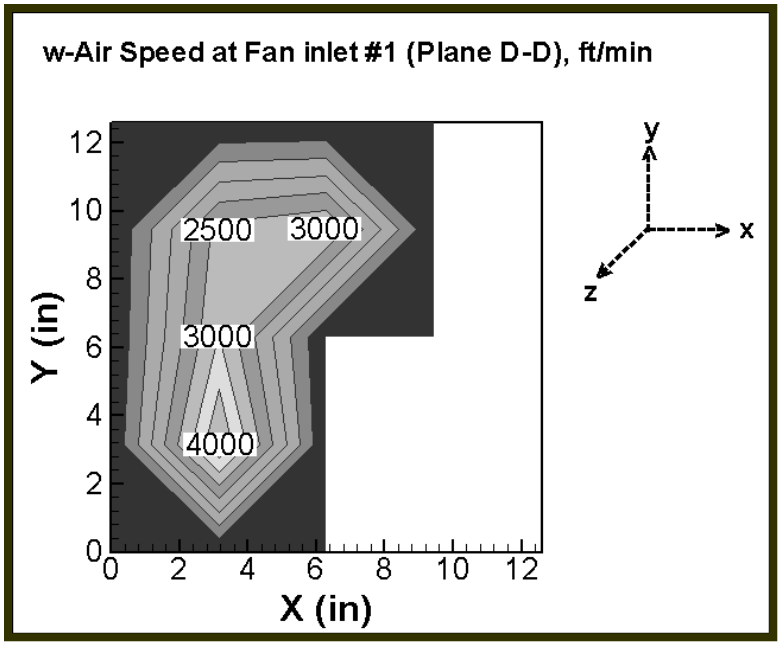

Figure 3.19 : w-air speed measured at fan inlet # 1 (plane D-D).

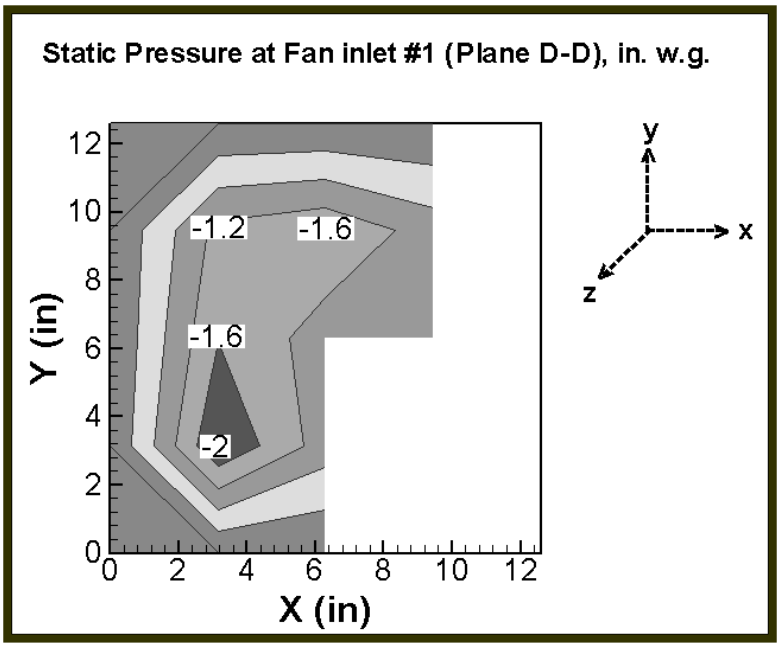

Figure 3.20. Static pressure measured at fan inlet # 1 (plane D–D).

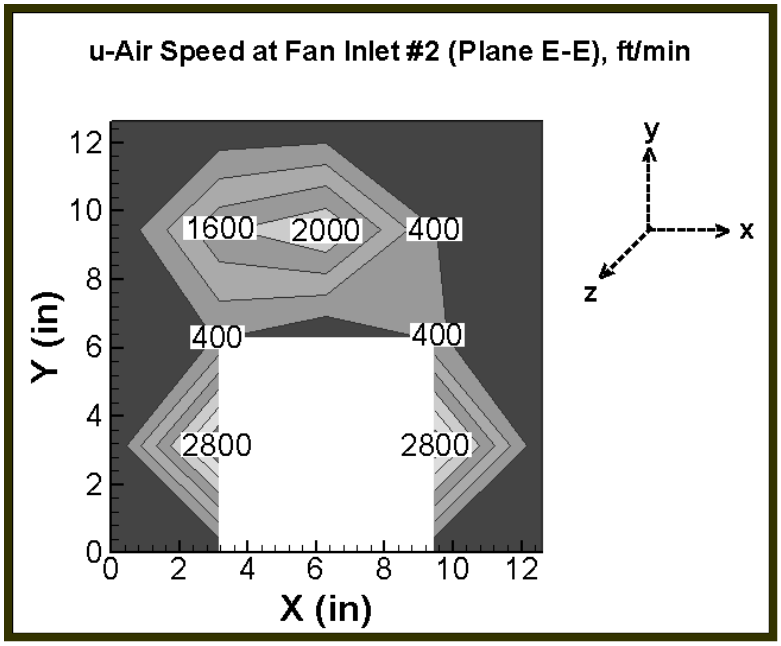

Figure 3.21. u-air speed measured at fan inlet #2 (plane E–E).

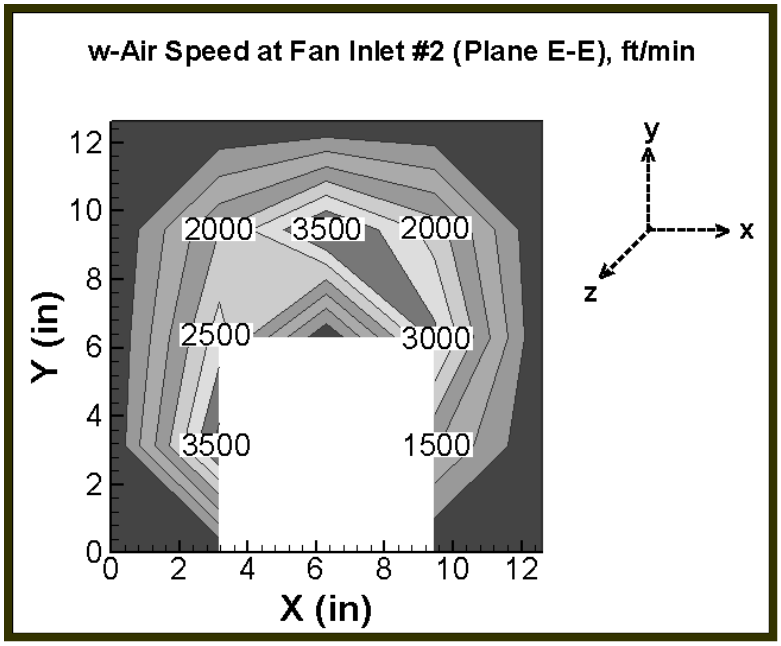

Figure 3.22. w-air speed measured at fan inlet # 2 (plane E–E).

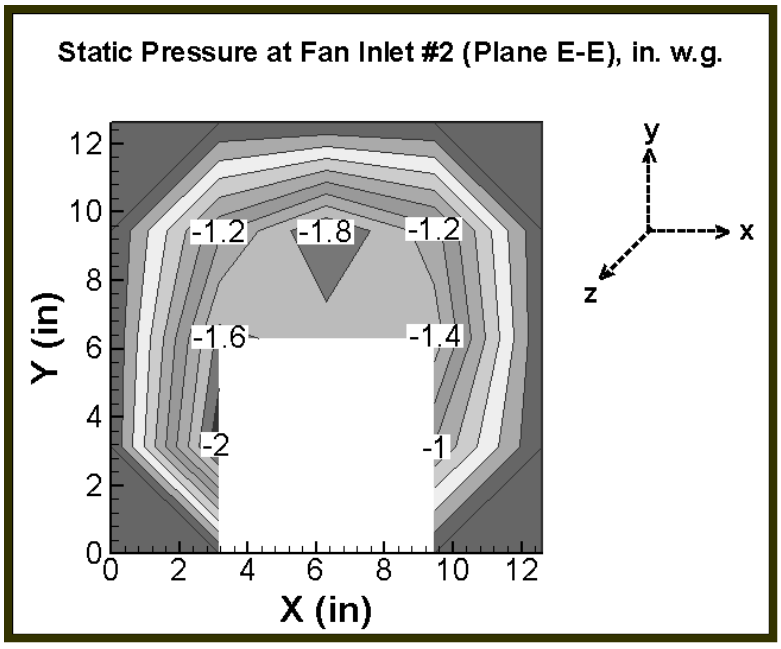

Figure 3.23. Static pressure measured at fan inlet #2 (plane E–E).

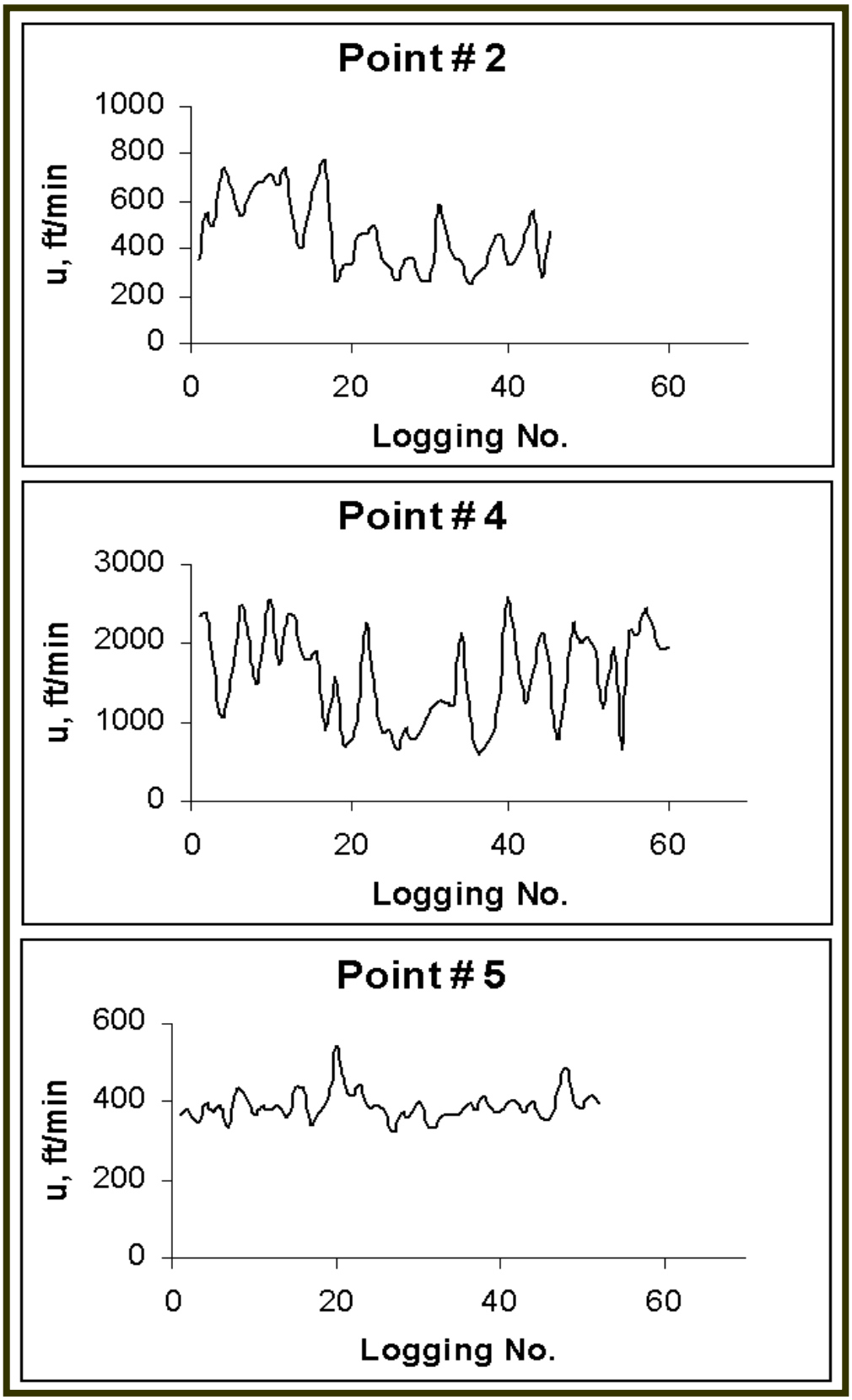

Figure 3.24. Fluctuation of u-air speed at measurement points on plane C-C.

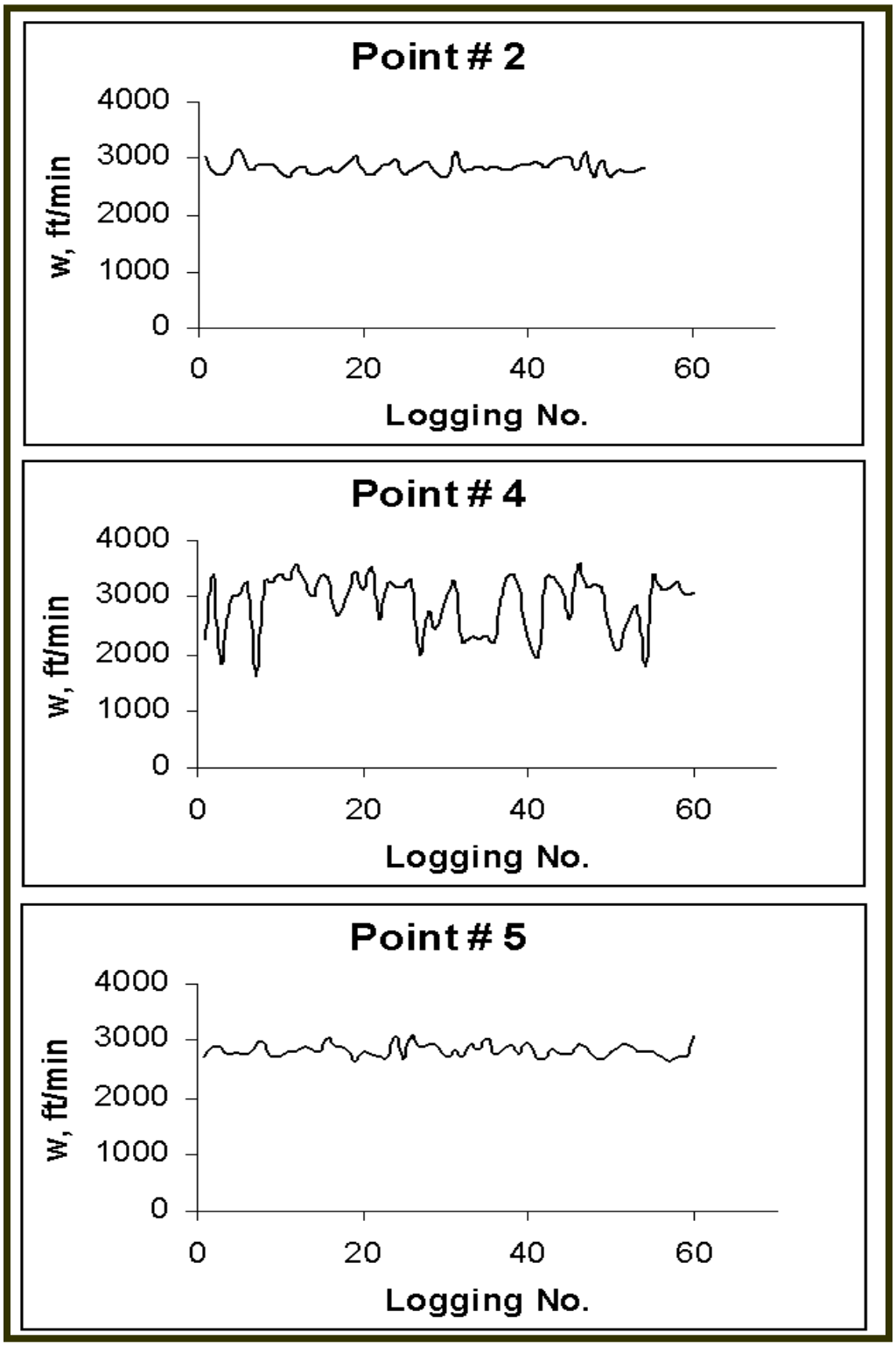

Figure 3.25. Fluctuation of w-air speed at measurement points on plane C-C.

3.5.2 FAN OUTLET PLANES

In the experimental setup of the PU300 unit, the two fans are tilted 25° clockwise about the z-axis. The velocity component normal to the fan outlet faces is expected to be the dominant one. Figures 3.26 and 3.28 show contours of air speed component normal to fan outlet # 1 and 2 respectively on plane F–F. Air speed distribution on the first fan outlet differs from that of the second fan. Higher air speed is reported in the second fan where the air speed range is between 2,000–6,000 ft/min. The range of air speed at the first fan outlet is between 1,000 to 4,500 ft/min. Both fans are driven by one motor at the same rpm (1,000 rpm). The difference in air speed levels between the two fans shows that each one supplies different flow rates resulted from different flow resistances around them.

On both fan outlet faces the static pressure ranges between 0-1 in. w.g. (see Figures 3.27 and 3.28 for static pressure at fan # 1 and 2 outlet faces respectively).

It is desired to calculate the actual pressure jump across each fan. This is accomplished by calculating the weighted average static pressure $\overline{P}_{avg,s}$ on both the fan inlet and outlet faces by integrating these values over each face area as:

$$\overline{P_{avg,s}} = \frac{1}{A}\int P \cdot dA \tag{3.11}$$

The averaged values of static pressure over the respected face areas are presented in Table 3.2. From these values, the pressure jump (ΔP) across each fan is calculated as:

$$\Delta P = P_{avg,o} - P_{avg,i} \tag{3.12}$$

where the average static pressure values are calculated at both the fan inlet and the fan outlet faces.

Table 3.2: Static pressure and pressure jump performed by the two fans.

	P (static pressure, in. w.g.)		ΔP
	Inlet face	Outlet face	Pressure jump, in. w.g.
Fan # 1	-1.34	0.43	1.77
Fan # 2	-1.49	0.45	1.94

Table 3.2 indicates that Fan # 1 has slightly lower pressure jump than Fan # 2. This difference is due to the different flow resistance for each fan. It is also observed that fan #1 delivers airflow rate of 3.14 m^3/s (6,647 ft^3/min). This is slightly less than Fan # 2 which delivers 3.57 m^3/s (7,557 ft^3/min) due to the difference of pressure jump.

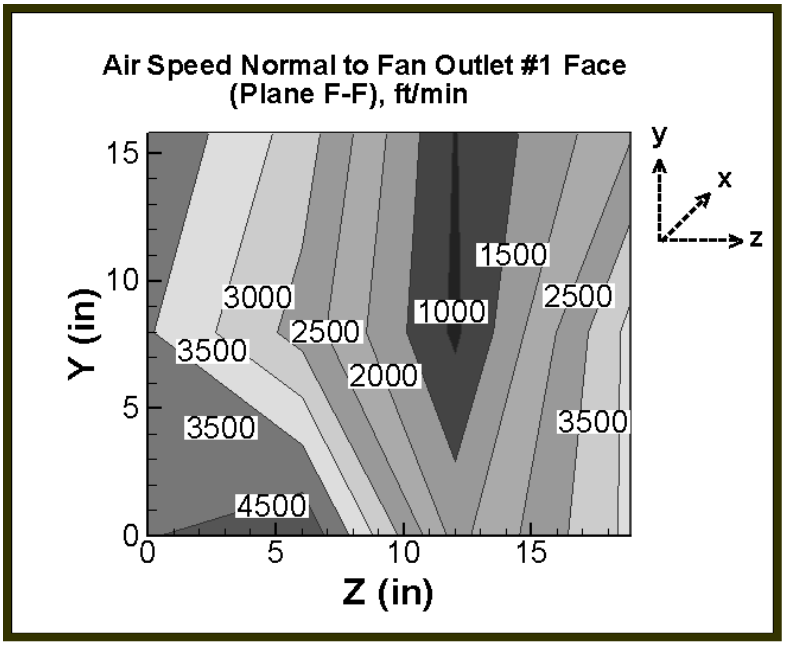

Figure 3.26. Air speed measured normal to Fan Outlet # 1 face (plane F-F).

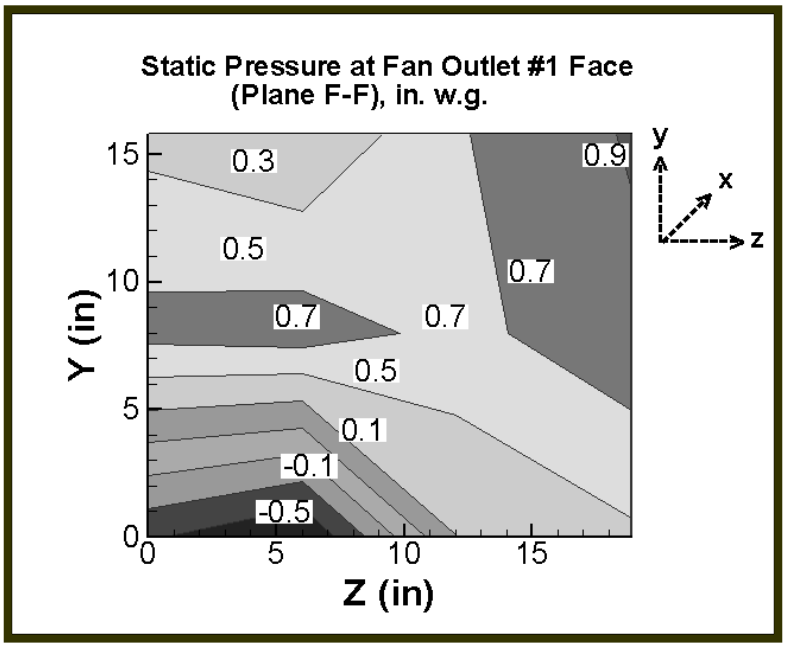

Figure 3.27. Static pressure measured at Fan Outlet # 1 face (plane F-F)

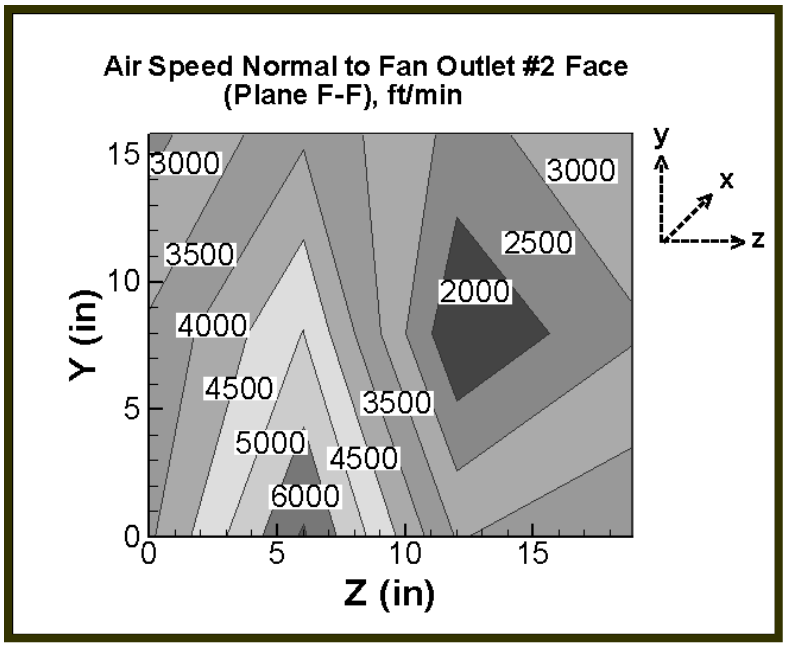

Figure 3.28. Air speed measured normal to Fan Outlet # 2 face (plane F-F).

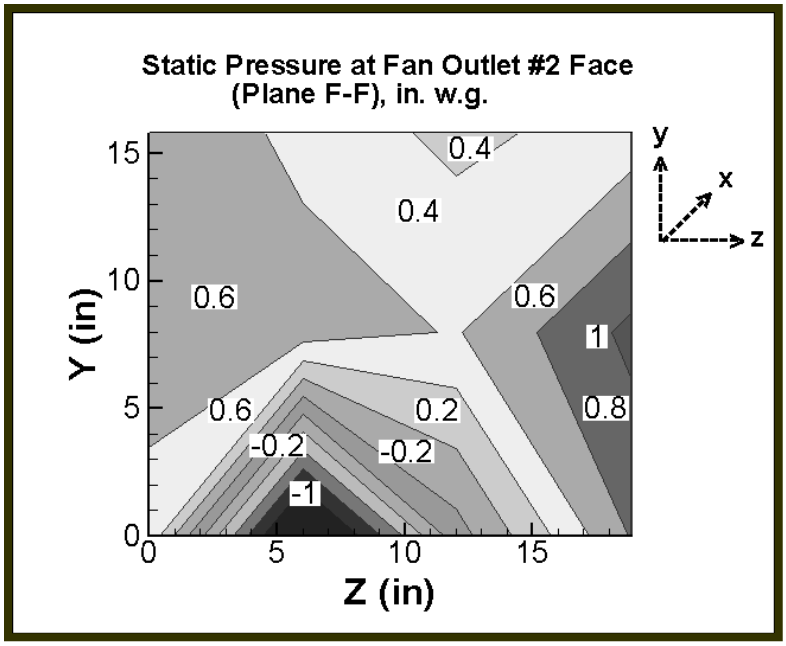

Figure 3.29. Static pressure measured at Fan Outlet # 2 face (plane F–F).

3.6 OUTLET

The unit outlet face is connected to a ducting system, which delivers air to the reconditioning system in the psychometric testing room. Figures 3.30 to 3.32 display contours of u-air speed, w-air speed and static pressure respectively on the outlet face. High w-air speed in the opposite z-direction axis is indicated especially in the lower area where it reaches 3100 ft/min.

The PU300 unit configuration forces air to turn 90° from fan outlet towards the unit outlet results into complex flow. Placing the unit outlet face in the same direction as the fan outlet may reduce the flow complexity and losses in this section. This correction in the design will be considered in the next chapter of parametric study. However, this present configuration considers other factors rather than flow regime such as the case of accessibility. Having one-side duct connection for both the inlet and the outlet face is desired in practical situations. Figure 3.32, shows the con-

tours of static pressure at the unit outlet. The integrated average static pressure over the outlet face area is 0.15 in. w.g.. This positive value is needed to push the supply airflow rate and overcome the external static pressure losses.

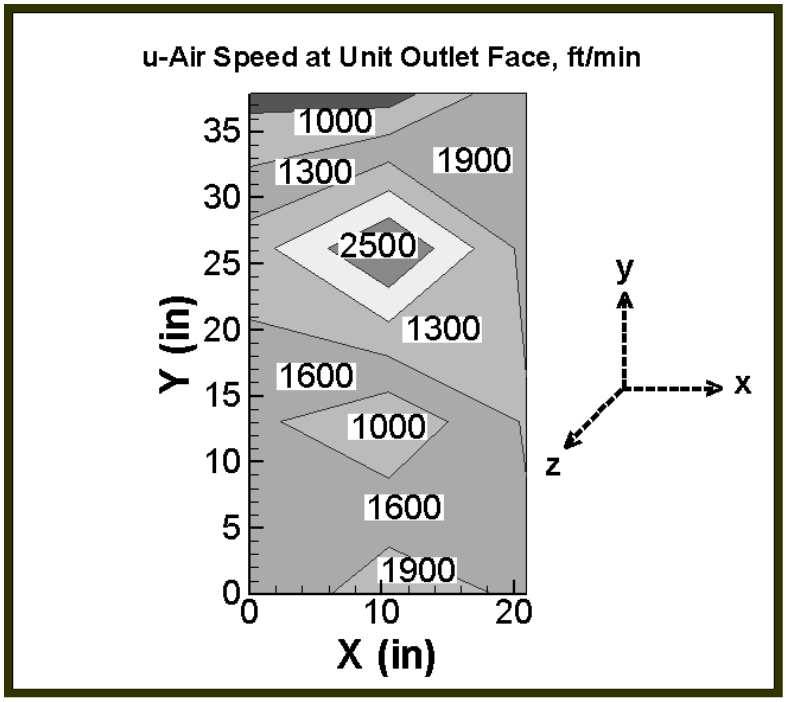

Figure 3.30. u-air speed measured at unit outlet face

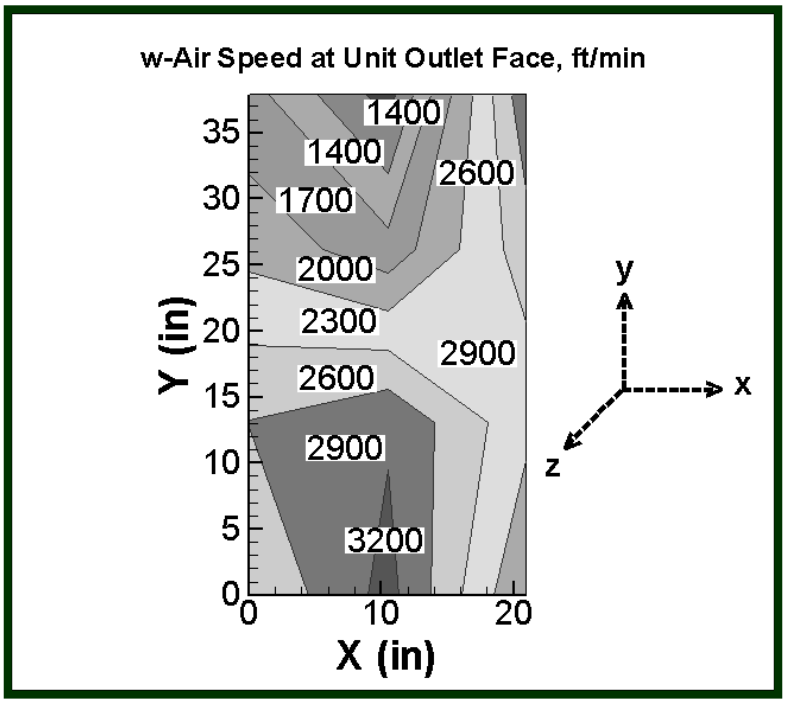

Figure 3.31. w-air speed measured at unit outlet face.

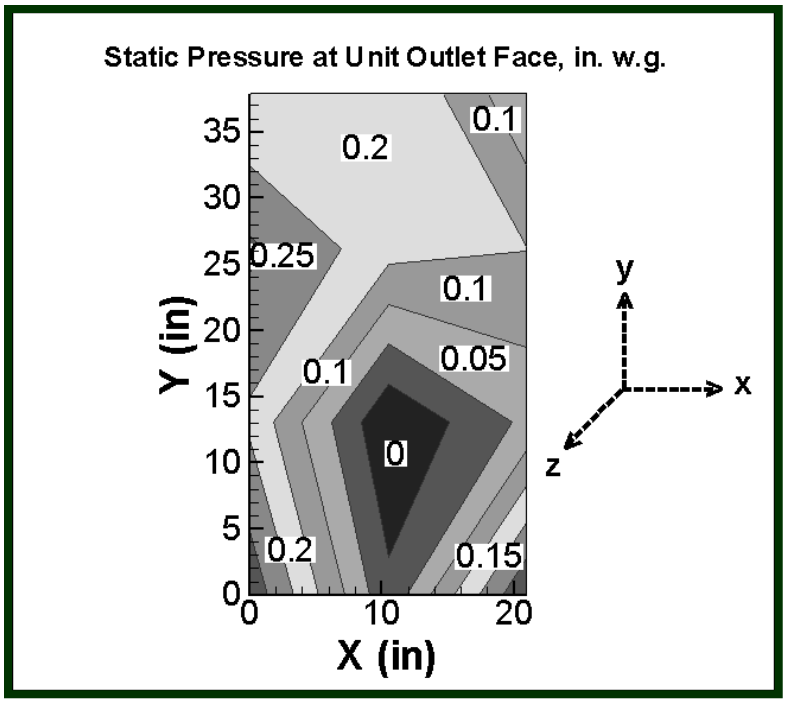

Figure 3.32. Static pressure measured at unit outlet face.

CHAPTER 4

CFD MODELING OF A PACKAGED AIR CONDITIONING UNIT

4.1 GENERAL

The flow pattern in a packaged air conditioning unit needs a turbulent three-dimensional modeling. The governing flow equations are solved by setting-up the geometry of the unit using CAD preprocessor software. The CFD software is used for solving the fluid flow problems with unstructured mesh in order to handle the complex geometry of the A/C unit.

4.2 BASIC GEOMETRY

The three–dimensional geometry of the packaged unit (PU300) is created in Gambit (CAD preprocessor software). The main components of the unit considered include: the evaporator, the fan, the drain pan, the motor stand, the motor, the bearings, the pulleys, and the shaft (see Fig 4 .1). The geometry construction is focused on the components that directly affect flow field. However, some minor details in the assembly are ignored to limit the number of cells required for meshing the geometry.

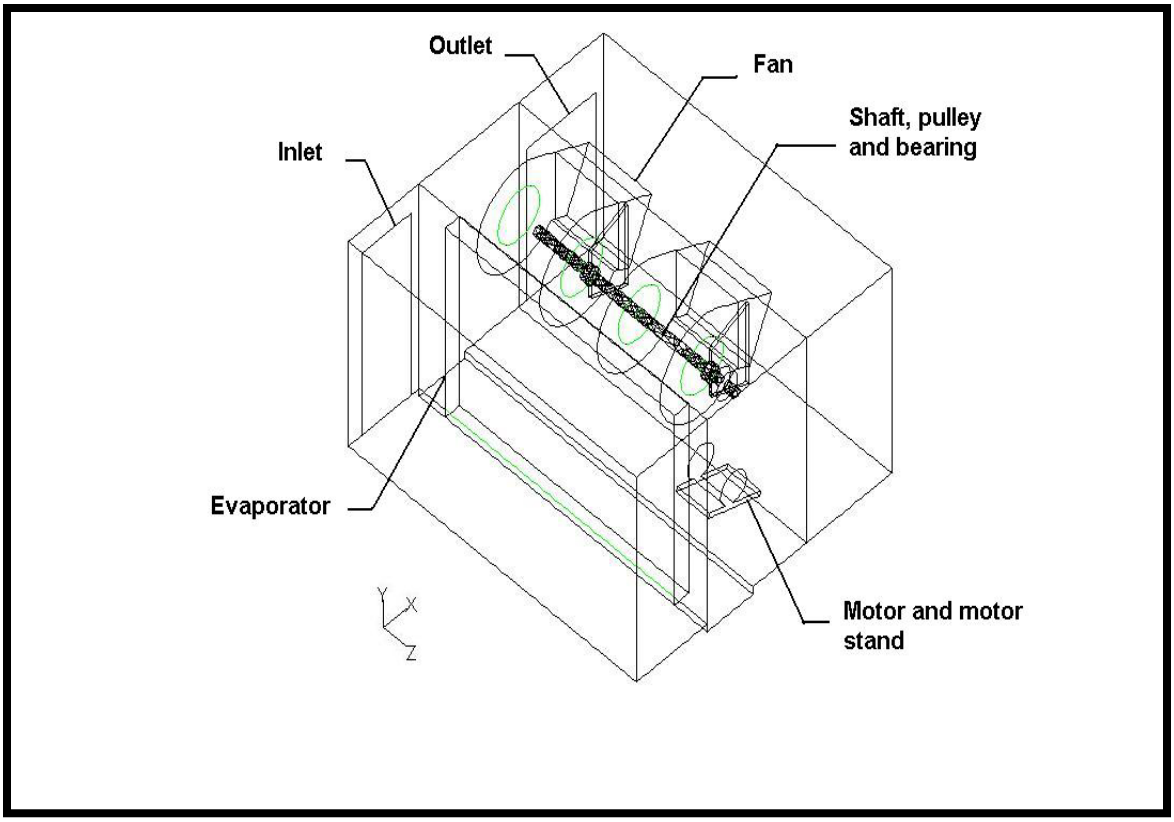

Figure 4.1. Basic geometry of the PU300 unit.

A suitable volume meshing is generated for the three-dimensional geometry of the packaged unit. Tetrahedral elements are used in this case. Due to memory limitation, the smaller cell size is taken to be 3.6 cm (1.57 in.). This mesh size results into 800,000 cells. The relatively large number of cells is needed to cover narrow spaces in the geometry.

4.3 MATHEMATICAL FOMULATION

The airflow inside the modeled packaged unit is solved subject to the following considerations:

a. Physical domain is three-dimensional.

b. The flow is steady.

c. Incompressible flow (low Mach number for air, less than 0.2)

d. Heat transfer is considered in evaluating the performance of evaporator in the specified packaged unit.

e. Humidity and Buoyancy effects on air are neglected.

f. Flow is turbulent, the Reynolds-averaged Navier-Stokes equations are used as a governing equations as listed next:

$$\frac{\partial U_j}{\partial X_j} = 0 \tag{4.1}$$

$$\rho U_j \frac{\partial U_i}{\partial X_j} = -\frac{\partial P}{\partial X_i} + \frac{\partial}{\partial X_j}\left[\mu\left(\frac{\partial U_i}{\partial X_j} + \frac{\partial U_j}{\partial X_i}\right)\right] - \frac{\partial}{\partial X_j}\rho\overline{u_i u_j} + B_i \tag{4.2}$$

where, B_i: body force per unit mass and, $\overline{u_i u_j}$: Reynolds stress

Using the k-ε turbulence model, the Reynolds stress and turbulent viscosity are expressed as:

$$-\rho\overline{u_i u_j} = \mu_t\left(\frac{\partial U_i}{\partial X_j} + \frac{\partial U_j}{\partial X_i}\right) - \frac{2}{3}\delta_{ij}\rho k \tag{4.3}$$

$$\mu_t = \frac{C_\mu \rho k^2}{\varepsilon} \tag{4.4}$$

where, μ_t is the turbulent or eddy viscosity, k is the turbulent kinetic energy, and ε is the dissipation rate. They are computed through their transport diffusion equations:

$$\rho U_j \frac{\partial k}{\partial X_j} = \frac{\partial}{\partial X_j}\left(\frac{\mu_t}{\sigma_k}\frac{\partial k}{\partial X_j}\right) + P_k - \rho\varepsilon \tag{4.5}$$

$$\rho U_j \frac{\partial \varepsilon}{\partial X_j} = \frac{\partial}{\partial X_j}\left(\frac{\mu_t}{\sigma_\varepsilon}\frac{\partial \varepsilon}{\partial X_j}\right) + C_{\varepsilon 1}\frac{P_k \varepsilon}{k} - C_{\varepsilon 2}\frac{\rho\varepsilon^2}{k} \tag{4.6}$$

Where, P_k is the production of turbulent kinetic energy:

$$P_k = \mu_t\left(\frac{\partial U_i}{\partial X_j} + \frac{\partial U_j}{\partial X_i}\right)\frac{\partial U_i}{\partial X_j} \tag{4.7}$$

The boundary conditions used for the flow and temperature solutions are as follows:

a. Inlet: Pressure boundary is applied based on the assumption of atmospheric pressure at the inlet of the unit. The dry bulb temperature of air entering the unit is set at 80° F (26.7°C).

b. Outlet: A pressure boundary is applied at the outlet. Static (gauge) pressure relative to system operating pressure is specified. Taking into account the static pressure losses across casing and evaporator coil.

c. Walls: A no slip condition is applied in this case, by assuming the velocity at the wall to be zero.

d. Heat exchanger model: The heat exchanger model is formulated as a distributed flow resistance by introducing a porous media, which is implemented by the addition of momentum source/sink term to the standard fluid flow equations. The source term is composed of two parts, a viscous loss term (Darcy), and an inertial loss term:

$$S_i = \sum_{j=1}^{3} D_{ij}\mu V_j + \sum_{j=1}^{3} C_{ij}\frac{1}{2}\rho\left|V_j\right| V_j \tag{4.8}$$

where, S_i is the source term for the x, y and z momentum equations, V_j is the average velocity component, and D_{ij} with C_{ij} are prescribed matrices. This momentum sink contributes to the

pressure gradient in the porous cell, creating a pressure drop that is proportional to the fluid velocity in the cell.

Energy treatment in porous media is performed by solving the standard energy equation. Modification to the conduction flux and the transient terms is included as explained in the heat exchanger model.

In the present CFD package, the radiator model is selected to represent the distributed resistance of evaporator coil by entering following two inputs:

(i) Loss coefficient (K_L), which accounts for static pressure drop losses at different air velocity across the evaporator coil:

$$\Delta P = K_L(\frac{1}{2}\rho V^2) \tag{4.9}$$

The loss coefficient is calculated based on experimental data of pressure drop at different velocities. A polynomial function of K_L is fitted based on this data as shown in Figure 4.2.

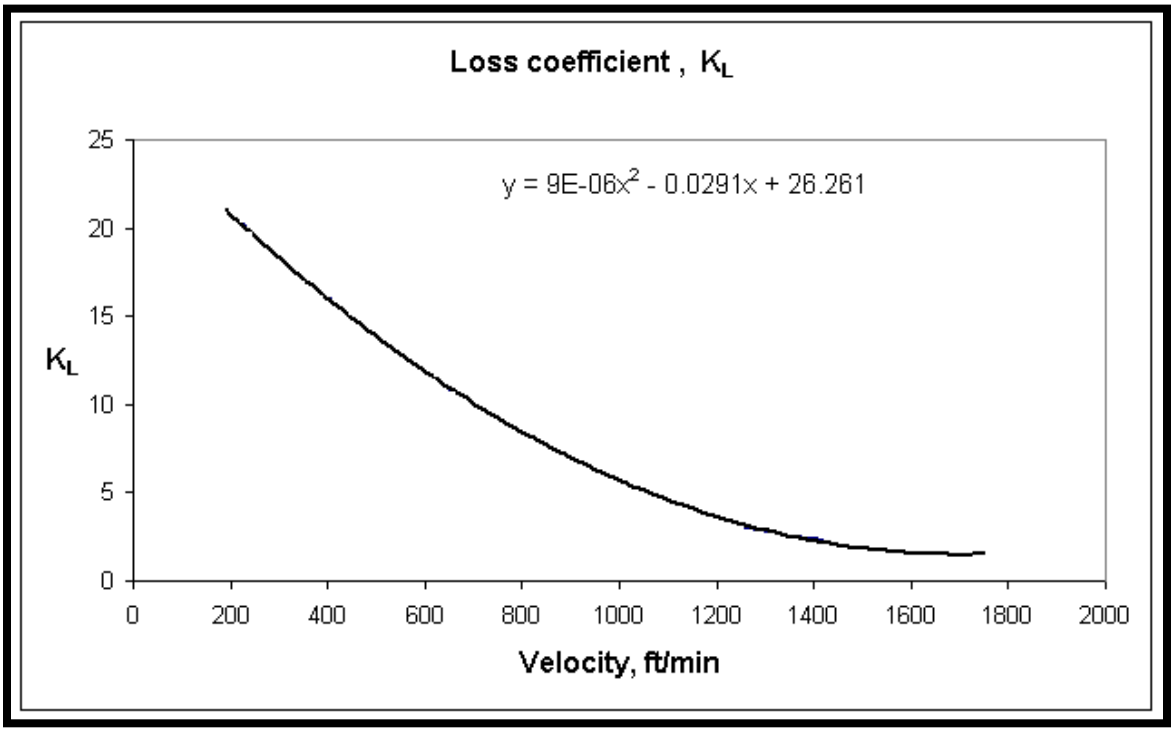

Figure 4.2. Polynomial function created for loss coefficient (K_L).

(ii) Heat transfer coefficient (h) as a function of air velocity across evaporator as follows:

$$q'' = h(T_{HX} - T_{exit}) \tag{4.10}$$

where, q" is the heat flux, and the T_{HX} and T_{exit} are heat exchanger surface temperature and exit air temperature. In this model, either the heat flux q" and heat transfer coefficient h or the surface temperature of heat exchanger T_{HX} and h shall be given. The heat exchanger surface temperature is set constant at 49° F (9.44° C). The manufacturer of heat exchanger provides capacity curves based on experimental measurements at variable air velocity across corresponding heat exchangers.

e. Fan model: The model for the centrifugal fan is formulated in terms of pressure jump correlation based on manufacturer data given at different volume flow rates. The fan performance curve is fitted in polynomial form. This method was used by Yukio Matsushima et al., [7]. The fan outlet face is selected to represent the fan model. Figure 4.3 shows polynomial function that approximates pressure jump curve as a function of airflow velocity.

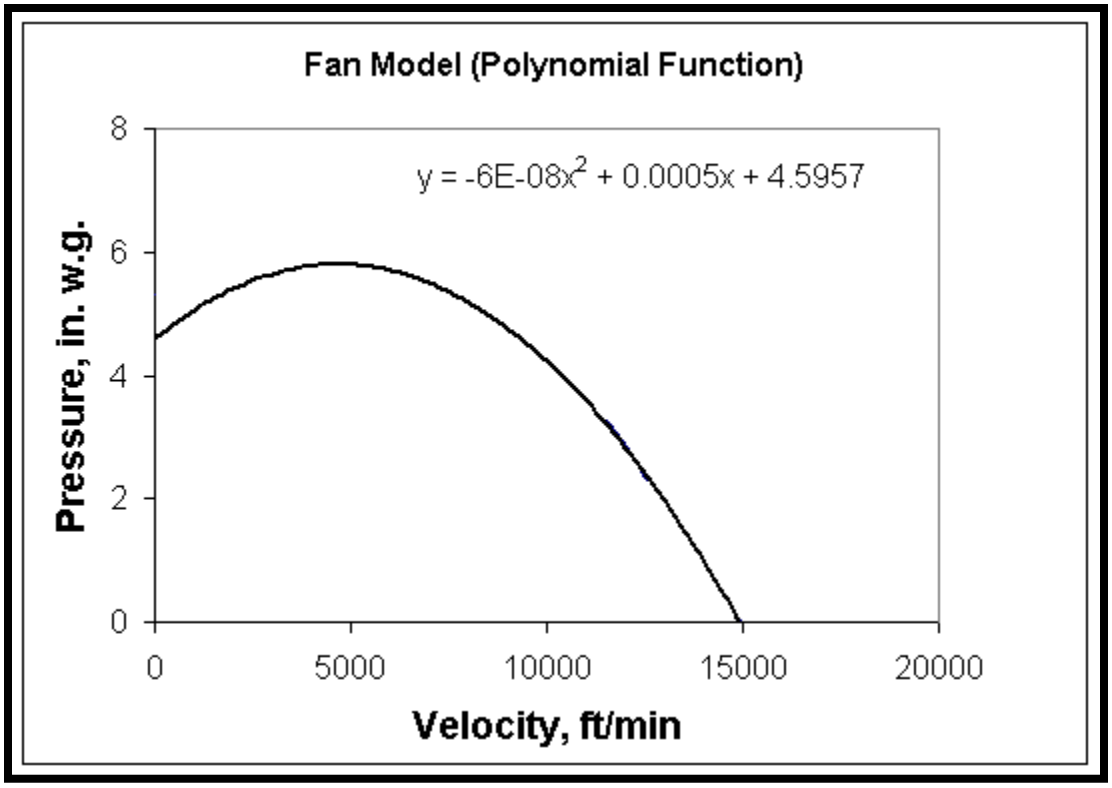

Figure 4.3. Pressure jump polynomial of fan model.

4.4 MESH QUALITY

The shape of the cells inside the mesh (including its skewness and aspect ratio) has a significant impact on the accuracy of the numerical solution. Skewness represents the difference between the cell's shape and the shape of an equilateral cell of equivalent volume. The mesh quality of the numerical model is analyzed by means of both equiangular and equivolume skew of each cell in the geometry. The first refers to the normalized angle deviation method, while the second refers the volume deviation method.

Figures 4.4 and 4.5 present both equiangular and equivolume skew for the tetrahedral mesh of the PU300 meshed geometry. The histograms show percentage of the skewness in the total mesh. It is noticed that maximum equiangular skew reached 0.7. The majority of cells fall in 0.2–0.5 range. The large number of cells used in this mesh (800,000) should be a good compromise based on the given computational resources. It is concluded that this mesh is of good quality and would not affect the accuracy and stabilization of the numerical solution.

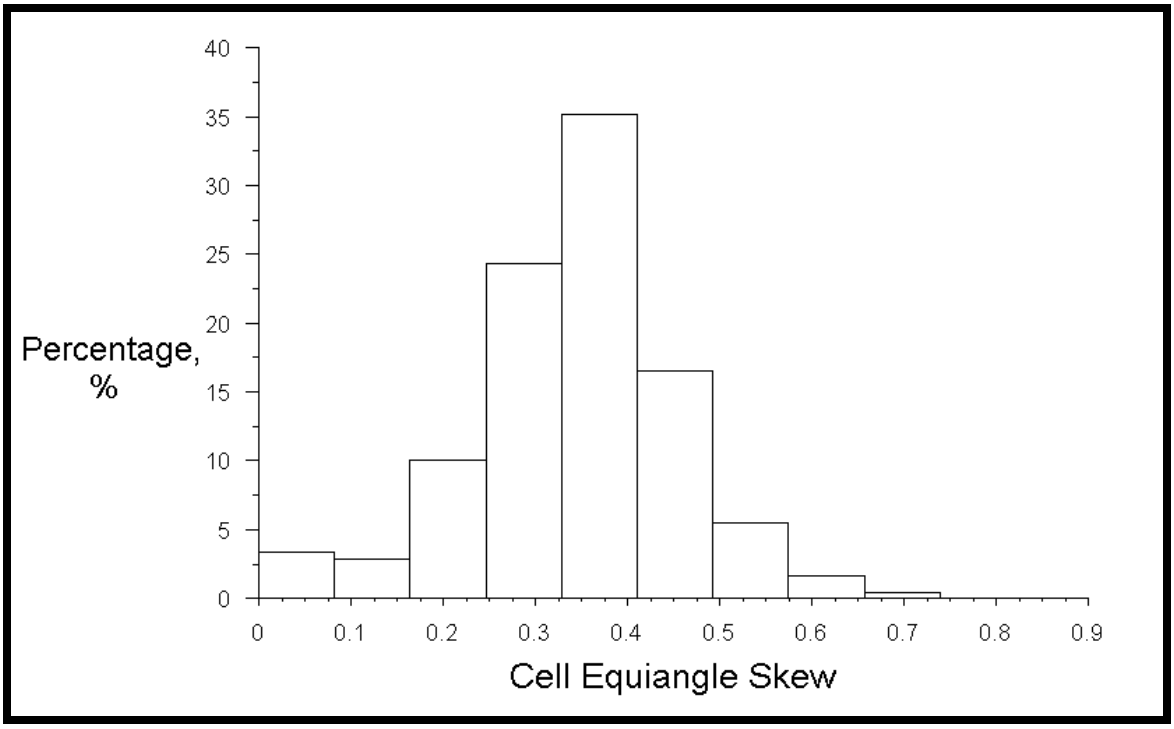

Figure 4.4. Equiangular skew of the volume mesh of PU300 model.

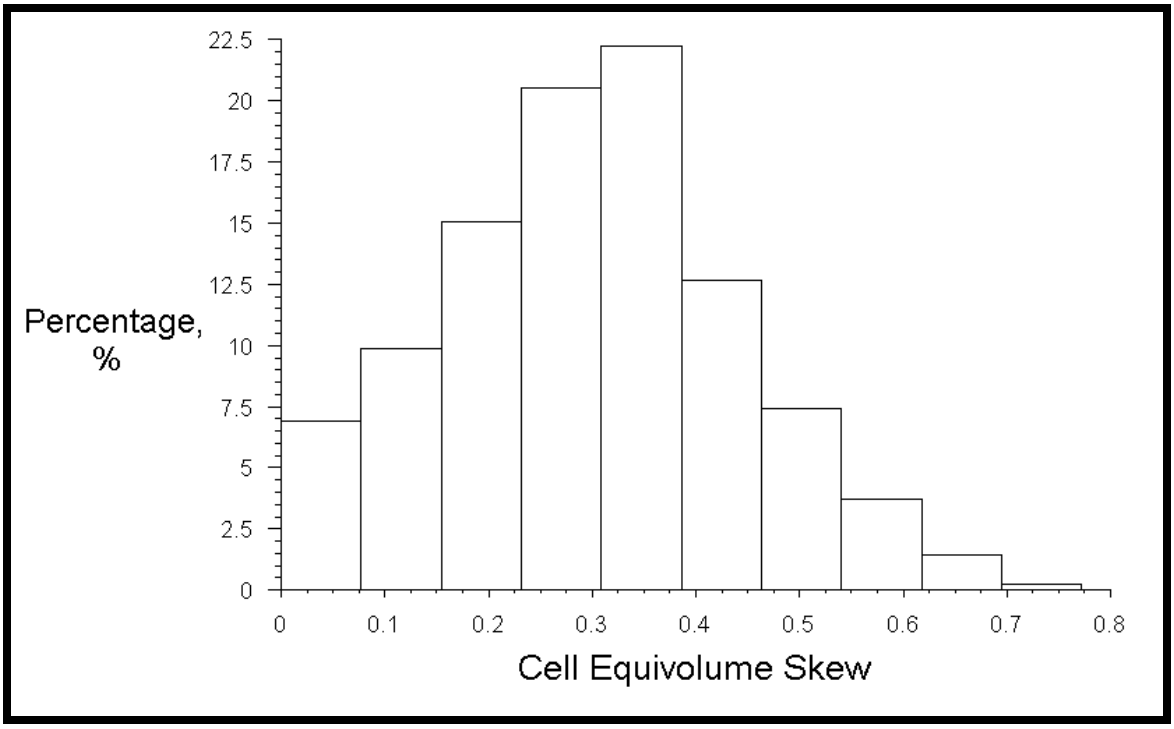

Figure 4.5. Equivolume skew of the mesh of PU300 model.

4.5 SOLUTION

The numerical solution is initialized by guessing the velocity field. The minimum residual for solution convergence is defined as follows:

- Continuity, u-velocity, v-velocity and w-velocity $\leq 1 \times 10^{-4}$
- Energy $\leq 1 \times 10^{-8}$

The solution is iterated to the convergence point where the minimum residual range is achieved. At this point, airflow characteristics such as velocity, pressure, turbulence intensity, temperature and others are predicted in all regions of the system. Figure 4.6 shows convergence behavior of the selected grid size of 800,000 cells up to 1000 iterations.

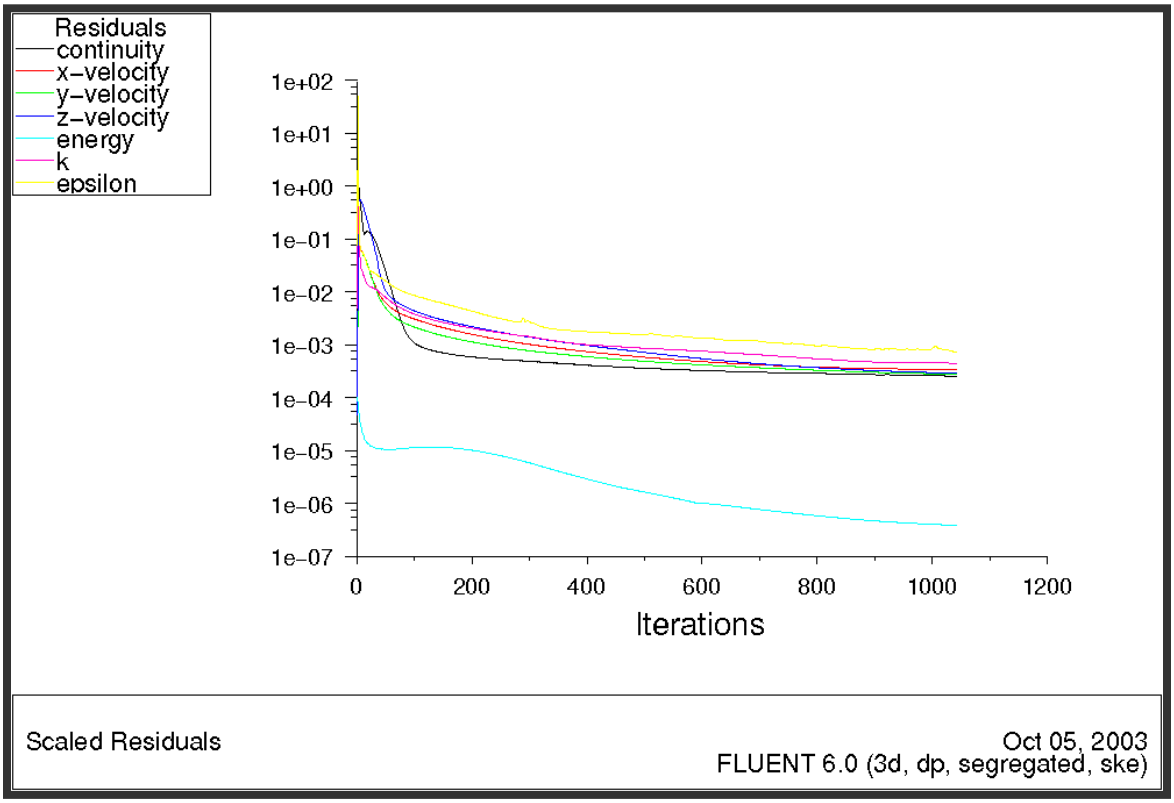

Figure 4.6. Convergence behavior of the solved CFD model.

4.6 GRID INDEPENDENT STUDY

A grid independent test is performed prior to selecting a suitable base case of the CFD model. The effect of finer and coarser mesh sizes is observed. Five independent grids with different number of cells are constructed. These independent grids include following number of cells: 255,000, 444,000, 570,000, 800,000 and 1,000,000. The objective is to reach a state where the predicted flow characteristics do not change (within a small tolerance) when refining the grid further.

The comparison between each independent grid is performed by means of the predicted flow characteristic such as: airflow rate, velocity profiles, pressure and temperature. They are taken in some regions of the flow field. Table 4.1 includes the predicted airflow rate for each grid. It also includes the average pressure and temperature over the surface integral of the identified planes. It is noticed from table 4.1 that the flow rate values are changing as the finer grid is applied. But the change is very small between the last two grids (800,000 and 1,000,000), where the values of flow rates are 12,763 ft^3/min and 12,728 ft^3/min as in Table 4.1. This change is very small (within 0.3%) and could be neglected. Also, the change in pressure values notices a decrease in the last two grids. Last, the air temperature values show small change between the last two grids.

Table 4.1. Mesh independent study.

		Mesh Size /1000				
		255	**444**	**570**	**800**	**1000**
Air flow rate, ft^3/min	Inlet	13,022	12,711	12,952	12,763	12,728
Static Pressure, in. w.g	Plane B - B upstream evap.	*0.17*	*0.18*	*0.14*	*0.15*	*0.17*
	Evaporator	*-0.04*	*-0.02*	*-0.06*	*-0.05*	*-0.02*
	Plane A - A downstream evap.	*-0.04*	*-0.02*	*-0.06*	*-0.04*	*-0.02*
	Plane C - C fan inlet # 1a	*-2.10*	*-1.88*	*-1.94*	*-1.96*	*-1.89*
	Plane D - D fan inlet # 1b	*-1.96*	*-2.01*	*-2.17*	*-1.93*	*-1.98*
	Plane E - E fan inlet # 2a	*-2.08*	*-2.09*	*-2.25*	*-2.02*	*-2.00*
	Plane G - G fan inlet # 2b	*-2.02*	*-1.78*	*-1.87*	*-1.92*	*-1.88*
	Outlet	*0.15*	*0.15*	*0.15*	*0.15*	*0.15*
Temperature, Deg. F	Inlet	80.00	80.00	80.00	80.00	80.00
	Plane B - B upstream evap.	79.68	79.65	79.68	79.38	79.39
	Evaporator	64.24	63.63	63.28	62.78	62.46
	Plane A - A downstream evap.	55.09	55.08	55.09	54.97	54.99
	Plane C - C fan inlet # 1a	54.27	54.10	54.10	54.21	54.25
	Plane D - D fan inlet # 1b	55.94	55.04	55.04	54.84	54.86
	Plane E - E fan inlet # 2a	55.49	55.53	55.53	55.33	55.35
	Plane G - G fan inlet # 2b	55.04	55.94	55.98	55.94	55.96
	Outlet	55.17	55.17	55.17	55.29	55.22

Figures 4.7–4.10 show some profiles of the predicted velocity components in some regions upstream and downstream of the evaporator. The velocity profiles are compared for all the grids on the same chart. It is observed that all velocity profiles have similar shape for all the grids. It is also noticed that a velocity jump exists always between third and fourth grid (570,000 and 800,000). But in the last grid (1,000,000), this change is small. This is clearly highlighted in the regions near the wall of the unit.

From the above analysis, it could be concluded that the fourth grid of 800,000 cells could be assumed to give as grid-independent results. Hence, the grid of 800,000 cells will be the base case for analysis of the predicted flow characteristics for the remaining of this study.

Finally, it should be mentioned that the computer used in this study is a Pentium III type with 1.2 GB RAM. It requires about 28 days of continuous operation to run and solve a case of one million cells.

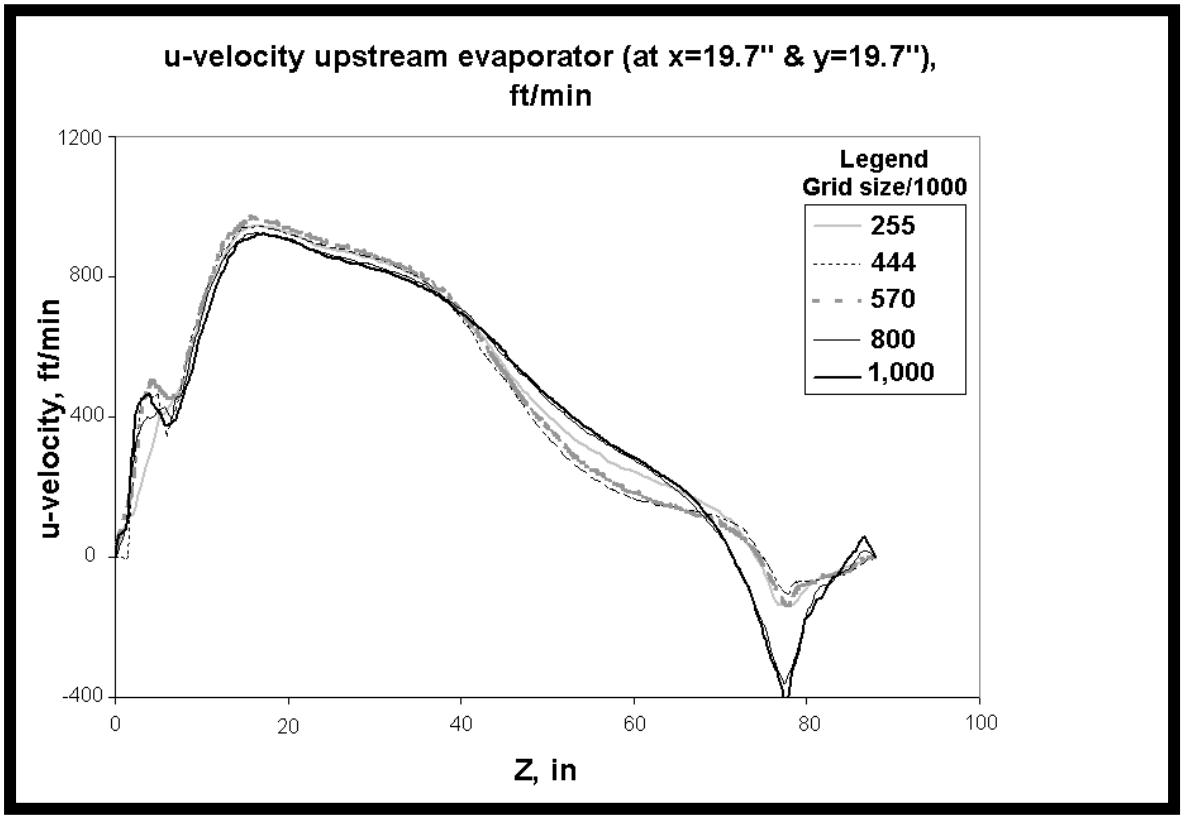

Figure 4.7. u-velocity upstream of the evaporator for different grids.

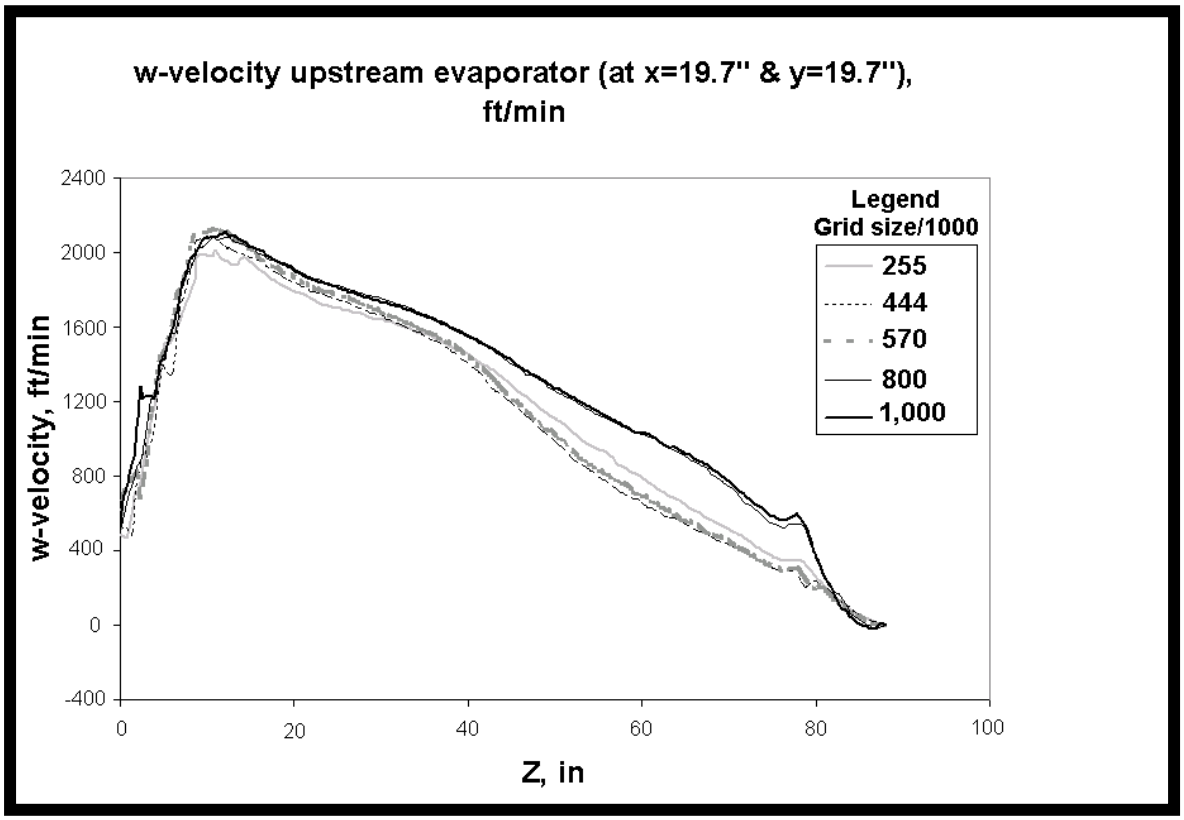

Figure 4.8. w-velocity upstream of the evaporator for different grids.

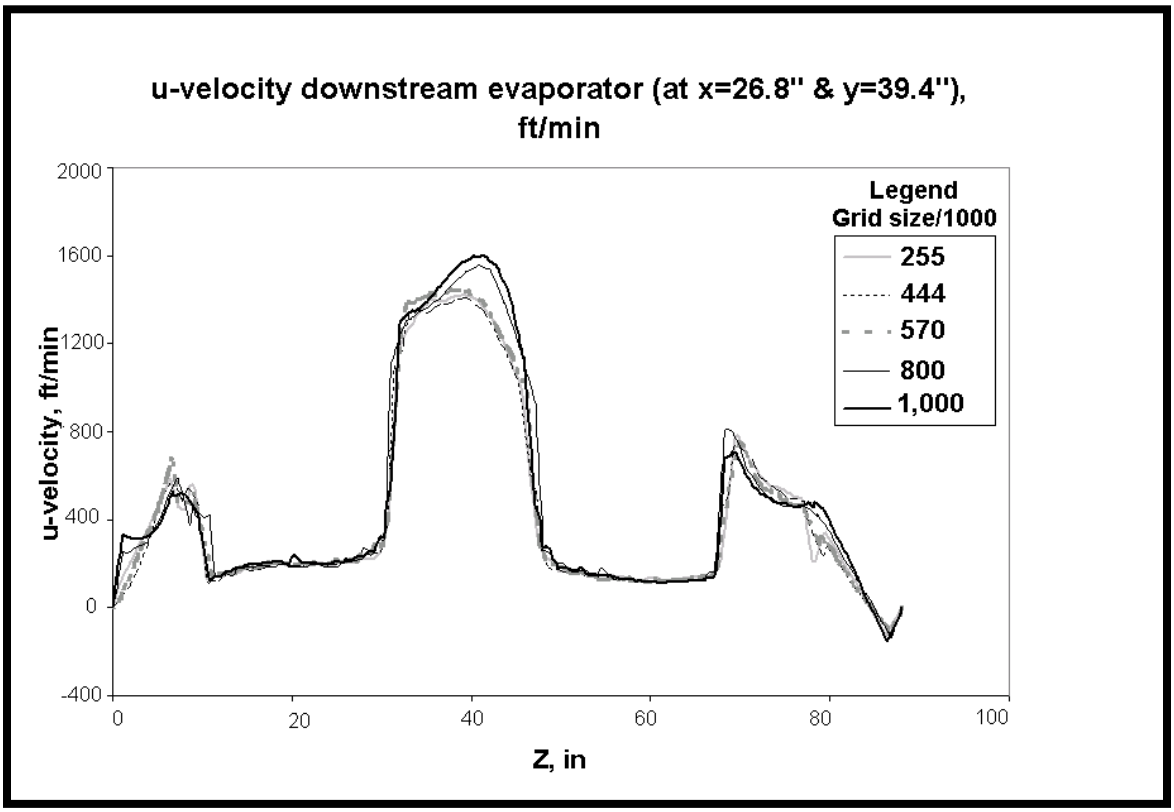

Figure 4.9. u-velocity downstream of the evaporator for different grids.

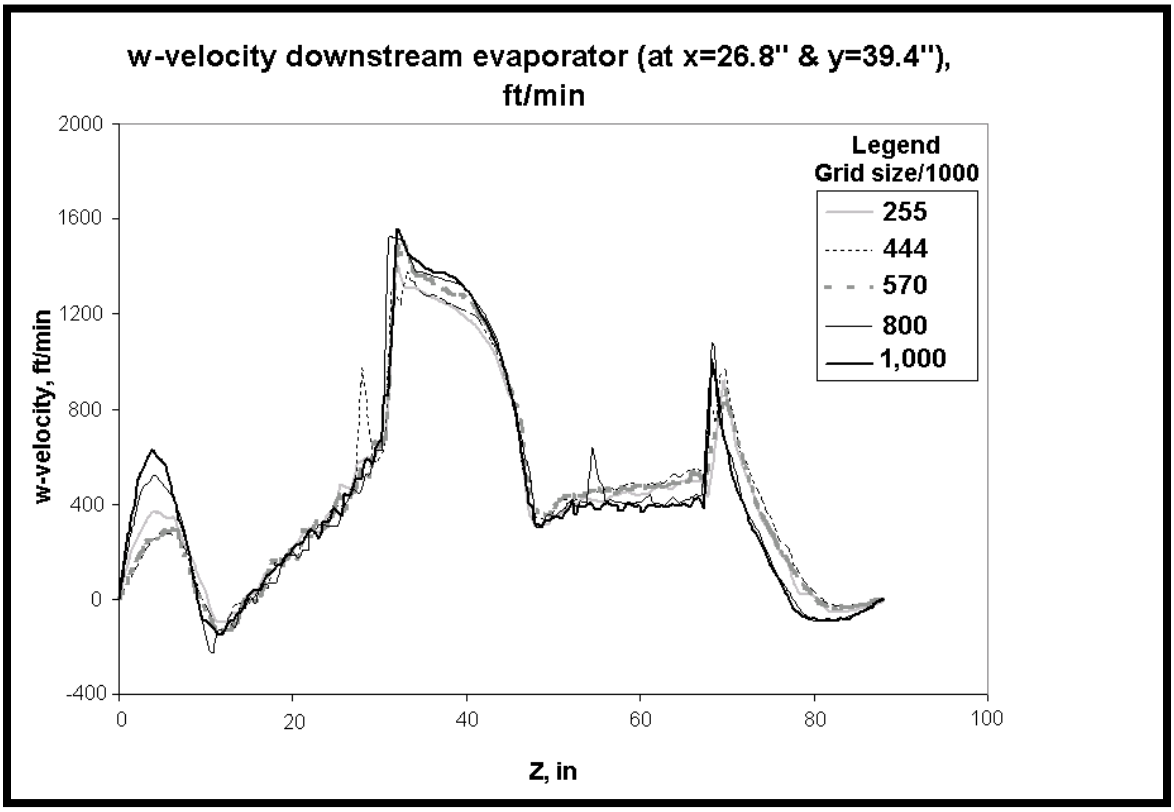

Figure 4.10. w-velocity downstream of the evaporator for different grids.

CHAPTER 5

CFD RESULTS AND VALIDATION

5.1 GENERAL

The predicted airflow pattern in the packaged unit is presented in terms of velocity distribution across the specified planes in the unit. Magnitude and components of velocity (u, v and w) are presented to help identifying re-circulation regions. To see the effect of fan model on the pressure distribution, the static pressure at these planes is investigated. The heat transfer across the evaporator is observed by means of air temperature distribution at a plane downstream of the evaporator. The regions of high turbulence may be observed by presenting values of turbulence intensity.

For the purpose of experimental validation, the same planes used in experimental measurements (Chapter 3) are also chosen here. Table 5.1 and Figure 2.8 show the specified planes for presentation purposes.

Table 5.1. Plane identification

Plane (Section)	Plane Name	Figure #
A-A	Vertical plane at 1.4 in. downstream evaporator	Figure 2.9
B-B	Vertical plane at 2.4 in. upstream evaporator	Figure 2.9
C-C	Vertical plane at fan inlet # 1 (left face)	Figure 2.10
D-D	Vertical plane at fan inlet # 1 (right face)	Figure 2.10
E-E	Vertical plane at fan inlet # 2 (left face)	Figure 2.10
F-F	Plane normal to fan outlet (both #1 and 2)	Figure 2.11
Inlet & Outlet	Plane covers inlet and outlet faces	Figure 2.12

The predicted flow on each plane is presented on contour maps. Contour levels represent the magnitude of the respective data on the plane. To present the flow pattern in the unit, some vector plots are shown for the air velocity on horizontal and vertical planes across the unit.

Comparison of the CFD results with the experimental ones is discussed here. Note that the magnitude of velocity components are used to compare with the measured air speed values.

5.2 MAIN FLOW REGIME

The airflow in the PU300 unit enters through the inlet face. Then it passes across the evaporator towards four fan inlets. The two fans suck air and throw it into the supply section toward the unit outlet, where air leaves the unit. Figures 5.1 and 5.2 show vectors and contours of velocity respectively on horizontal XZ plane cutting the unit at y = 39.3 in.. High velocity magni-

tude is noticed near the unit inlet, fan inlets and fan outlet faces. The unit configuration forces airflow to turn 180° angle between the inlet and the outlet directions. As a result, complex flow and re-circulation zones are noticed in many regions of the flow field. In Figure 5.3, air leaving the fan with high velocity tends to hit the facing wall and then circulates in the upper and lower regions. This phenomenon creates disturbance of flow at the outlet section, which causes eddies that retard the flow leaving the unit through the outlet. In addition, it creates higher static pressure drop in the system further reducing the effective airflow rate. The existence of two fans in the system aims to assure even air distribution across the evaporator. Four fan inlets are provided to suck air from the wide evaporator section. However the fan housing shrouds obstruct the airflow across some regions on the evaporator surface. This may be caused by the small distance between the evaporator and fan housing (about1.6 in.).

Other causes of flow non-uniformity in the system are the fan motor, motor stand, shaft, pulley, bearings and bearing supports. Their location especially near the fan inlets adds resistance to the flow entering each fan inlet. In addition, it creates high turbulence and air circulation in the same region.

Flow re-circulation and stagnant regions are identified at each plane in the flow field. Their effect on the performance of the packaged unit is evaluated in the next sections.

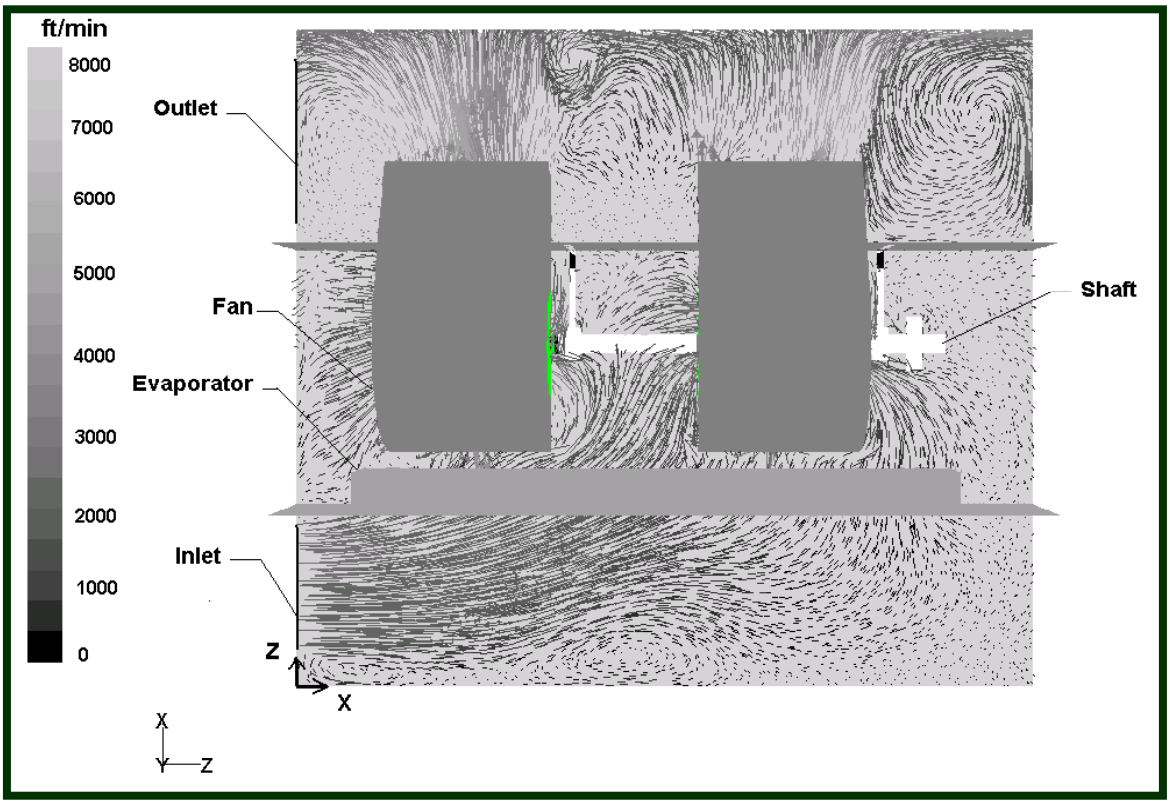

Figure 5.1. Velocity vector in the horizontal plane at y = 39.4 in.

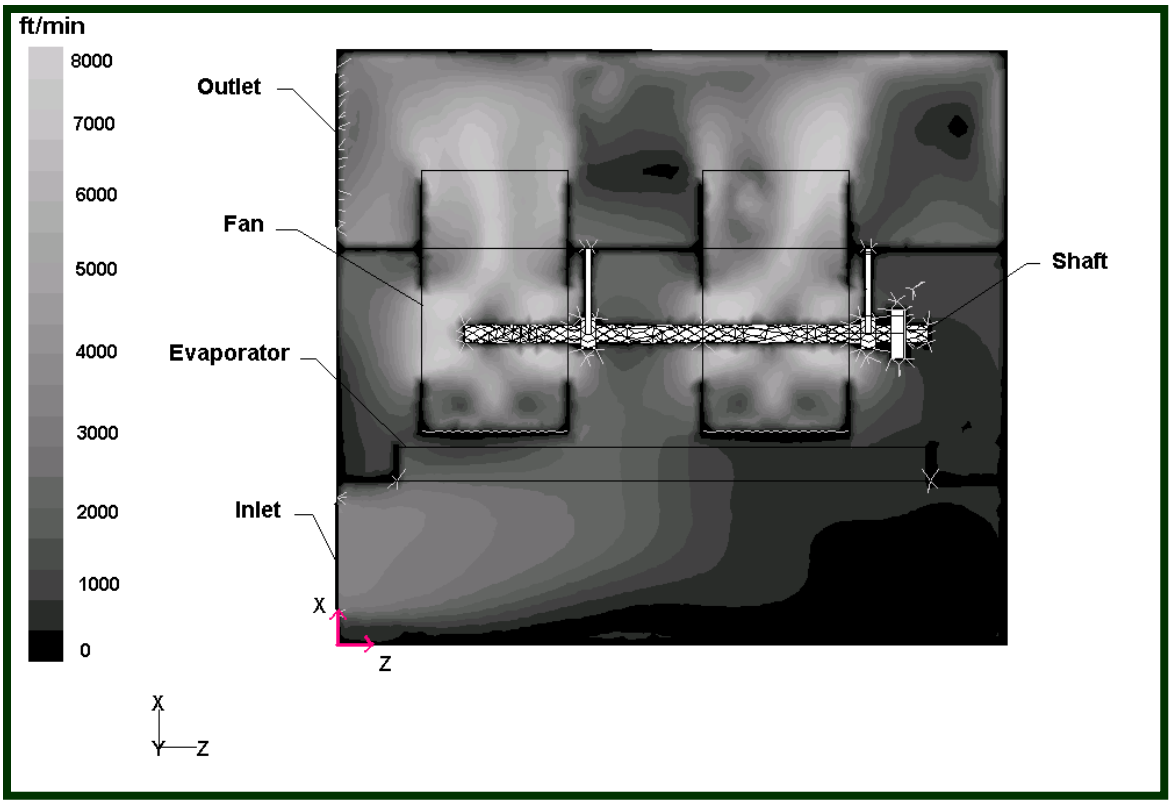

Figure 5.2. Contours of velocity magnitude in the horizontal plane at y = 39.4 in.

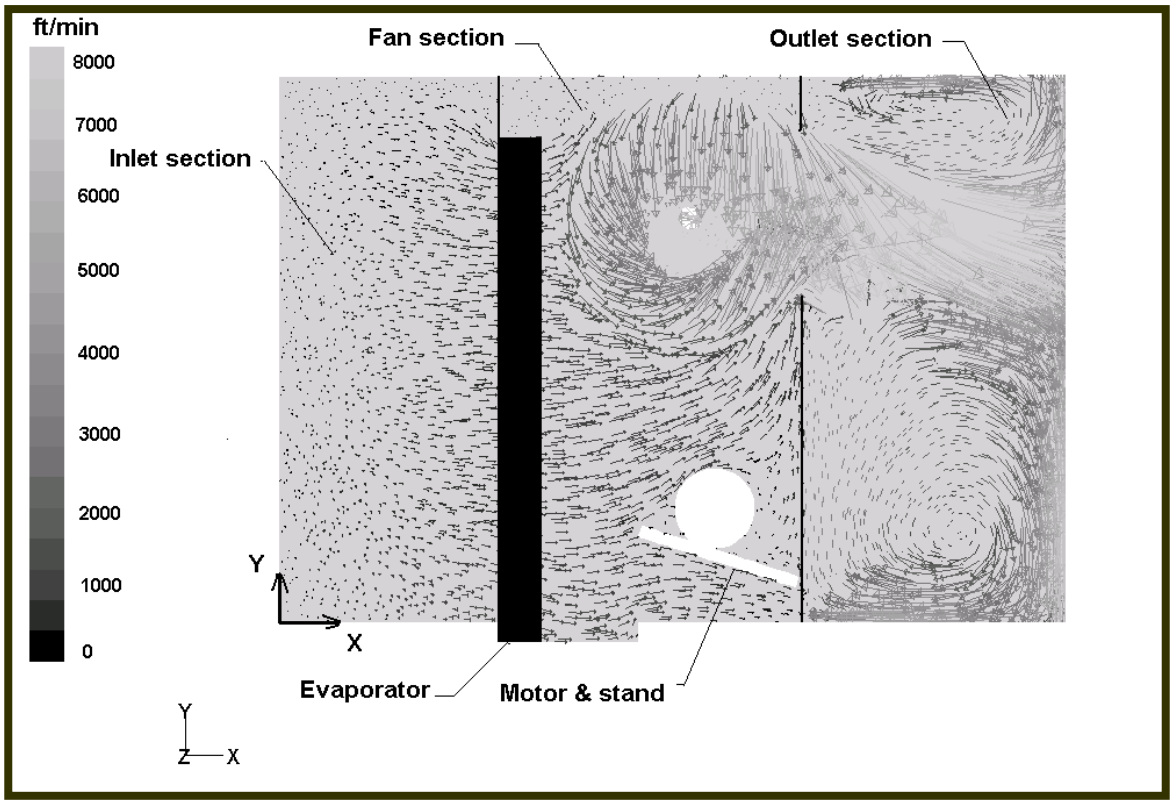

Figure 5.3. Velocity vector in the vertical plane at z = 66 in.

5.3 INLET

The predicted airflow w-velocity (z-component) at the unit inlet face is almost uniform (see Figure 5.4). The inlet face is considered as a pressure boundary type, and set at atmospheric pressure. This is assumed based on an open inlet duct to the atmosphere. The predicted airflow rate (Q) entering the PU300 unit is calculated by a surface integral as follows:

$$Q = \iint_{inlet} w(x, y) \cdot dx \cdot dy \tag{5.1}$$

$$Q \cong \sum_{j} \sum_{i} w_{ij} \cdot \Delta x_i \cdot \Delta y_j \tag{5.2}$$

where, dx and dy refer to the integration of the cross sectional area of the inlet face, and w is the velocity component in the z-direction. The predicted value of Q is 12,763 ft^3/min. This value of airflow rate is slightly less than the experimental value (12,931 ft^3/min). The difference is within 2 %. Figure 5.4 shows increasing values of the w-velocity on the inlet area next to the evaporator. To identify the flow regime in the unit, the Reynolds Number (Re) is computed as follows:

$$\mathrm{Re} = \frac{\rho \overline{V} D_H}{\mu} \tag{5.3}$$

where $\overline{V}$ is the average air velocity at inlet. It is computed by integrating the w-velocity on the cross sectional surface area of the inlet face as follows:

$$\overline{V} = \frac{1}{A_{inlet}} \int_{A} \vec{V}_{inlet}(x, y) dA = 2{,}384 \text{ ft/min} \tag{5.4}$$

and A_{inlet} is the cross sectional area of the inlet face that is equal to 4.91 ft^2 (0.456 m^2). D_H is the hydraulic diameter of inlet cross section, which is calculated as follows:

$$D_H = \frac{4 \cdot A}{p} = \frac{4(0.456)}{3.16} = 0.577 \ \ m \tag{5.5}$$

ρ is the air density, taken as 1.225 kg/m^3 and μ is the dynamic viscosity of air set at 1.85x10^{-5} N.s/m^2. Substituting above values in equation (5.3) results in Re = 462,683. This indicates fully turbulent flow at inlet face. Figure 5.5 shows the percentage (%) of turbulence intensity that accounts for velocity fluctuation at inlet face. Turbulence intensity (TI) is derived from the kinetic energy of turbulence assuming isotropic turbulent field as:

$$TI = \frac{\sqrt{\frac{2}{3}k}}{U} \tag{5.6}$$

where, k is the turbulent kinetic energy and U is the mean velocity magnitude. The values of turbulence intensity do not exceed 1.5%, which is expected as the air moves at the inlet section without obstruction.

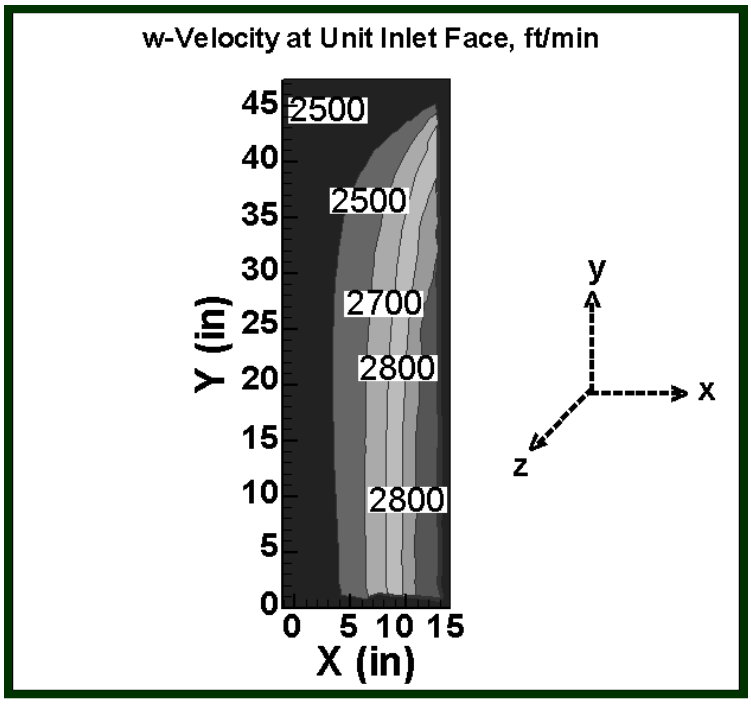

Figure 5.4. w-velocity predicted at unit inlet.

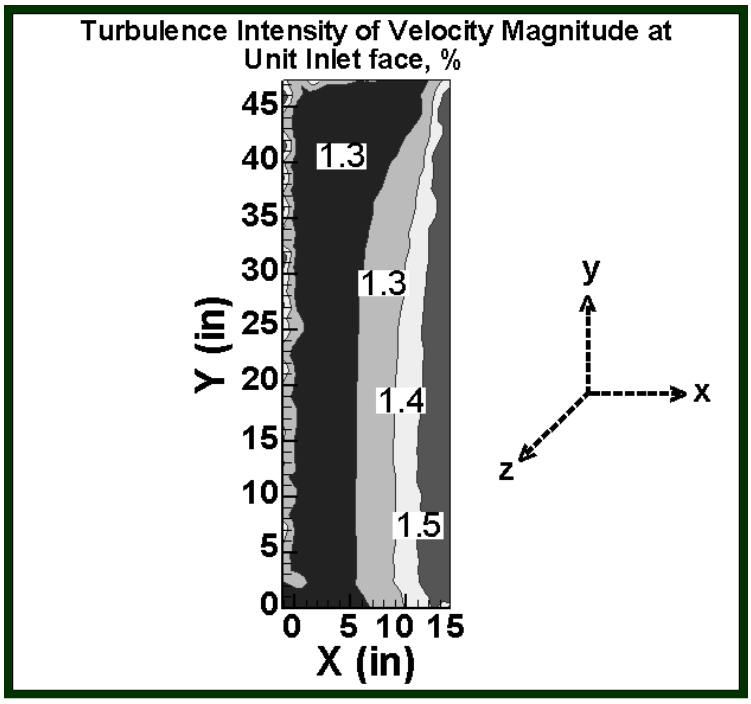

Figure 5.5. Turbulence intensity of velocity magnitude at unit inlet.

5.4 EVAPORATOR

The high velocity air entering the inlet of the PU300 unit tends to turn at 90° angle to pass across the evaporator coil, which leads to flow maldistribution. Good airflow distribution immediately before the evaporator is desired in order to gain better performance of the evaporator. An even air distribution across the whole evaporator surface area improves the overall heat transfer between refrigerant tubes and air.

The airflow distribution across the evaporator is investigated by observing the planes upstream and downstream of it.

5.4.1 PLANE B–B UPSTREAM OF THE EVAPORATOR

Plane B–B at distance 2.4 in. upstream of the evaporator (refer to Figure 3.10 for reference) is selected to study flow pattern prior to the evaporator. Velocity magnitude and turbulence intensity at Plane B–B are shown in Figures 5.6 and 5.7. Higher velocity magnitude is noted upstream of the evaporator in the regions closer to the unit inlet. The velocity magnitude decreases gradually as the distance increases in the z-direction.

The three components of velocity at the same plane are presented in Figures 5.8, 5.9 and 5.10. It is found that the v-velocity ranges between -300 and 200 ft/min. Hence the flow upstream of the evaporator is dominated by the u and w-velocity components. The u-velocity decreases as one moves towards the far end of the evaporator surface (see Figure 5.8). In Figure 5.11, the static pressure upstream of the evaporator surface ranges between 0 to 0.25 in. w.g (inch of water gauge). The air entering the unit with zero static pressure is subjected to deceleration of velocity. The static pressure increases in the positive z-direction.

5.4.2.2 Experimental Validation of Plane B–B

Comparisons between the experimental and predicted velocity components are shown in Figures 5.12 and 5.13. They are taken on horizontal flow lines at y-positions of 10 in., 20 in., 30 in. and 40 in. on the plane B–B. The values of u-velocity show relatively good agreement in positions at low and medium distances of z-axis. However, no good agreement occurs in the remainder of the plane. The difference may be due to the re-circulation zone in the inlet section upstream of the evaporator. In Figure 5.13, the experimental measured values of w-velocity component are higher than the predicted ones. The difference may be due to experimental errors as well as numerical errors.

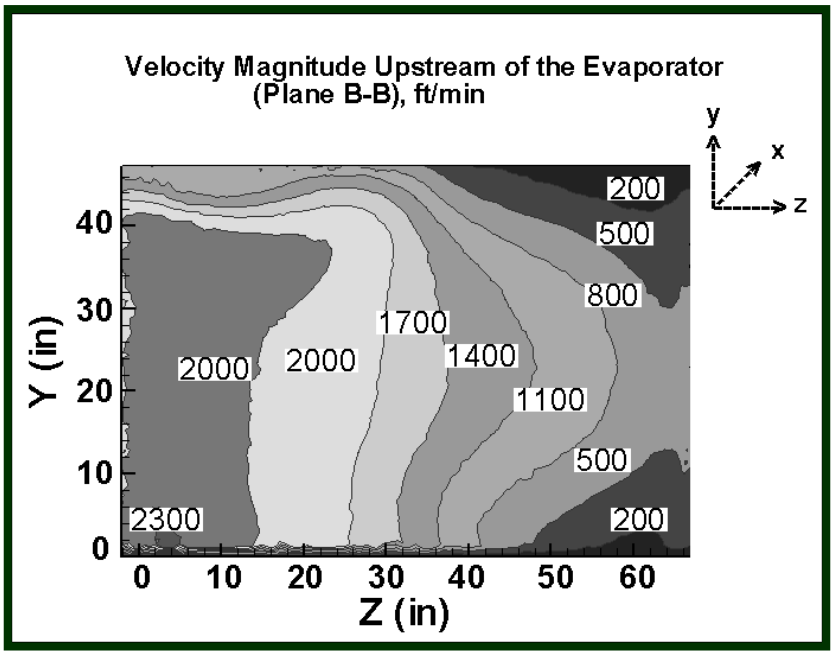

Figure 5.6. Velocity magnitude predicted upstream of the evaporator (plane B–B).

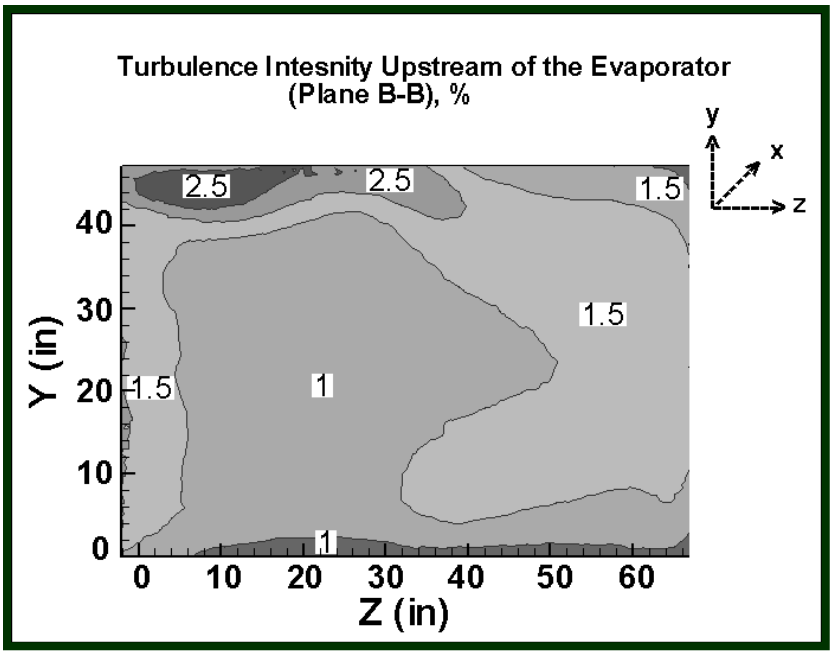

Figure 5.7. Turbulence intensity of velocity upstream of the evaporator (plane B–B).

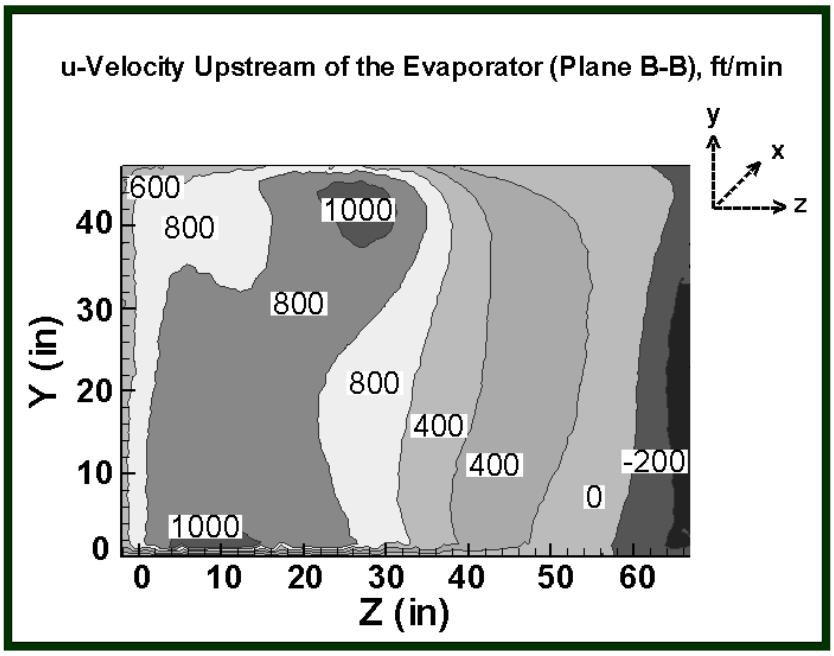

Figure 5.8. u-velocity predicted upstream of the evaporator (plane B–B).

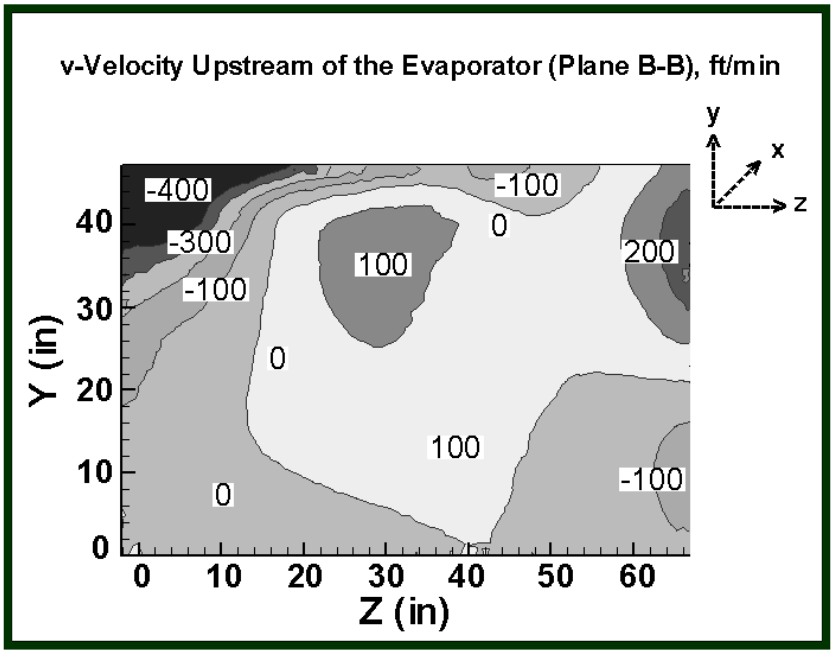

Figure 5.9. v-velocity predicted upstream of the evaporator (plane B–B).

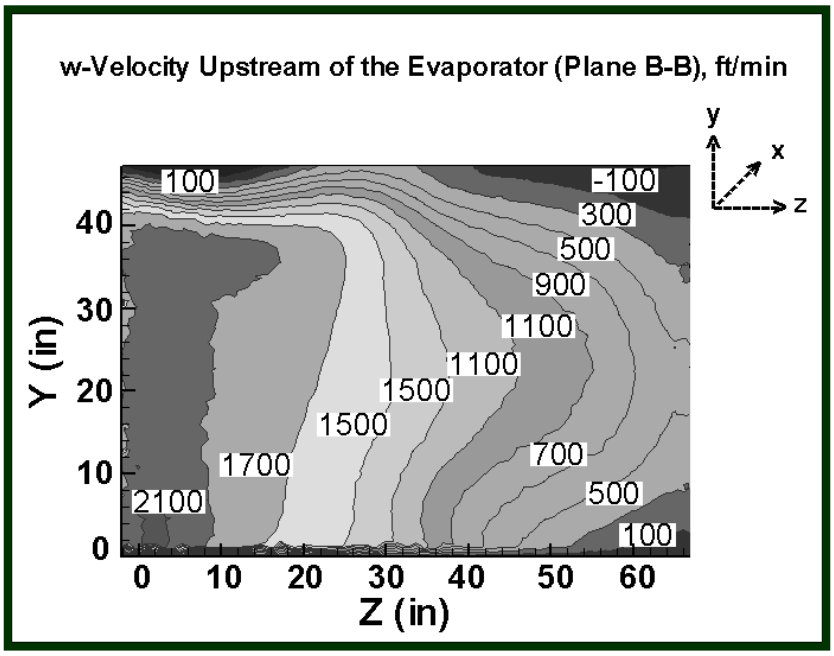

Figure 5.10. w-velocity predicted upstream of the evaporator (plane B–B).

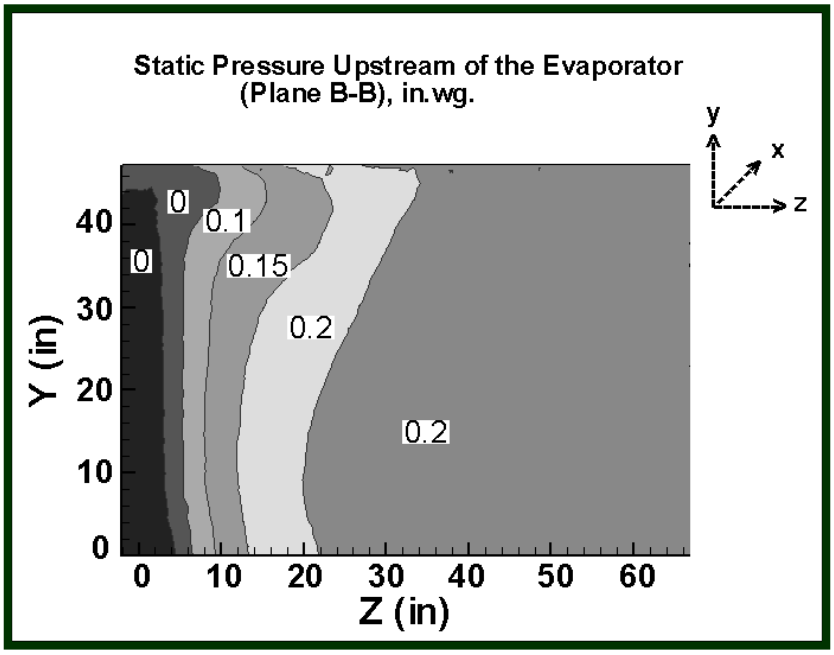

Figure 5.11. Static pressure predicted upstream of the evaporator (plane B–B).

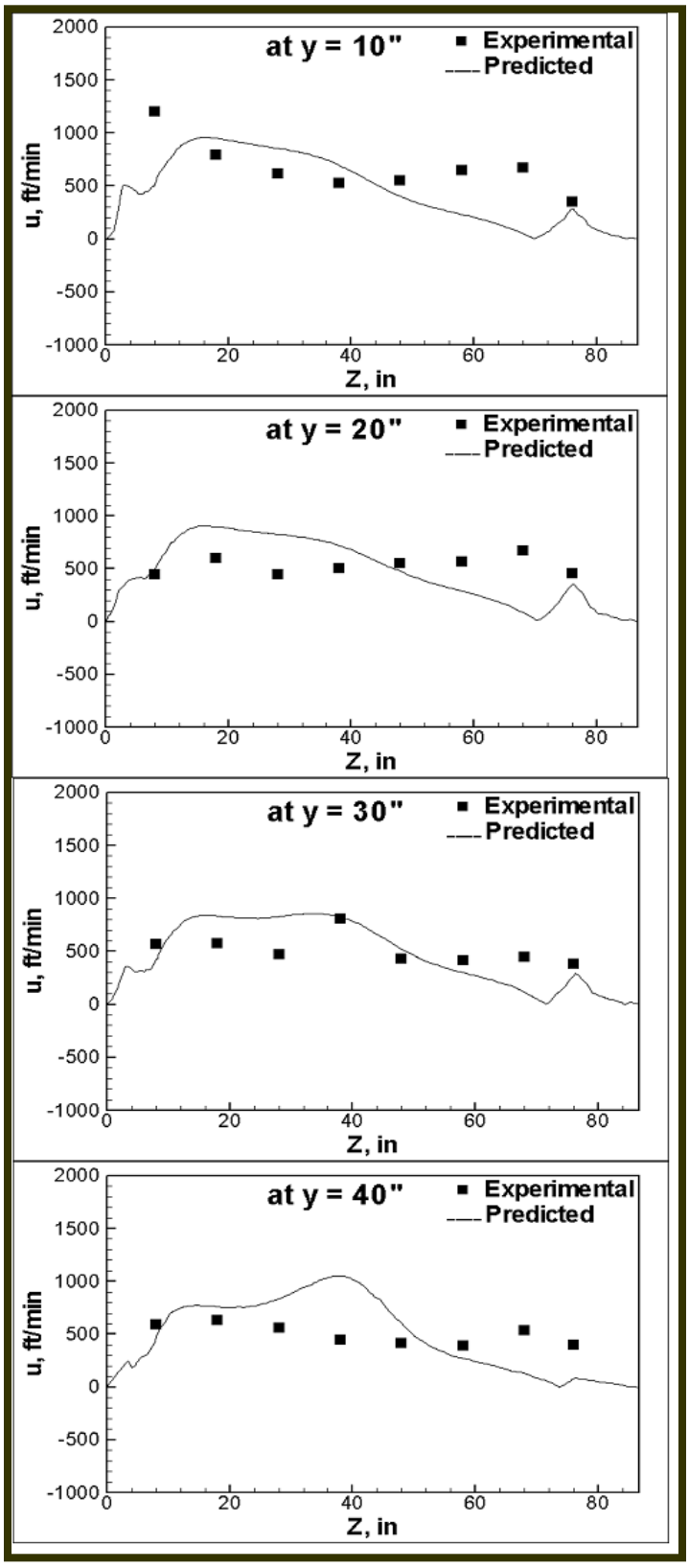

Figure 5.12. Comparison between experimental and predicted u-air speed at plane B-B.

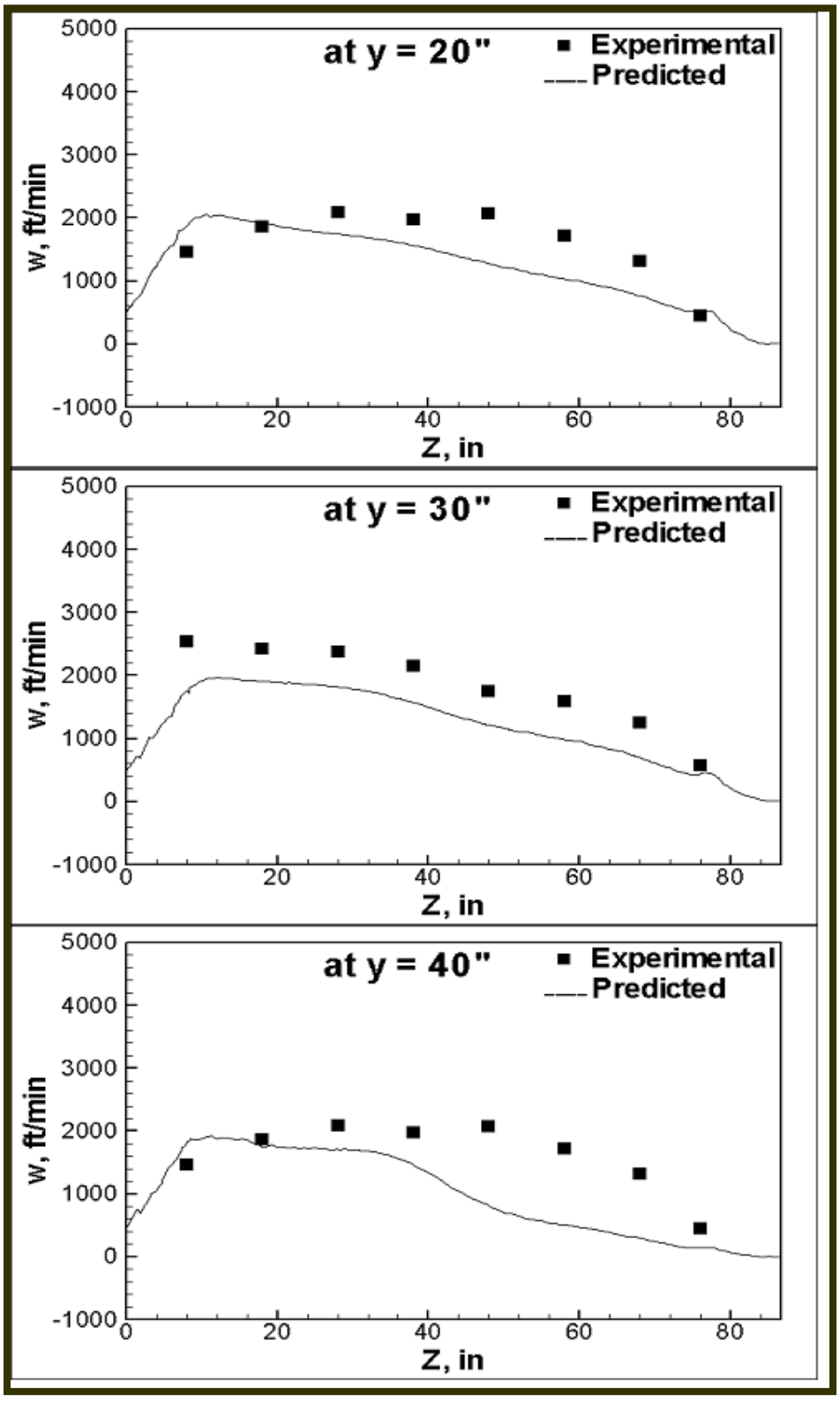

Figure 5.13. Comparison between experimental and predicted w-air speed at plane B-B.

5.4.2 PLANE A–A DOWNSTREAM OF THE EAPORATOR

Plane A–A at 1.4 in. downstream of the evaporator (refer to Figures 2.8 and 2.9 for reference) is selected to study the behavior of airflow leaving the evaporator. Contours of velocity magnitude and components at plane A–A are shown in Figures 5.14 to 5.18. Non-uniform velocity distribution is observed as the magnitude ranges between 200–2000 ft/min. The predicted volume flow rate (Q = 12,876 ft^3/min) across the evaporator with surface area (A = 21.875 ft^2) gives an average velocity of 588 ft/min. There exist some locations of low velocity especially behind fan housing. The flow is also obstructed due to the narrow space between the evaporator and the two fans.

Slightly higher turbulence intensity is noticed upstream of the evaporator in comparison to the downstream flow. The turbulent intensity in the upstream flow ranges between 1–2.5% while it ranges between 1 – 2% in the downstream plane as shown in Figure 5.15. This may be due to the fact that airflow is straightened as it leaves evaporator. The vertical v-velocity varies between negative and positive values behind the wide region of evaporator surface. The u-velocity values are all positive while w-velocity has large values in the mid region of z-axis as shown in Figure 5.18. The velocity field downstream of the evaporator is quite complex as air is sucked by the two fans.

Relatively large static pressure variation is noticed downstream of the evaporator (see Figure 5.19). It is known that static pressure drop across evaporator depends on airflow velocity. Higher velocity leads to higher pressure drop. This is obvious when comparing between static pressure downstream and upstream planes.

In the radiator model of the evaporator, the heat transfer coefficient is a function of air velocity passing through evaporator. Figure 5.20 shows contours of air temperature at plane A–A. The temperature ranges between 54 and 60° F. The regions of higher velocity give higher temperatures. An increase in air velocity leads to increase of both heat transfer coefficient and mass flow rate. This further leads to an increase in the cooling capacity. The mass weighted average of the air temperature (T_b) downstream of the evaporator is calculated by integrating the temperature on plane A–A as follows:

$$T_b = \frac{1}{\dot{m}} \int_A \rho \cdot u \cdot T \cdot dA = \frac{1}{\rho \cdot Q} \int_A \rho \cdot u \cdot T \cdot dA = 55^\circ F \tag{5.7}$$

To calculate total cooling capacity (q) taking place across the evaporator as:

$$q = \dot{m} \cdot C_p \cdot \left(T_{in} - T_{out}\right)$$

$$q = \rho \cdot Q \cdot C_p \cdot \left(T_{in} - T_{out}\right) \tag{5.8}$$

$$q = 1.225 \times 6.08 \times 1007 \times \left(26.7 - 12.78\right) = 104{,}402\ W$$

where, Q is the volume flow rate of the system in m^3/s, and T_{in} is the entering air temperature. The above value of heat transfer is equivalent to 29.7 tons or (356,320 Btu/hr) of cooling capacity, which the system offer based on the operating conditions.

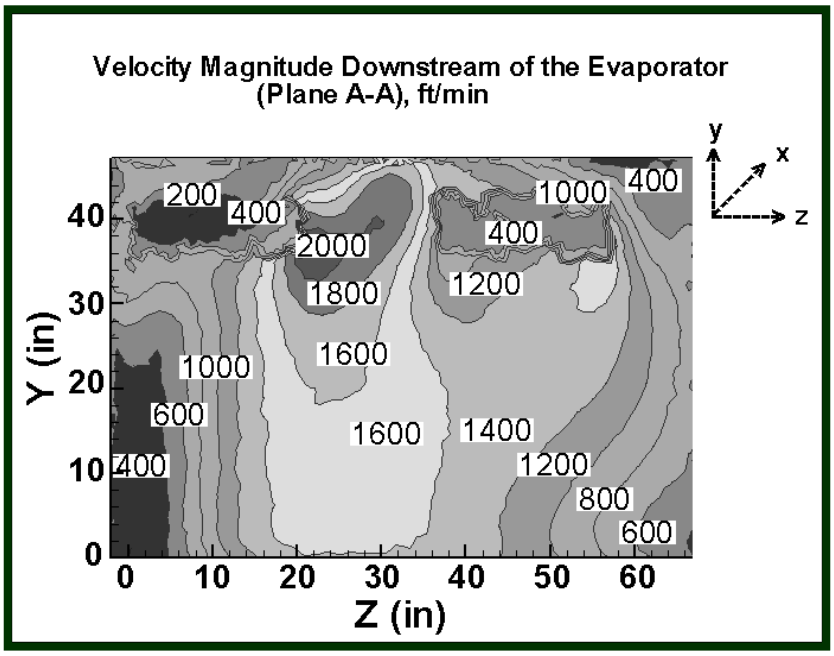

Figure 5.14. Velocity magnitude predicted downstream of the evaporator (Plane A-A).

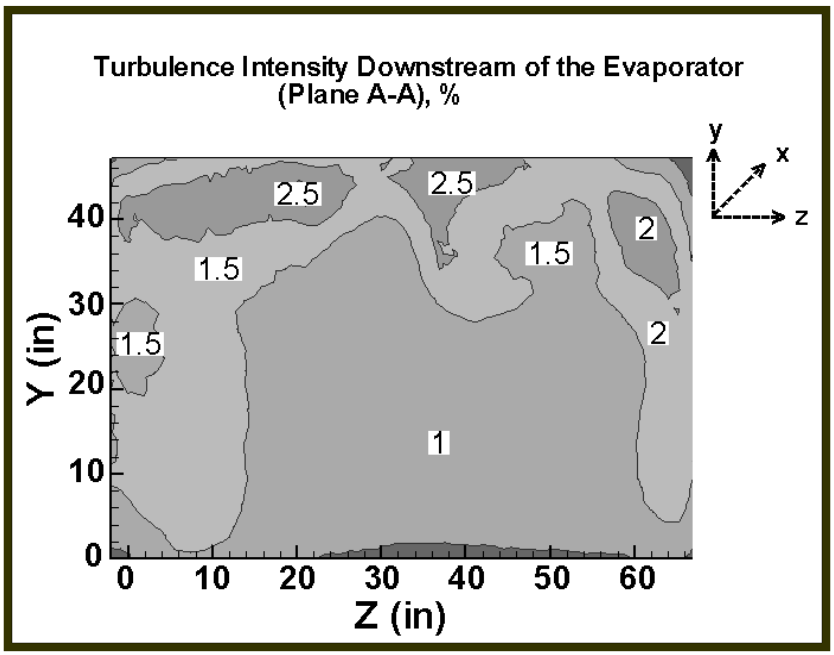

Figure 5.15. Turbulence intensity of velocity downstream of the evaporator (Plane A-A).

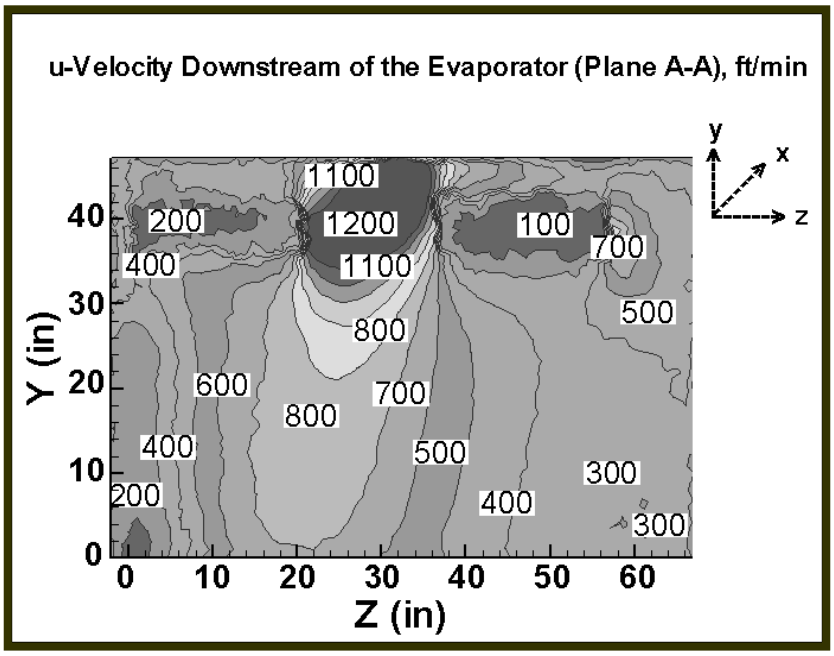

Figure 5.16. u-velocity predicted downstream of the evaporator (plane A–A).

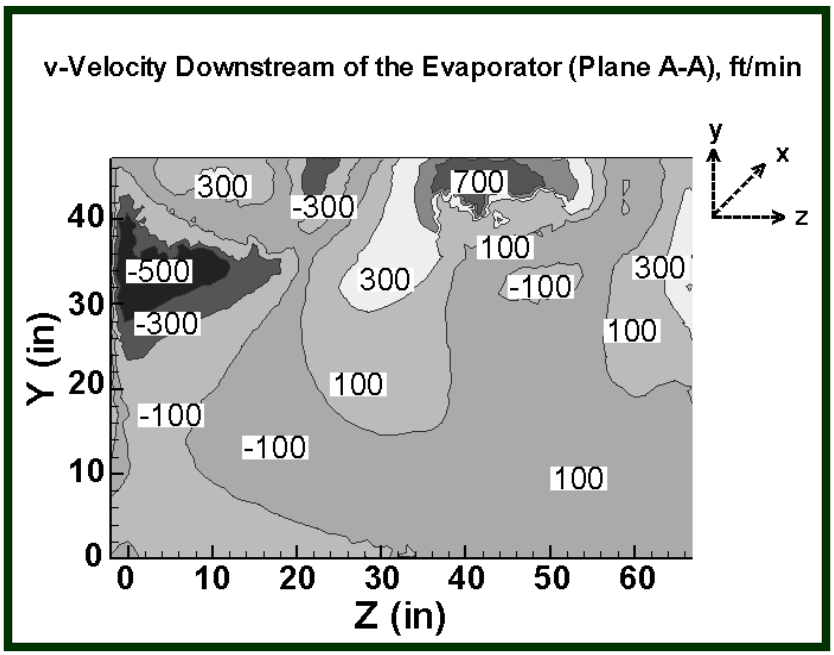

Figure 5.17. v-velocity predicted downstream of the evaporator (plane A–A).

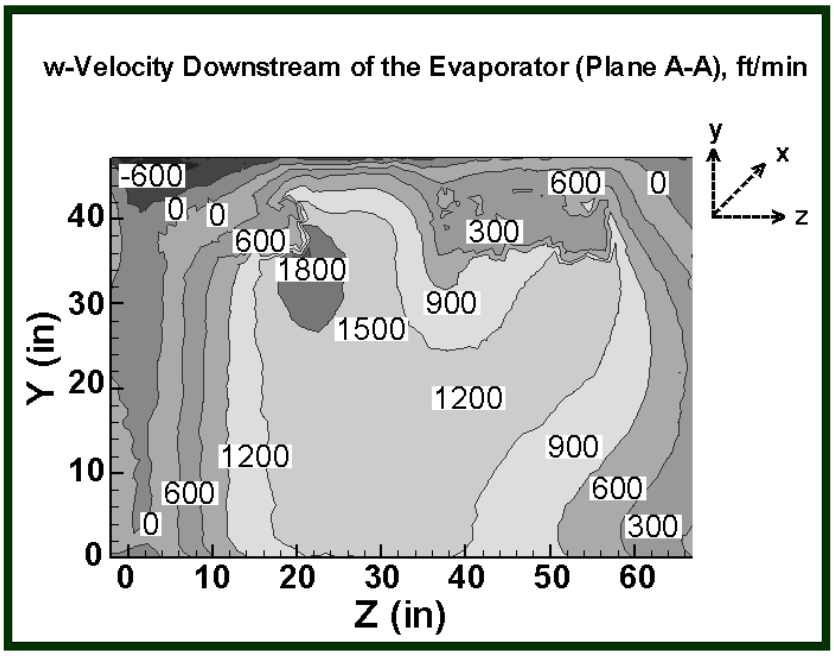

Figure 5.18. w-velocity predicted downstream of the evaporator (plane A–A).

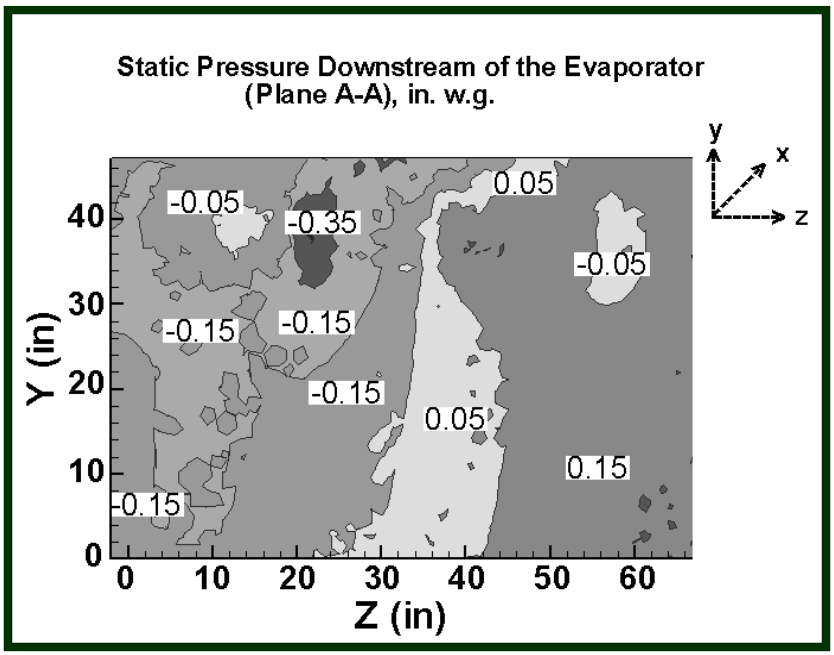

Figure 5.19. Static pressure predicted downstream of the evaporator (plane A–A).

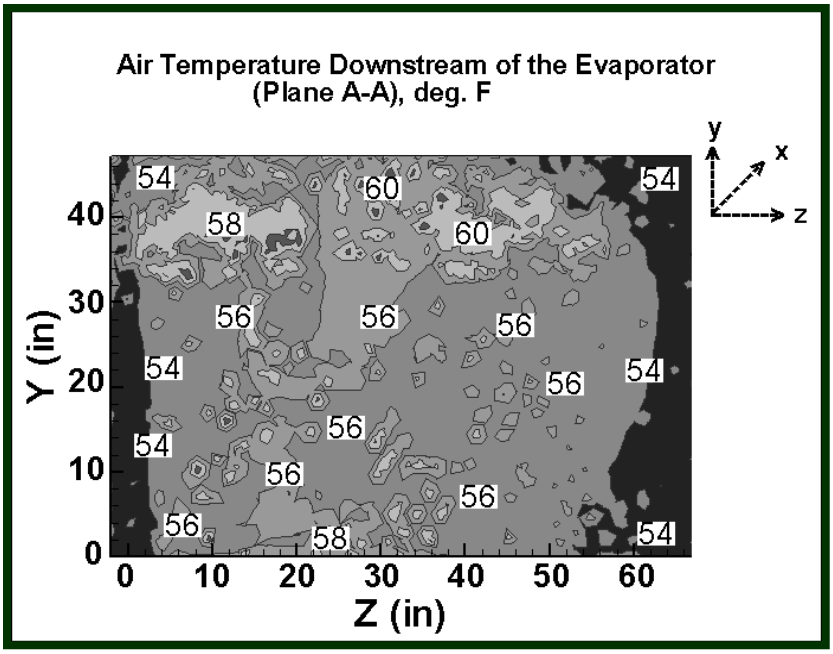

Figure 5.20. Air temperature predicted downstream of the evaporator (plane A–A).

5.4.2.1 Experimental Validation of Plane A–A

Figure 5.21 and 5.22 display the comparison between the experimental and predicted u and v-velocity respectively in plane A-A. Relatively good agreement is noticed of the u-velocity in most of y-positions. This indicates that the predicted flow distribution downstream of the evaporator is similar as the experimental distribution. Good agreement is observed in v-velocity especially in the central positions of plane A–A at y = 20 in. and y = 30 in.. These positions fall in the free area between the fan housing and the fan motor.

In Figure 5.23, the comparison of experimental and predicted air temperature in the same plane is exhibited. The temperature has the same range for the experimental and predicted values of 55-60° F. However, there are large differences between numerical and experimental values in the regions near the wall. This may be due to the coarse mesh near the walls of the CFD model. More importantly, the experimental temperature jump near the wall edge is caused from the bypass air from evaporator, which is not modeled experimentally.

The calculated cooling capacity for both models shows 29.7 tons for the predicted model and 22.5 tons for the experimental one. The increase in the first refers to the porous media introduced in the CFD model. It assumes a constant heat exchanger temperature. This is not the case in the experimental unit since the evaporator surface temperature is not constant across the refrigerant circuits.

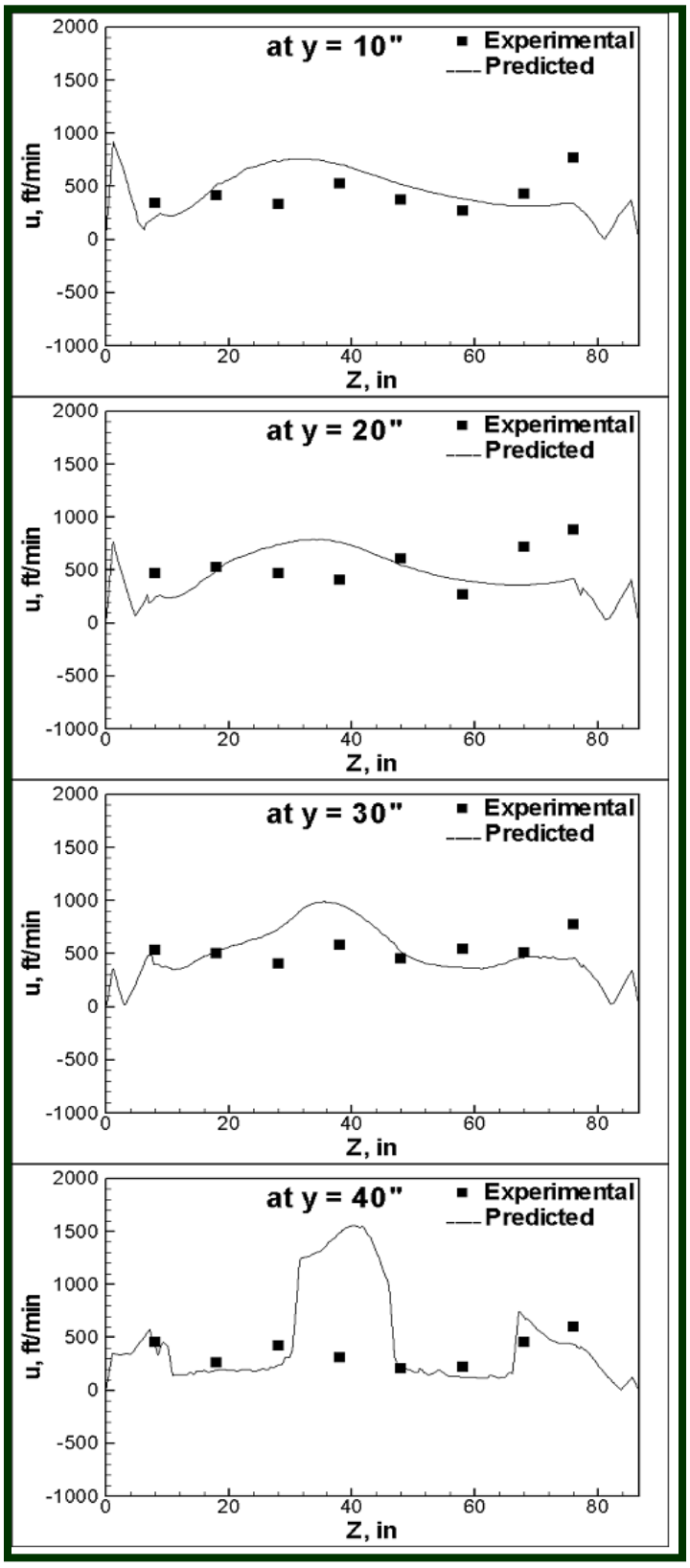

Figure 5.21. Comparison between experimental and predicted u-air speed at plane A–A.

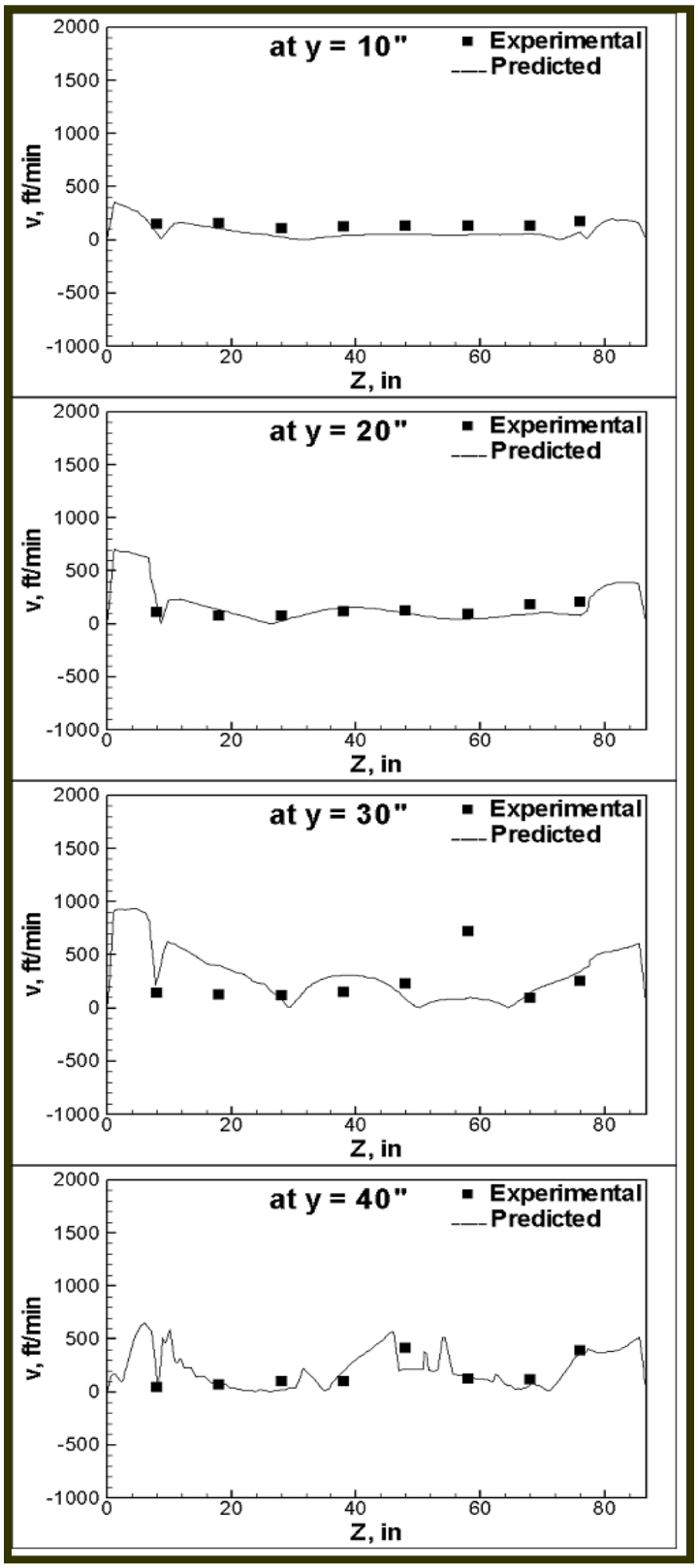

Figure 5.22. Comparison between experimental and predicted v-air speed at plane A–A.

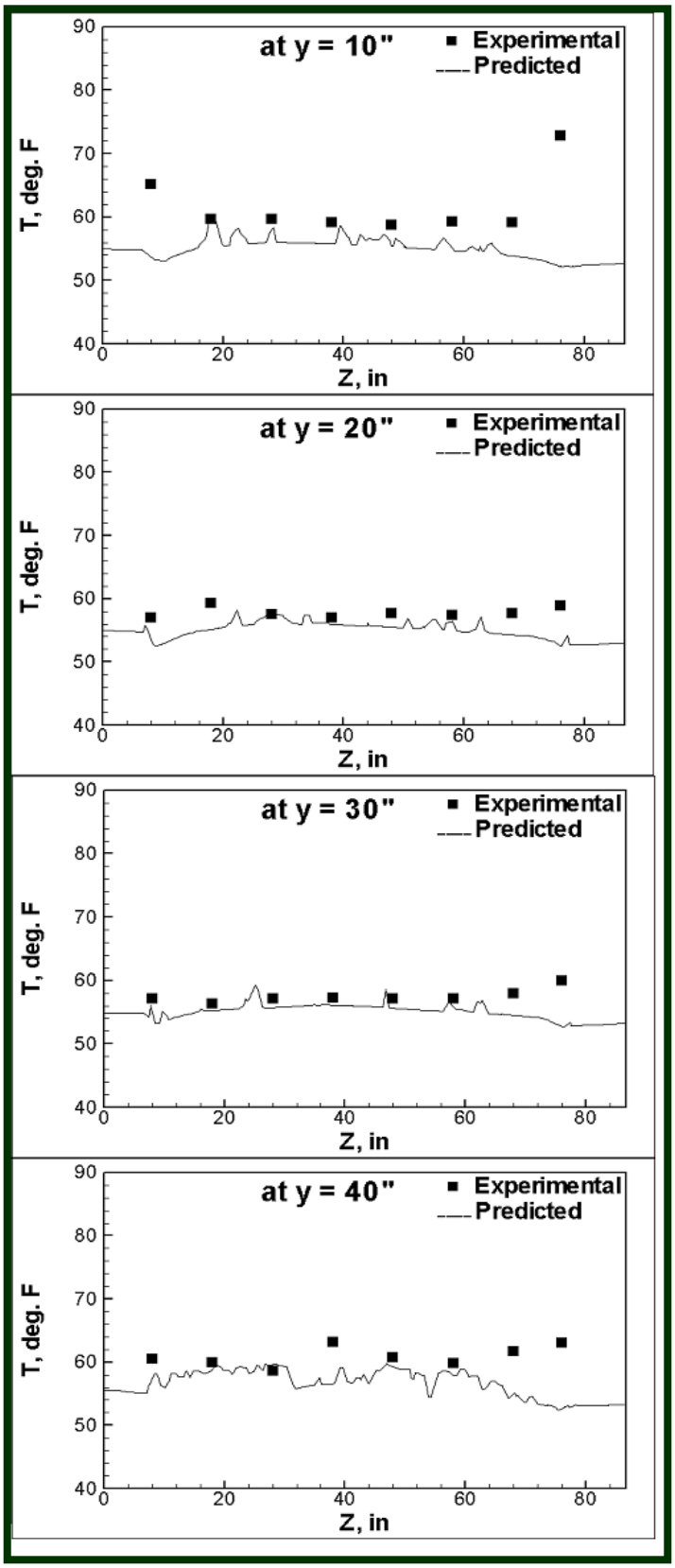

Figure 5.23. Comparison between experimental and predicted temperature at plane A–A.

5.5 FAN

In the computational modeling of the PU300 unit, the two fans are introduced as pressure jump function acting at each fan outlet face. The fan swirl is ignored in this study due to the difficulty of representing its effect on the fan performance. The predicted flow characteristics at both fan inlets and outlets are shown on planes (C-C, D–D, E–E and F–F, see Figure 2.8 and Table 2.10 for reference).

5.5.1 PLANE C–C (FAN # 1 INLET)

Figures 5.24–5.28 show the contours of velocity magnitude and components predicted at plane C–C. High velocity magnitude is noticed at the center of the fan inlet (about 4,500 ft/min). The w-velocity component normal to the plane is in the same range of velocity magnitude indicating that flow is dominantly in the z-direction. The predicted u and v-velocities have lower positive and negative values, since the flow enters fan inlet from all direction in YZ plane.

Large negative static pressure is predicted at plane C–C (Figure 5.29). This is due to the large velocity produced at the fan inlet.

5.5.1.1 Experimental Validation of Plane C–C

For experimental validation of the predicted flow characteristics near the fan inlets of the PU300 unit. Plane C–C is selected for comparing results near the fan # 1 inlet face. Figure 5.30 show the comparison of u-air speed at three horizontal y-positions of plane C–C respectively. The u-air speed shows good agreement between the experimental and predicted results in most of y-positions. This agreement indicates that fan swirl has a minor effect on the flow pattern near the fan

inlet. The fan model in CFD incorporates a pressure jump polynomial without including the swirl effect.

Figure 5.31 presents the comparison of static pressure at plane C–C. Slightly lower experimental values of static pressure are observed near the fan inlet. The average static pressure at fan #1 inlet face is calculated as –1.23 in. w.g. for the numerical model while it gives –1.34 in. w.g. for the experimental measurement. This shows approximate agreement of static pressure near the fan inlet for the numerical and the experimental models.

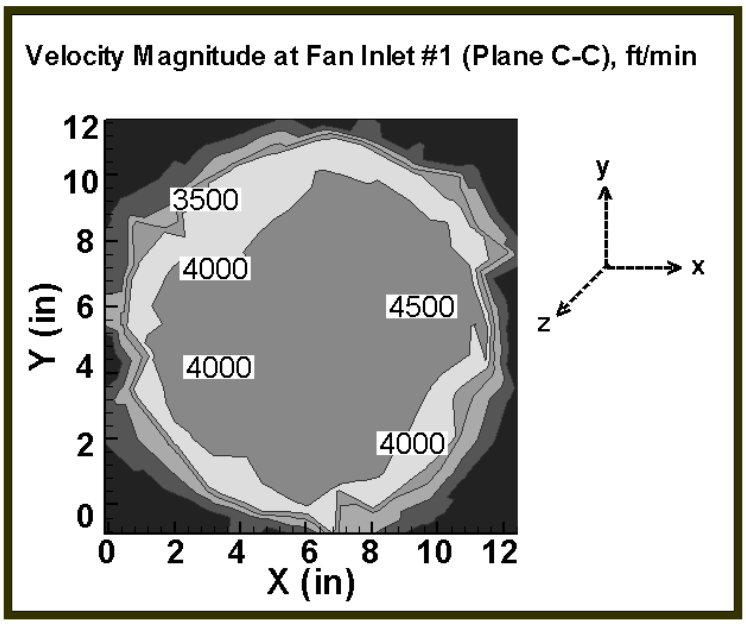

Figure 5.24. Velocity magnitude predicted at fan inlet #1 (plane C–C)

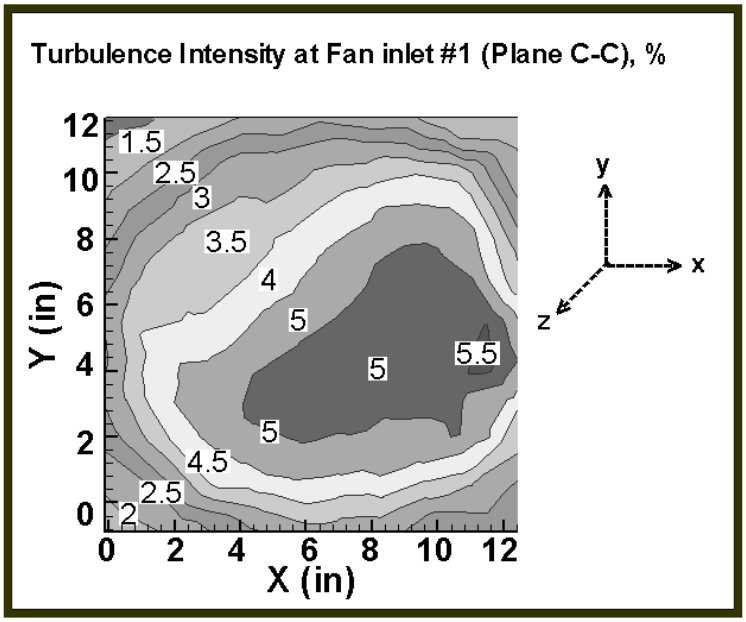

Figure 5.25. Turbulence intensity of velocity at fan inlet #1 (plane C–C).

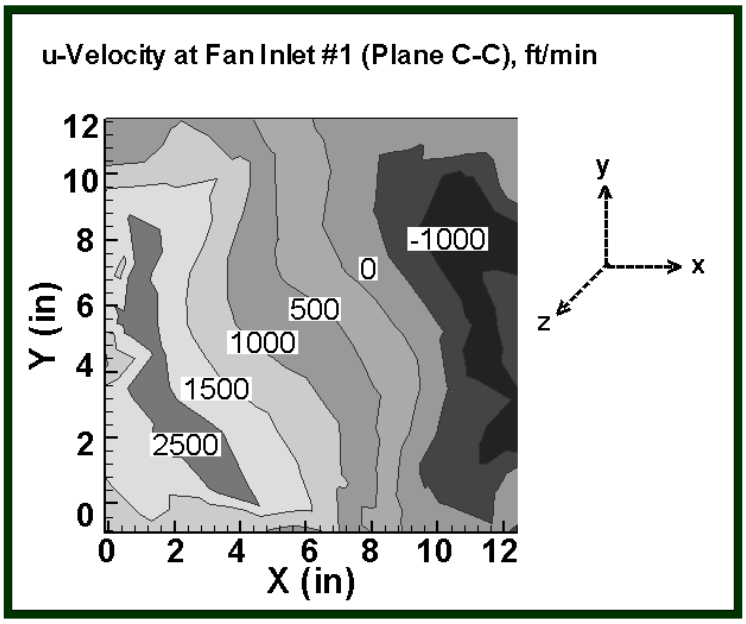

Figure 5.26. u-velocity predicted at fan inlet #1 (plane C–C).

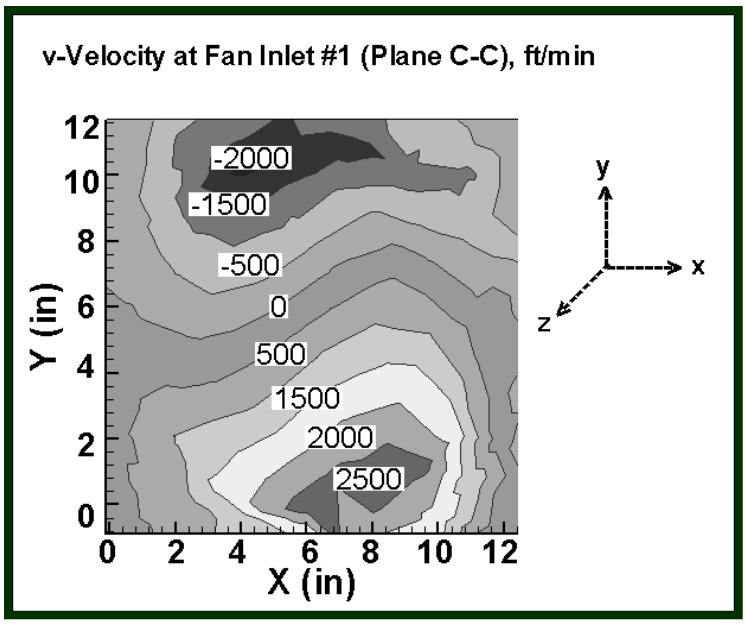

Figure 5.27. v-velocity predicted at fan inlet #1 (plane C–C).

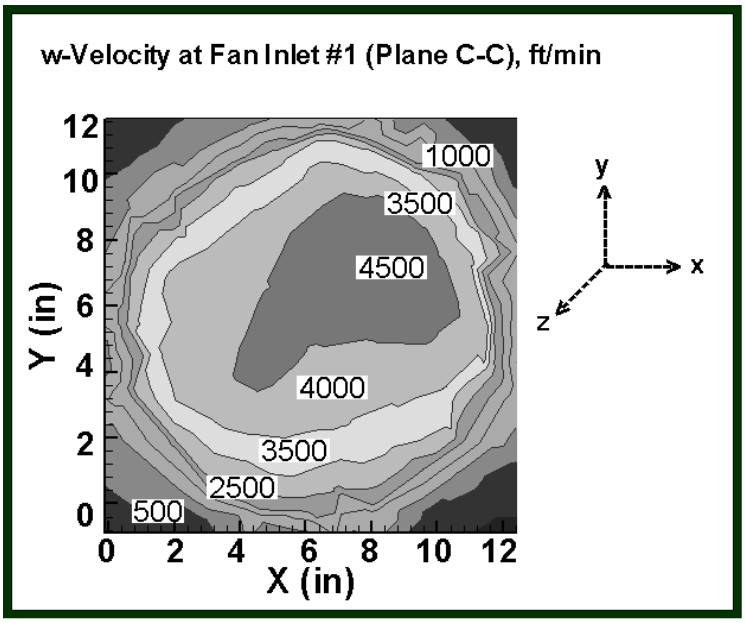

Figure 5.28. w-velocity predicted at fan inlet #1 (plane C–C).

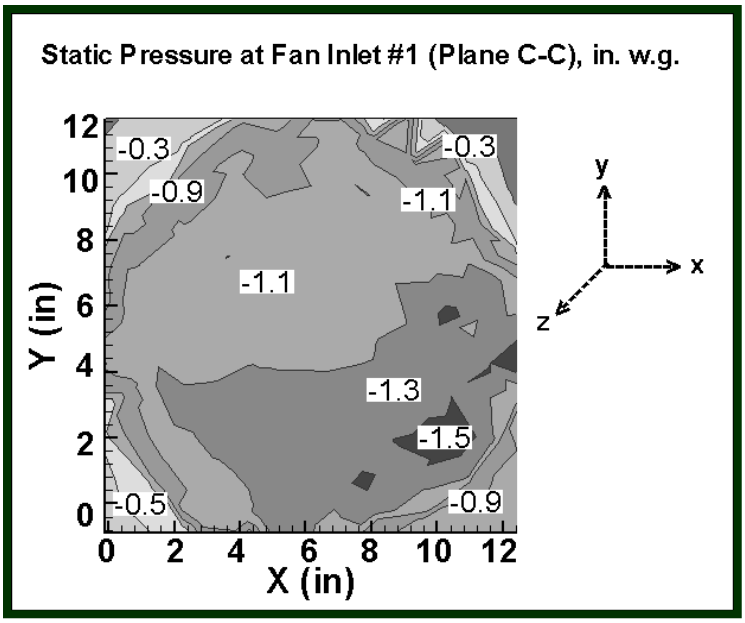

Figure 5.29. Static pressure predicted at fan inlet #1 (plane C–C).

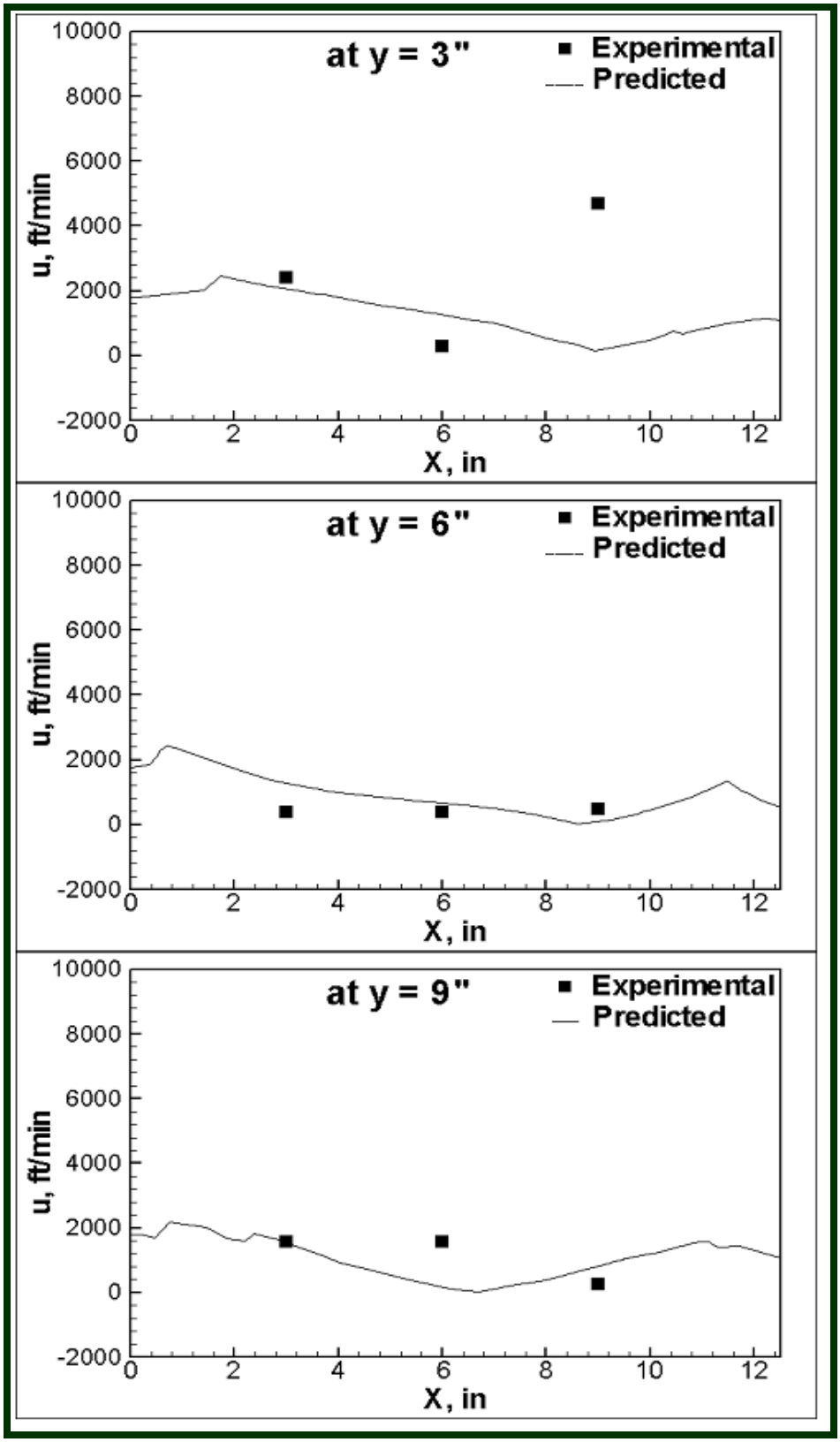

Figure 5.30. Comparison between experimental and predicted u-air speed at plane C-C.

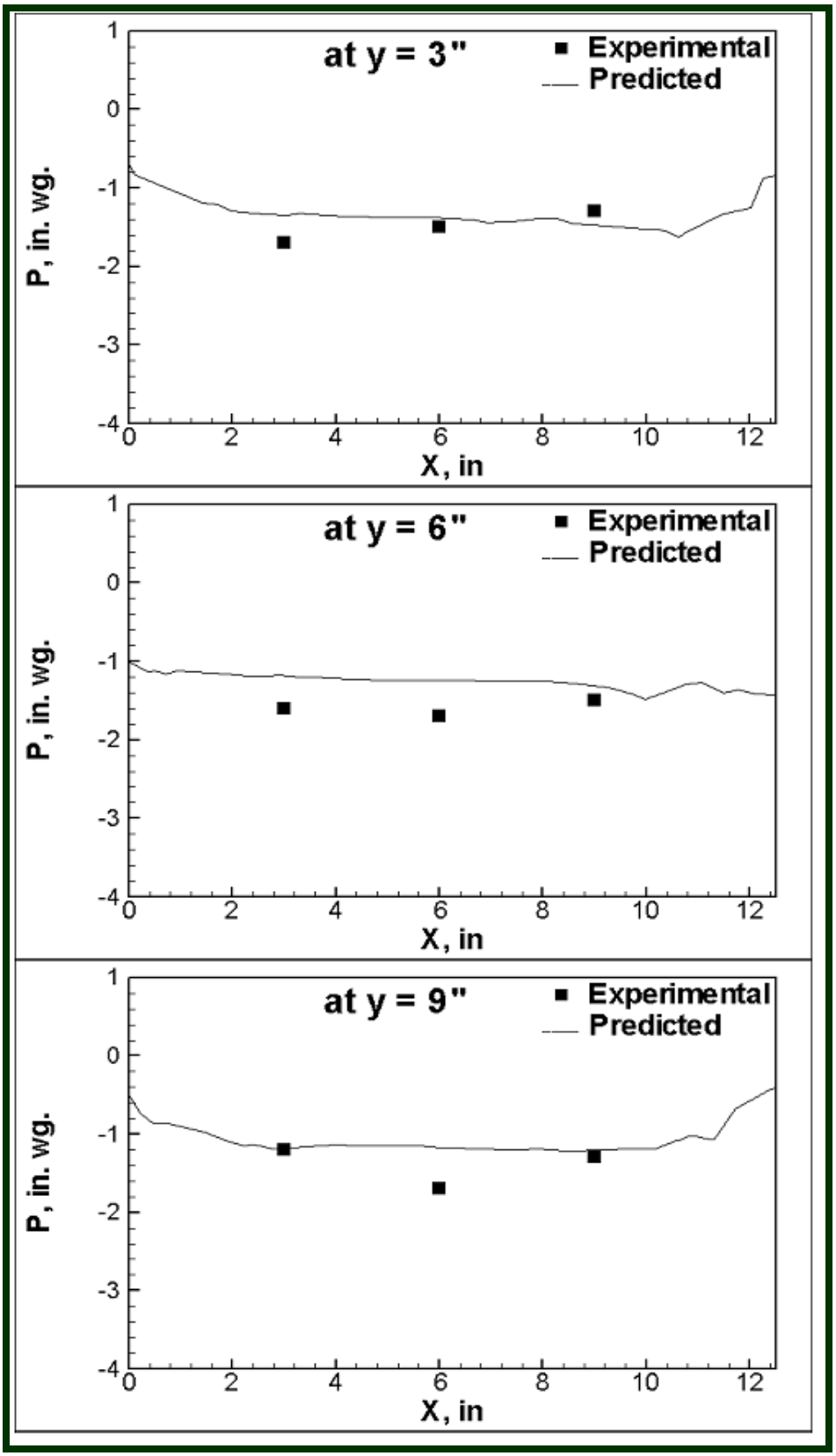

Figure 5.31. Comparison between experimental and predicted static pressure at plane C-C.

5.5.2 PLANE F–F (FAN OUTLET)

It was mentioned that the pressure jump function of air velocity was applied at the fan outlet faces. Plane F–F represents the normal face to the inclined fan outlet cross sectional area (see Figure 2.8 and Table 2.1 for reference). Figure 5.32 shows the contours of velocity magnitude at fan # 1 outlet face. Figure 5.33 presents static pressure contours that vary between negative and positive values from –0.4 to 0.8 in. water gauge. This indicates a re-circulating flow at the fan outlet face because of the non-uniform static pressure. The air supplied by the inclined fan tends to hit the facing wall producing large circulations. These circulations cause a frictional pressure drop and a complex flow near the unit outlet.

It is desirable to calculate the flow rates performed at each fan to check weather or not an even airflow distribution is satisfied across each one. The predicted airflow rate at fan #1 is 6,404 ft^3/min while it is 6,362 ft^3/min for fan # 2. The flow rate of fan #1 is slightly larger than of fan # 2. This is due to the blockage caused by the pulley and the rotating shaft next to fan # 2. The difference is relatively low (0.6 %) and it could be concluded that both fans perform evenly.

5.5.2.1 Experimental Validation of Plane F–F

Figures 5.34 and 5.35 present comparison of air speed magnitude and static pressure respectively for three y-positions (y = 4 in., y = 8 in. and y = 12 in.). The air speed magnitude shows reasonable agreement at position y = 4 in. but most other points display poor agreement. On the other hand, good agreement of static pressure is indicated for both results as shown in Figure 5.35. The pressure jump performed by fan #1 is calculated by the difference between static pressures at both the fan inlet and fan outlet faces as follows:

$$\Delta P_{prediction} = P_{out} - P_{in} = 0.06 - (-1.23) = 1.29 \ \ in.$$
$$\Delta P_{Experimental} = P_{out} - P_{in} = 0.43 - (-1.34) = 1.77 \ \ in. \tag{5.11}$$

This indicates that a lower pressure jump is predicted in the CFD model than the actual pressure jump. This deviation may be due to the simple fan model in the CFD simulation, where it represents the pressure jump function on a specified face. In the experimental unit, the pressure addition is performed through a body force by the rotating impeller. The pressure jump function in the CFD model was varied until a good agreement of volume flow rate was satisfied for both the numerical and the experimental model. Minimizing the difference between both the experimental and computational model requires further investigation, which is beyond the scope of this study.

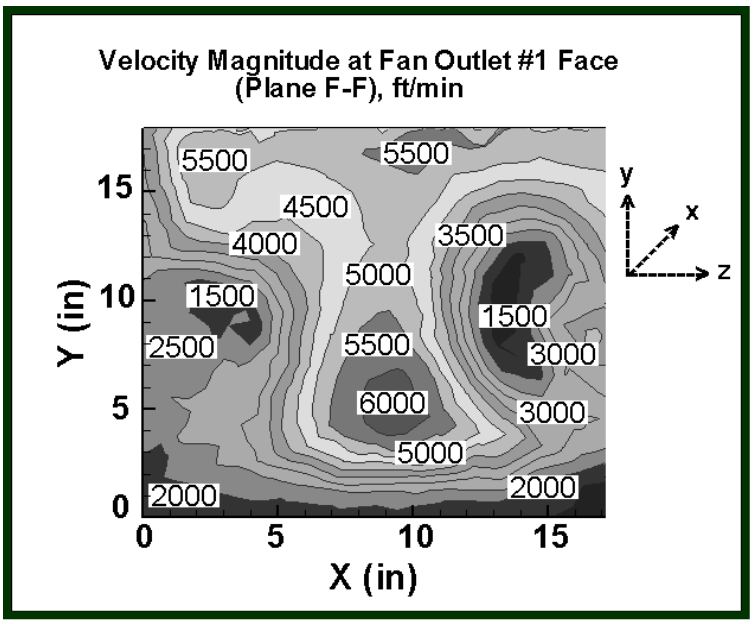

Figure 5.32. Velocity magnitude predicted at fan outlet #1 (plane F–F).

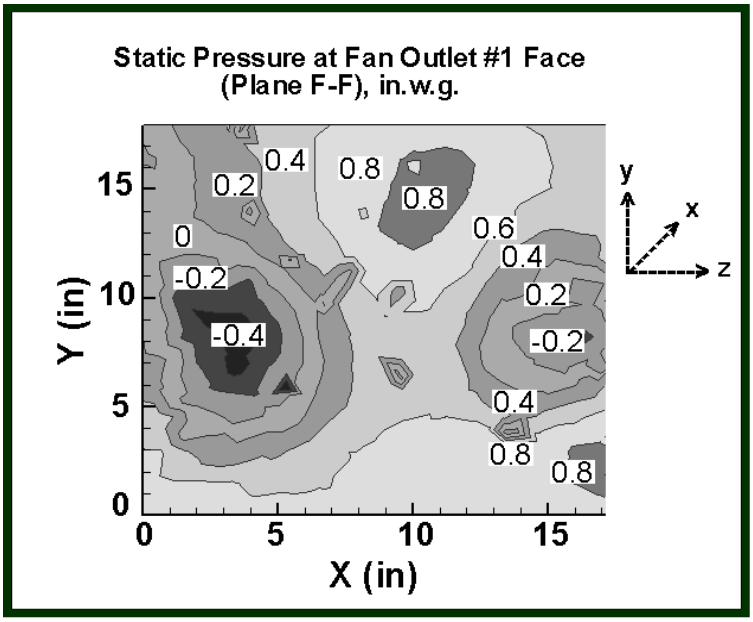

Figure 5.33. Static pressure predicted at fan outlet #1 (plane F–F).

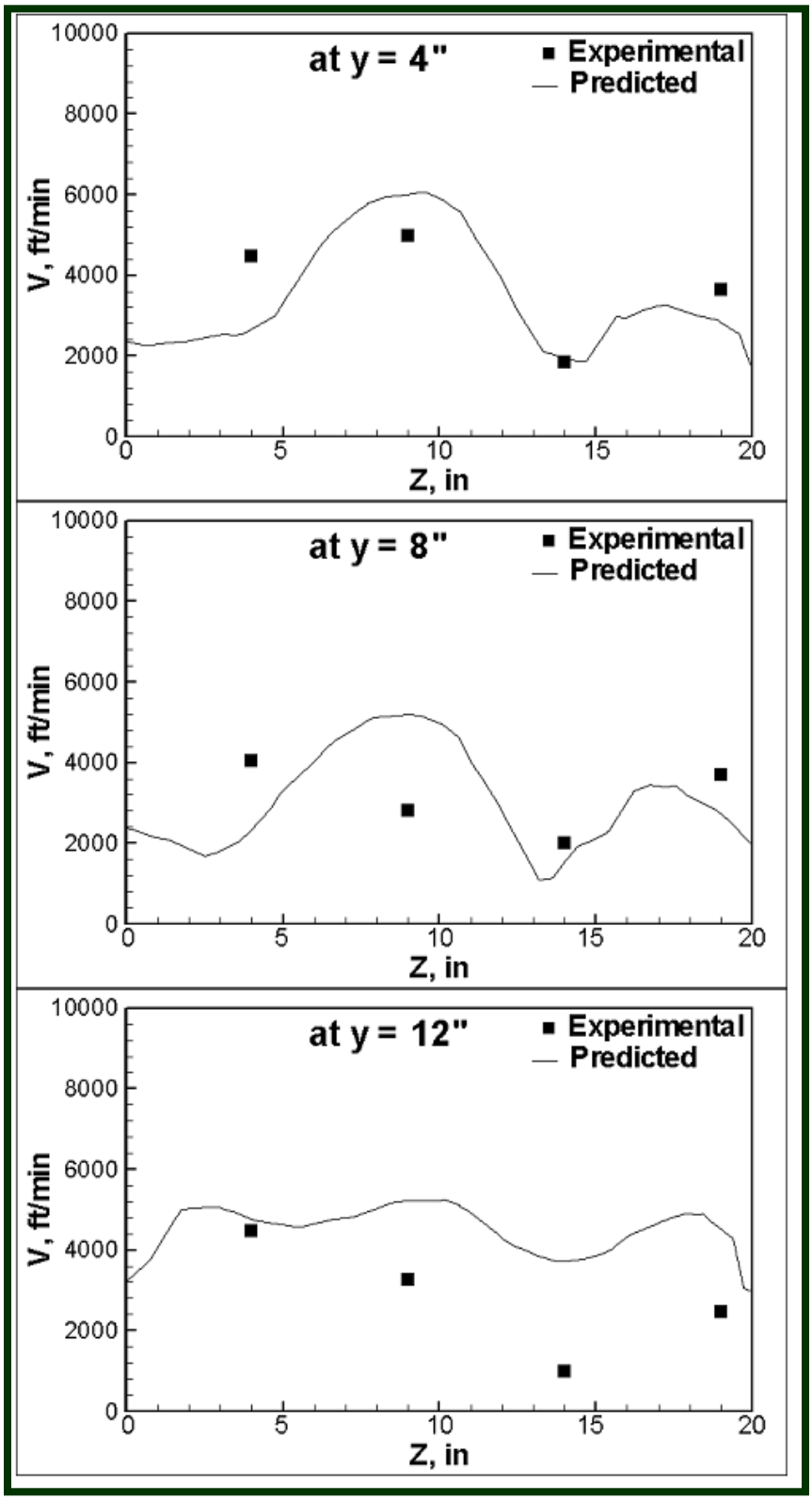

Figure 5.34. Comparison between experimental and predicted air speed magnitude at fan outlet # 1 (plane F–F).

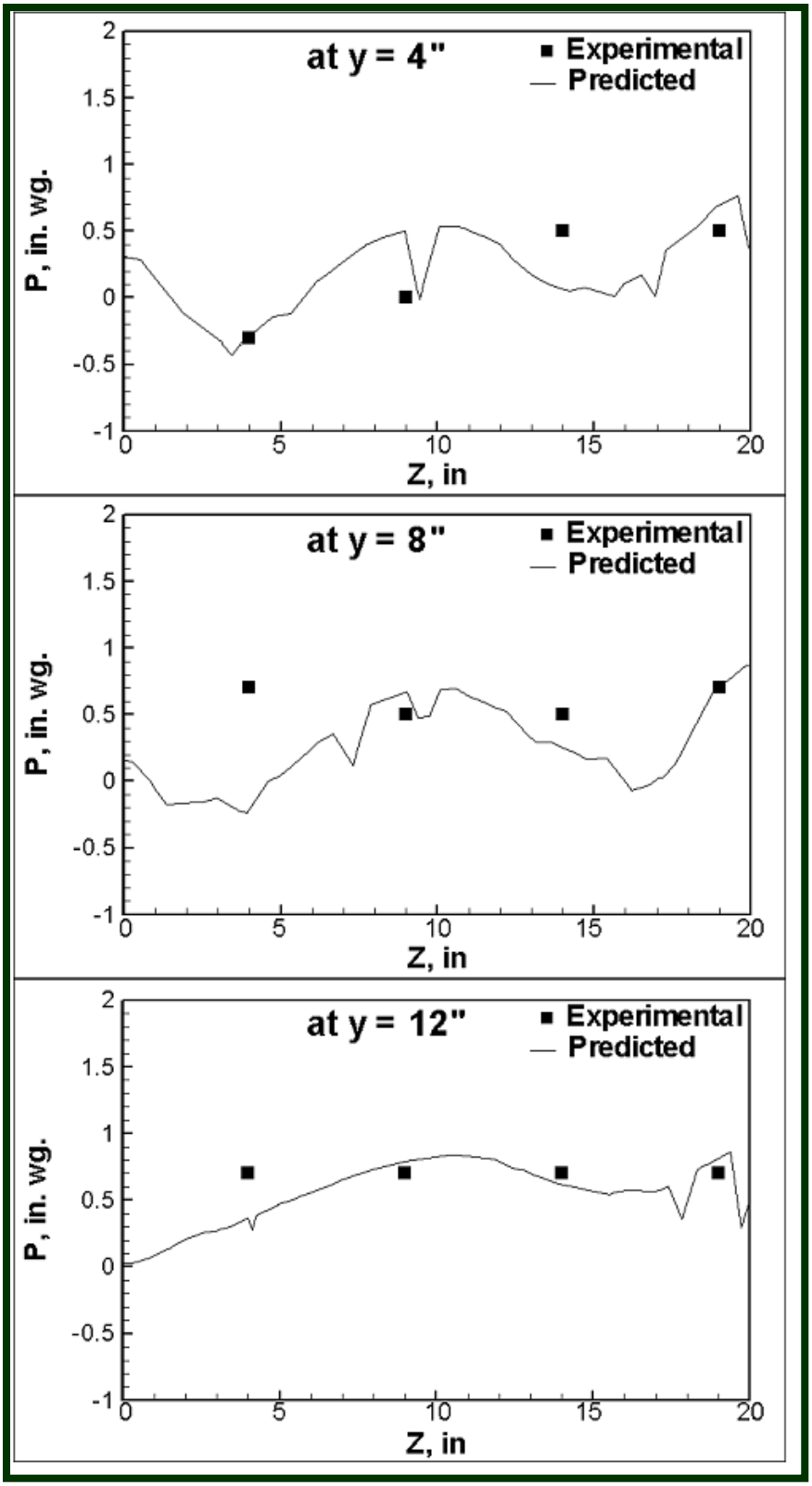

Figure 5.35. Comparison between experimental and predicted static pressure at fan outlet # 1 (plane F–F).

5.6 OUTLET

The flow regime resulting from arrangement of various components in the flow field appears as a complex one especially in the area close to the outlet section. Figures 5.36 and 5.37 show contours of velocity magnitude and the w-component on the outlet face. The air leaving the fan is forced to turn 90° angles to the direction of unit outlet. This produces more turbulence in the flow and the velocity exceeds 3500 ft/min. This also affects the fan performance, since the flow circulation causes building of pressure and further creates additional load on the fan. Static pressure at the outlet face is maintained at 0.15 in. w. g. as boundary condition of the numerical model.

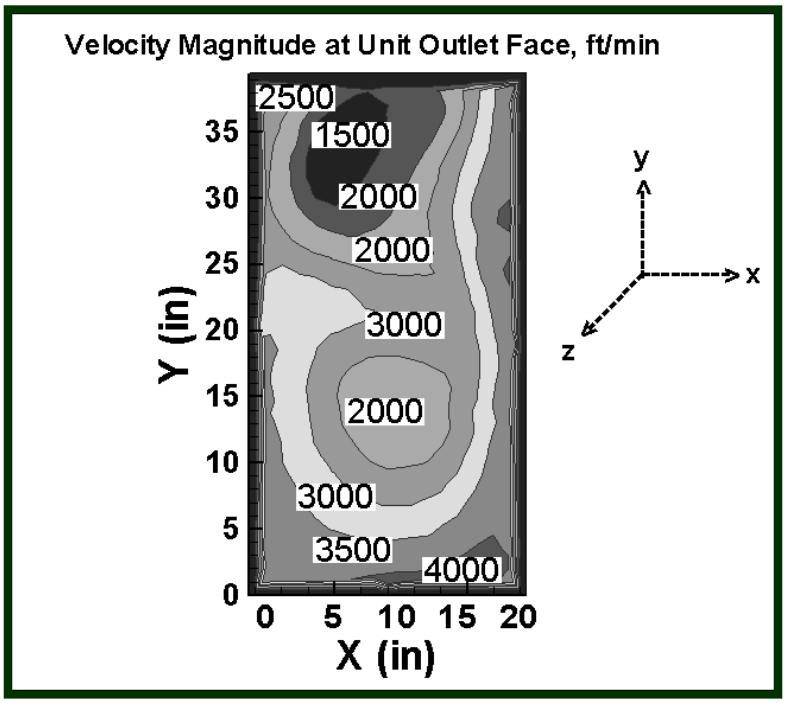

Figure 5.36. Velocity magnitude predicted at unit outlet.

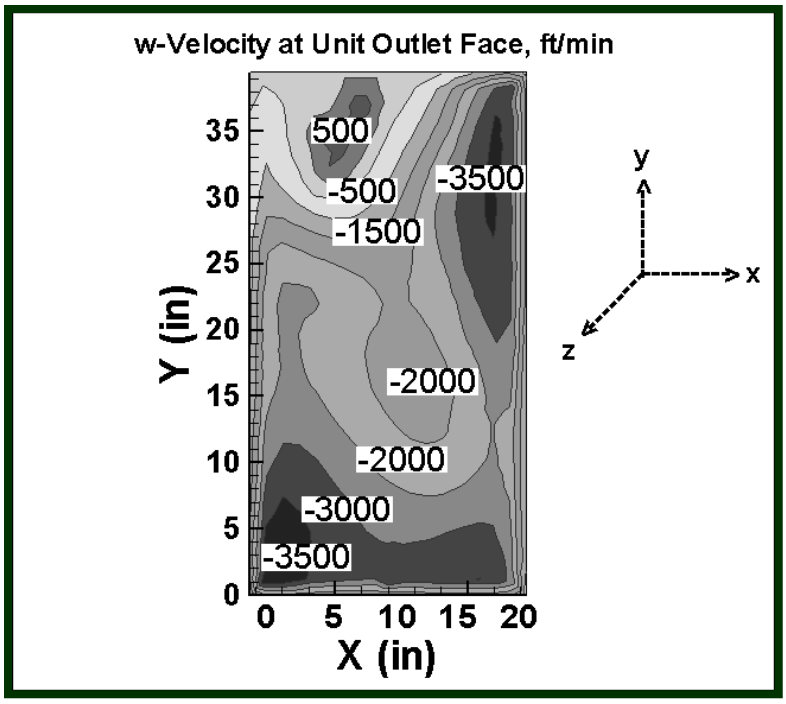

Figure 5.37. w-velocity predicted at unit outlet.

CHAPTER 6

PARAMETRIC STUDY

6.1 DESIGN PARAMETERS

A parametric study is attempted towards optimizing the performance of the packaged unit under different design parameters. These parameters represent the position of specified components in the unit. Rearrangement of component positions like inlet, outlet, evaporator and fan leads to a major deflection of flow path inside the unit. These design parameters chosen are thought to have a strong impact on the airflow distribution and pressure drop. They affect thermal and dynamic performance of the unit. It is known that the heat transfer across evaporator increases as higher velocity air passes through it. Also the pressure drop will increase due to friction at the evaporator. The change in velocity distribution caused by altering the unit flow configuration will affect the heat transfer and pressure drop.

The effect of variable design parameters on the PU300 unit performance is studied using similar CFD approach introduced in the last two chapters. New positioning of the components is applied to the basic geometry of the unit. Then, the CFD model of the new geometry is solved to predict flow characteristics. Table 6.1 displays the design parameters and their different positions as

placed in the unit layout. There is limitation of the proposed changes in relation to the accessibility and/or installation requirements of the unit. For example, the wide evaporator position could not be placed elsewhere in the unit, but it could be inclined with a small angle to improve flow distribution. Although some combinations of these parameters are not practical, they are selected for theoretical investigation.

Table 6.1. Variation of design parameters in the construction of PU300.

Item	*Parameter*	*Position No.*	*Description*
A	Inlet	1	XY vertical plane
		2	YZ vertical plane
		3	XZ horizontal plane
B	Evaporator	1	Vertical
		2	Inclined about Y-axis
		3	Inclined about Z-axis
C	Fan	1	Inclined about Z axis
		2	Horizontal
		3	Vertical upward
D	Outlet	1	XY vertical plane
		2	YZ vertical plane
		3	XZ horizontal plane

Four geometries out of twenty-four combinations are selected for investigation. Some of these geometries involve a single design change, while the others involve more than one change in order to find out the best combination by means of thermal and dynamic (pressure drop) performance. The selected combinations are classified with reference to the denoted symbols of each parameter (see Table 6.1). The standard unit geometry is classified as A1B1C1D1. The letter identifies parameter name while the number identifies its position. The classification of the selected ge-

ometries with the description of each one is shown in Table 6.2. Figures 6.1–6.4 show the drawings of the different geometries proposed as described in Table 6.2.

Table 6.2 Classification of geometries with variable parameters included

Geometry No.	*Classification*	*Description of parameters*
1	A1B1C1D1	Standard unit geometry
2	A1B2C1D1	Inclined evaporator about y-axis
3	A2B1C1D2	Inlet at yz vertical plane Outlet at yz vertical plane
4	A3B3C2D3	Inlet at xz horizontal plane Inclined evaporator about z-axis Horizontal fan Outlet at xz horizontal plane

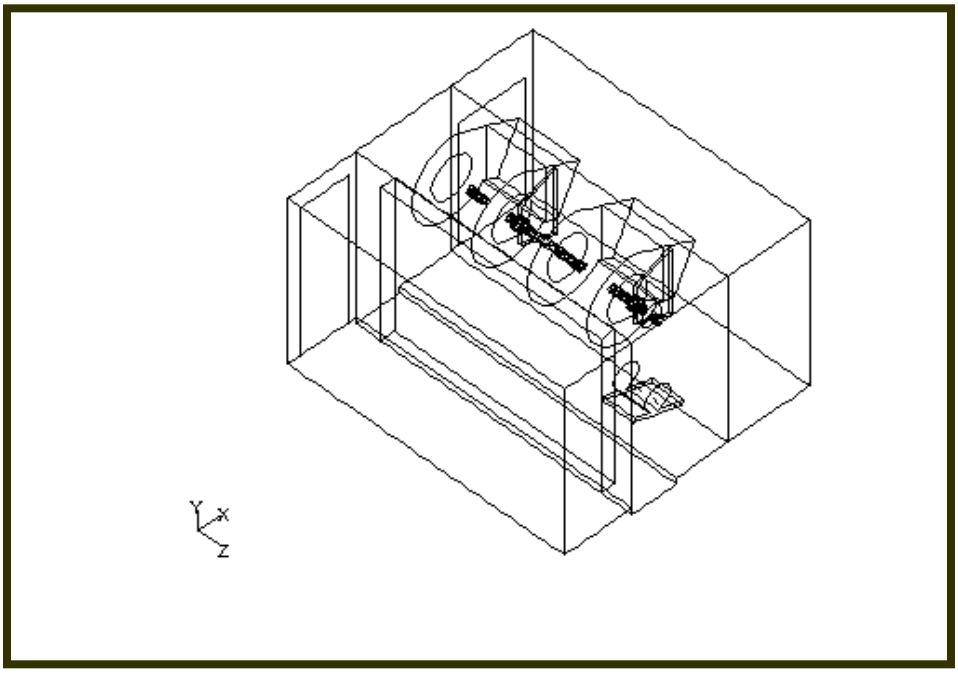

Figure 6.1. Geometry # 1 (Standard packaged unit).

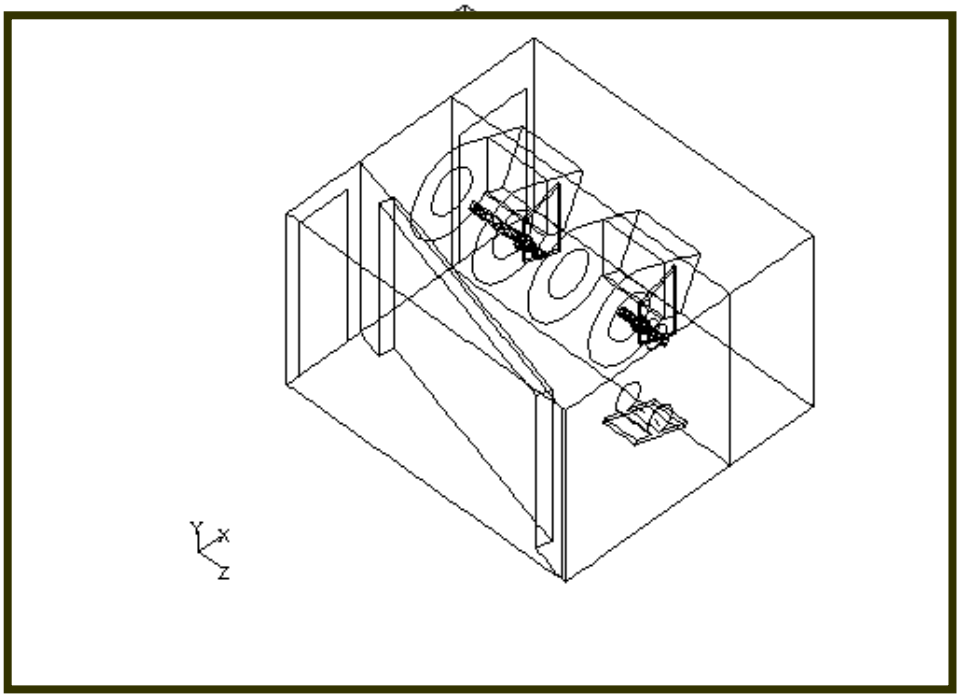

Figure 6.2. Geometry # 2.

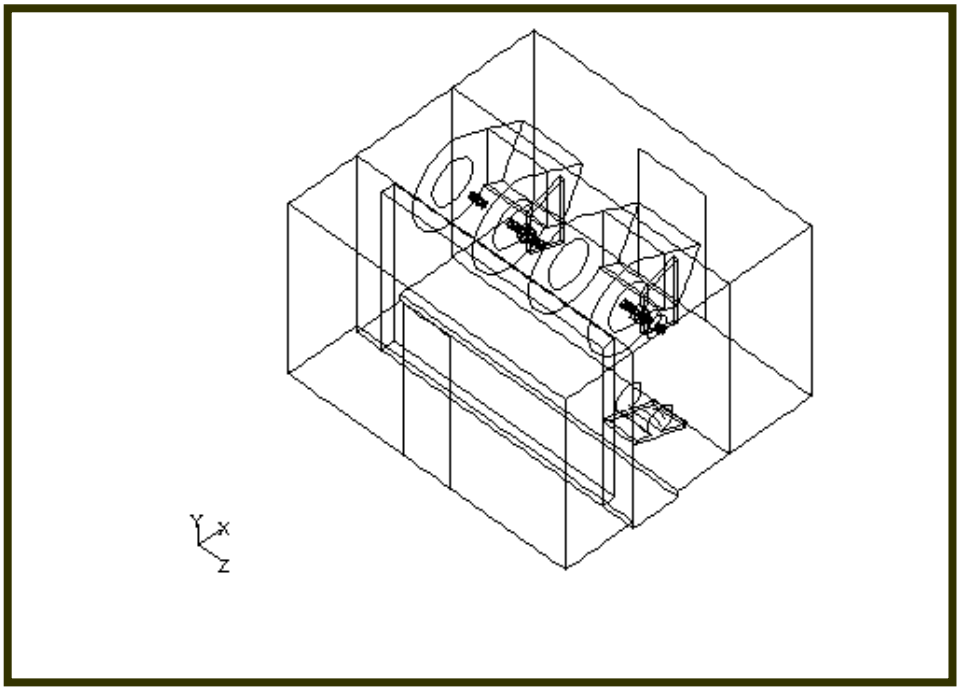

Figure 6.3. Geometry # 3.

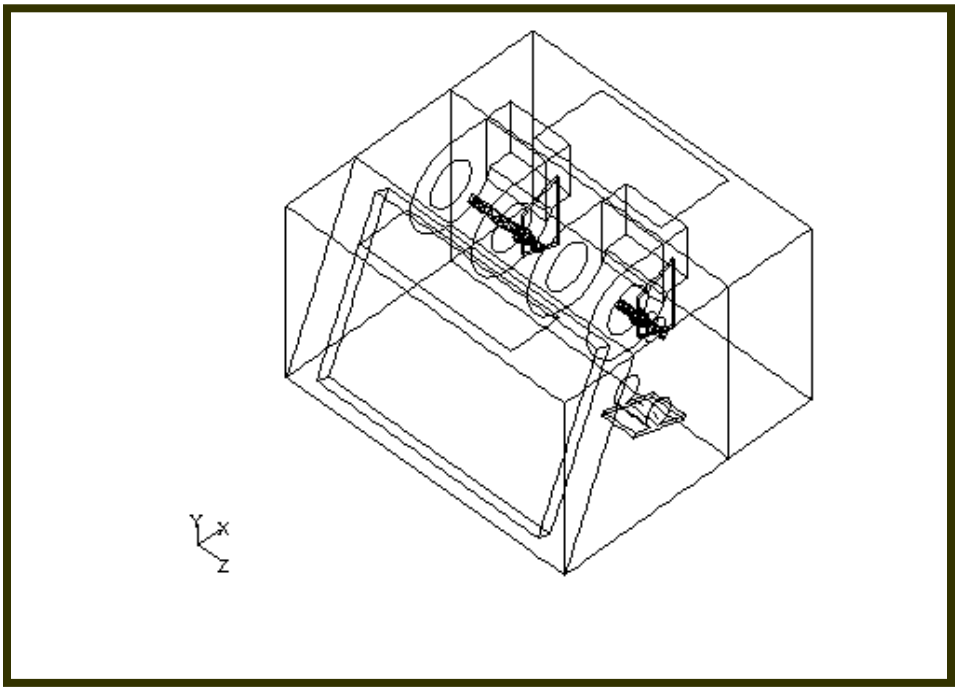

Figure 6.4. Geometry # 4.

6.2 THERMAL AND FLOW PERFORMANCE

To evaluate the thermal and flow performance of the proposed geometries from the predicted flow characteristics, it is required to identify following outputs:

- Airflow rate supplied by the system (Q, ft^3/min).
- Average air temperature (T_{avg},° F) downstream of the evaporator. Also, bulk average air temperature (T_b,° F) is required on the plane downstream of the evaporator for the sake of calculating evaporator cooling capacity q.

The obtained outputs are presented in Table 6.3. It shows the thermal and flow performance of the four geometries. The effect of deviating a single or multi design parameters is evaluated by comparison with the standard unit configuration provided in geometry # 1 as in Figure 6.1.

Table 6.3. Predicted performance of all geometries using CFD modeling.

	Geometry No.			
	1	***2***	***3***	***4***
Q (ft^3/min)	12,763	13,236	13,176	12,693
T_{avg} (°F)	55	55.3	55.8	56
q (Btu/h)	356,320	362,038	353,106	337,378
q (Tons)	29.7	30.2	29.4	28.1

From Table 6.3, different airflow rates are predicted in the selected geometries. This indicates the effect of altering airflow configuration of the unit, which results into adding or reducing resistances on the flow path. Geometry #2 offers the highest airflow rate compared to others. The evaporator inclination about y-axis is found to be useful in modifying the flow rate of this geometry. The reason for this is the elimination of circu-

lation region upstream of the evaporator. Also, it offers more space for flow to be redirected in the direction of the fan inlets.

Furthermore, the highest capacity is achieved by geometry #2, which supplies 30.2 tons. The cooling capacity depends on the airflow rate and the temperature difference of air and the evaporator tubes surface. Although the leaving air temperature of this geometry is slightly higher than that of the standard unit, but the change in the flow rate is considerable.

In geometry #3, the overall flow path is straight since the inlet, evaporator, fan and outlet are all in the same direction. For some reason, this geometry offered slightly less flow rate and capacity than the standard unit. Finally, vertical flow path is introduced in geometry #4. It supplied the lowest performance compared to others. Better performance may be obtained by ducting the fan outlet all the way to the unit outlet.

CHAPTER 7

CONCLUSION AND RECOMMENDATION

7.1 GENERAL

In this study, CFD modeling of airflow inside the packaged unit (PU300) was performed. The predicted airflow characteristics were presented at specified planes in the flow field. Validation of the CFD model was attained by performing experimental measurements of flow characteristics in the unit. The airflow characteristics included air speed components, pressure, temperature and turbulence quantities of air in the actual unit.

The experimental measurement took long process. Special arrangement was applied for the experimental unit set-up. The sheet metal of the top and side walls of the unit were re-fabricated to incorporate long-cut slots. These slots permit accessibility of inserting the velocity probe in the airflow field.

Each measurement plane incorporated a good number of measurement points. For example, plane A–A contained 48 measurement points. The three components of velocity were collected at the same point. It was required to turn the velocity sensor window in different directions to ob-

tain the other components of air speed. The logging time interval required for each measurement was 3-minutes for velocity and 5-minutes for temperature. The measurements took place after system stabilization of airflow rate and refrigerant superheat. It usually takes two hours from unit start-up operation. The experimental work took 31-days of logging time with a careful probe mounting and assuring the right direction of sensor's window.

Due to above reasons, it was not possible to perform an experimental parametric study on the unit performance. This requires a long time and large budget. Instead, a parametric study was performed by varying design parameters in the CFD model. This parametric study offered plenty of information about the effect of different unit configurations on the flow regime. Also, it helped to evaluate the performance of the unit under modified flow path. The standard packaged unit geometry provided the lowest thermal and dynamic performance by comparison with the other geometries of different flow configuration. This is due to its complicated flow configuration.

7.2 FINDINGS

The proposed CFD model of the packaged air conditioning unit has provided an insight to flow regime inside the unit. In evaluating the validity of this model in contrast with the experimental investigation, advantages and disadvantages were noted below.

The heat exchanger model was selected as a porous media by assuming a constant heat exchanger surface temperature. In the actual unit, the evaporating refrigerant temperature was varying between different tube circuits. More sophisticated heat exchanger model is desired to reflect the actual refrigerant circuits with their variations in temperature. This can be attained by dividing the heat exchanger surface to a number of sub-surfaces. Each one has different temperature. However, with the existing porous media, the CFD model offered good agreement with the experimental unit.

The fan model introduced in the CFD approach showed an acceptable agreement with the actual unit. The pressure jump was almost in the same range between both cases. The centrifugal fan (in the experimental unit) was creating a swirl because of the rotating impeller. Although, this fan swirl was not considered in the CFD model.

The unit configuration was a complicated one. It incorporated a turning flow path, which experienced a complex and re-circulating flow behavior. This complexity was a challenge for the k-ε turbulent model. If the comparison was performed on a uniform configuration, then part of this complexity could have been eliminated.

In the experimental investigation, the velocity probe used in the flow measurements did not have the capability to collect transient data. Its minimum logging time interval was 1-second, which was not enough to monitor turbulent and fluctuating flow.

The proposed CFD model in this study is considered successful one since it showed acceptable agreement with the experimental unit. It is classified as a base model that could be amended in future work by implementing the points explained in the recommendations.

7.3 RECOMMENDATIONS

Future work to extend this study may require considering certain factors in both the CFD modeling and the experimental investigation. These factors are noted below:

- In the heat exchanger model, it is recommended to incorporate the details of refrigerant tube circuits to have more accurate simulation in the CFD model.
- Modeling condensation of water vapor content in air at evaporator surface is essential. It aims to predict the latent load applied in the airside.

- Building boundary layers near the wall is recommended. However, the curved geometry of the walls and unit boundaries causes difficulty in boundary layer construction.
- Introducing the fan swirl effect is desired. It may be fulfilled by introducing the components of radial and tangential velocities at the fan inlet. It may have an effect on the flow distribution in the regions downstream of evaporator.
- In the experimental measurements of the actual flow characteristics, it is proposed to have a more sophisticated instrument for flow measurements. Hot wire anemometer is recommended as it monitors the velocity fluctuation more accurately. Also, the mounting of the probe should include automatic traversing system to identify the correct orientation of the measurement points.
- Finally, identifying more design parameters is required for an extensive parametric study. For example, varying the evaporating refrigerant temperature, proposing new refrigerant circuits layout, and studying the performance under different operating conditions of air entering the unit.

REFERENCES

1. Xu, Z.G., Gothman, D.H.T., Collins, M.W., Coney, J.E.R., Sheppard, C.G.W., Merdjani, S., CFD Prediction of Turbulent Recirculating Flow in an Industrial Packaged Air Conditioning Unit, HVAC & R Research, Volume 2, Number 3, p. 195-214, 1996.

2. Aganda, A.A., Coney, J.E.R., Sheppard, C.G.W., Airflow Maldistribution and the Performance of a Packaged Air Conditioning Unit, Applied Thermal Engineering, Volume 20, Number 6, p. 515-528 (2000).

3. Xu, Z.G., Gothman, D.H.T., Collins, M.W., Coney, J.E.R., Sheppard, C.G.W., and Merdjani, S., A Numerical and Experimental Study of Turbulent Flow Through the Evaporator Coil in an Air Conditioning Unit, International Journal of Refrigeration, Volume 19, Number 6, p. 369-381, 1996.

4. Xu, Z.G., Gothman, D.H.T., Collins, M.W., Coney, J.E.R., Sheppard, C.G.W., and Merdjani, S., Validation of Turbulence Models in a Simulated Air Conditioning Unit, International Journal of Numerical Methods in Fluids, Volume 26, p. 199-215, 1998.

5. Xu, X.Y., Xu, Z.G., Gothman, D.H.T., Collins, M.W., CFD Analysis of Flow in Medium Sized Vertical Air Conditioning Units, Proceeding s of the International Conference on Energy and Environment, ICEE 1998, China Machine Press, Beijing, China, p. 221-229.

6. Yun, J., Lee, K., Influence of Design Parameters on the Heat Transfer and Flow Friction Characteristics of the Heat Exchanger with Slit Fins, International Journal of Heat and Mass Transfer, Volume 43, p. 2529-2539, (2000).

7. Mitsushima, Y., Takeuchi, T., Kohri, I., Prediction Method of Engine Compartment Airflow Using CFD Analysis., JSAE Review, Volume 21, p. 197-203, (2000).

8. Aganda, A.A., Coney, J.E.R., Farrant, P.E., Sheppard, C.G.W., Wongwuttanasatian, T., A Comparison of the Experimental and Predicted Heat Transfer Performance of an Evaporator Coil Circuit., Applied Thermal Engineering, Volume 20, Number 6, p. 499-513, (2000).

9. Stoecker, W.F., Jones, J.W., Refrigeration and Air Conditioning., McGraw-Hill, USA, 1982.

10. Park, M., Farrant, P.E., Hewitt, G., The Effect of Air Maldistribution on Heat Transfer Performance in Air Conditioning Unit., Heat Transfer and Fluid Flow Service, National Engineering Laboratory, East Kilbride, Glasgow G75 OQU, 1993.

11. Aganda, A.A., The Effect of Airflow Non-Uniformity on Heat Exchanger Perform-ance, with Special Reference to Air Conditioning Units., P.h.D. Thesis. Department of Mechanical Engineering, The University of Leeds, 1995.

12. Fagan, T.J., The Effect of Flow Maldistributions on Air to Refrigerant Heat Exchanger Performance, Transactions ASHRAE 86 (2), p. 699-713, (1980).

13. Hewitt, G.F., Shires, G.L., Bott, T.R., Process Heat Transfer., 2000, New York. Begell House.

14. Koido,T., et al., Development of Compact Heat Exchanger for Air Conditioner., Proceeding of the 26th JAR Annual Conference, p. 65-168, 1992.

15. Yun, J.Y., & Lee, K.S., Investigation of Heat Transfer Characteristics on Various Kinds of Fin-and-Tube Heat Exchangers with Interrupted Surfaces., International Journal of Heat and Mass Transfer, Volume 42, p. 2375-2385, (1999).

16. FLUENT 5 User Guide Manual. 1998., Fluent Inc. E.I. du Pont de.

17. Van Doormal, J.P., Raithby, C.D., Enhancement of the Simple Method for Predicting Incompressible Fluid Flows, Numerical Heat Transfer, Volume 7, p. 147-163, (1984).

18. McQuiston, F.C., Parker, J.D., Heating, Ventilating and Air Conditioning Analysis and Design, New York. John Wiley & Sons, Inc., 1994.

19. Trane Air Conditioning Manual, 1988, McGraw Hill, USA.

20. TSI Incorporated, Air Velocity Meter VelociCalc Plus Model No. 8386, Operation and Service Manual.

21. Najim, A.U., Energy Efficient Buildings and Their Effects on the National Economy, Symposium, King Fahd University of Petroleum and Minerals, 5 Feb. 2002.

VITAE

- Adel M. Al-Nasser
- Born in Al-Hassa, Saudi Arabia in 1975.
- Acquired Bachelor of Engineering (BE) in Mechanical Engineering from King Fahd University of Petroleum and Minerals, Dhahran, Saudi Arabia in 1998.
- Served as a Research Engineer at Zamil Air Conditioners, Dammam, Saudi Arabia from 1998 to 2003.
- Received Master of Science (MS) in Mechanical Engineering from King Fahd University of Petroleum & Minerals, Dhahran, Saudi Arabia in 2003.